NICKEL-MANGANESE PHOSPHATE/ELECTROCHEMICAL EXFOLIATED GRAPHENE NANOCOMPOSITES FOR HYBRID SUPERCAPACITORS

by

TSHUPO KGWADIBANE

submitted in accordance with the requirements for
the degree of

MASTER OF SCIENCE

in the subject

CHEMISTRY

at the

UNIVERSITY OF SOUTH AFRICA

SUPERVISOR: PROF MOSHAWE J. MADITO

CO-SUPERVISOR: DR NTUTHUKO W. HLONGWA; PROF XOLILE FUKU

05/12/2025

DECLARATION

Name: TSHUPO KGWADIBANE

Student number: 15812650_

Degree: M.Sc. Chemistry

I declare that: (Exact wording of the title of the dissertation as appearing on the electronic copy submitted for examination)

NICKEL-MANGANESE PHOSPSHATE/ELECTROCHEMICALLY EXFFOLIATED

GRAPHENE NANOCOMPOSITES FOR HYBRID SUPERCAPACITORS

I declare that the dissertation is my own work and that all the sources that I have used or quoted have been indicated and acknowledged by means of complete references, and that any use of Artificial Intelligence (AI) has been fully disclosed.

I further declare that I submitted the dissertation to the appropriate originality detection system which is endorsed by Unisa and that it falls within the accepted requirements for originality.

I further declare that I have not previously submitted this work, or part of it, for examination at Unisa for another qualification or at any other higher education institution.

I further declare that where Artificial Intelligence (AI) tools have been used in the preparation of this thesis/dissertation, their use has been limited to ethical permissible support, has been fully disclosed, and does not replace my own original research, my independent critical thinking and analysis, or authorship responsibilities.
I understand that failure to disclose AI use, plagiarism and/or lack of academic integrity may constitute academic misconduct under Unisa's policies.

(The dissertation will not be examined unless this statement has been included.)

Kgwadibane

SIGNATURE

05/12/2025

DATE

DEDICATION

To my late brother, Lesedi Kgwadibane, my sister, Boitumelo Kgwadibane, and my late friend, Zodwa E. Jantjies your memory continues to inspire me. Your unwavering belief in my potential, your encouragement, and the light you brought into my life have carried me through this journey. This work is a tribute to the impact you made on my academic path.

To my parents, Kgakgamaco M. Kgwadibane and Jappie J. Kgwadibane, thank you for your love, strength, and sacrifice.

To my brothers (Kagiso, Rammileng, Kabelo, and Otsile) and my sisters (Mapampiri and Olebogeng) your support and faith in me have been my anchor.

This achievement is as much yours as it is mine.

ACKNOWLEDGEMENTS

I would like to express my deepest gratitude to God for granting me strength, guidance, and perseverance throughout the course of this research.

My sincere appreciation goes to my supervisor, Prof. Moshawe J. Madito, and my co-supervisors, Dr. N.W. Hlongwa and Prof. X. Fuku, for their continuous support, invaluable guidance, and constructive insights. Their mentorship has been instrumental in shaping both this dissertation and my development as a researcher.

This work forms part of the research supported by the University of South Africa (UNISA), through the Institute for Nanotechnology and Water Sustainability (iNanoWS). I am grateful to iNanoWS for providing the facilities and resources necessary to complete this study. I also acknowledge and sincerely appreciate the financial support I received from iNanoWS during my MSc studies.

I extend heartfelt thanks to my family and friends for their unwavering encouragement, patience, and belief in me. Their support has been a constant source of motivation.

My sincere appreciation also goes to Dr. Bello for his assistance with the synthesis and characterization of the wastewater sludge-derived activated carbon. His support added significant value to this work.

I would also like to acknowledge the AEC Thematic Area staff members and students for their collaborative support, guidance, and constructive discussions that enriched this research.

Lastly, I would like to thank the laboratory technicians for their assistance, technical support, and guidance throughout the experimental work. Their contribution played an important role in the successful completion of this dissertation.

ABSTRACT

The global shift toward sustainable energy technologies has increased the demand for advanced energy storage systems that deliver both high energy and power densities. Conventional supercapacitors provide excellent power output, rapid charge-discharge capability, and superior cycling stability; however, their low energy density restricts practical applications. In contrast, rechargeable batteries offer higher energy densities but are limited by slower charge rates and reduced cycling stability. Hybrid configurations that integrate the complementary advantages of both systems have therefore emerged as a promising approach to achieving balanced performance.

Nickel-manganese phosphate/electrochemically exfoliated graphene $NiMn(PO_4)_2$/EEG) nanocomposite was synthesized via a hydrothermal method. Structural and morphological analyses, including X-ray diffraction (XRD), scanning electron microscopy with energy-dispersive spectroscopy (SEM-EDS), high-resolution scanning electron microscopy (HRSEM), Fourier-transform infrared spectroscopy (FTIR), and Raman spectroscopy, confirmed the formation of well well-crystallised composite with homogeneous morphology. The $NiMn(PO_4)_2$/EEG composite leverages the multiple redox-active sites and structural robustness of bimetallic phosphate combined with the high conductivity of electrochemically exfoliated graphene, resulting in enhanced charge transport efficiency and electrochemical performance. Additionally, this work presents an investigation of heteroatom-doped EEG thin film synthesised via a two-step process involving graphite intercalation and electrochemically exfoliation in sulphuric-phosphoric acid medium, enabling in-situ doping with nitrogen (N), phosphorus (P), and sulphur (S). The exfoliation products were vacuum filtered to form porous films. Raman spectroscopy revealed Fermi-level shifts of approximately 0.5 eV and heterogeneous defect distributions.

The doped EEG films exhibited enhanced electrical conductivity (~10,000 $S \cdot m^{-1}$) and improved interfacial properties, as evidenced by reduced adhesion forces in force-distance measurements. Electrochemical analyses demonstrated that Fermi-level modulation facilitated rapid interfacial charge transfer by lowering the electrode-electrolyte potential barrier. The doped EEG films achieved a specific capacitance of 150.5 $F \cdot g^{-1}$ at 1.0 $A \cdot g^{-1}$, confirming their potential as highly conductive supports for hybrid electrode configurations.

Furthermore, a $NiMn(PO_4)_2$/EEG composite was integrated with activated carbon (AC) derived from wastewater sludge to fabricate energy storage devices. The $NiMn(PO_4)_2$/EEG composite was synthesised hydrothermally, while AC was produced via phosphoric acid activation. Characterisation verified the formation of a mixed-metal phosphate phase anchored on few-layer graphene. The optimised $NiMn(PO_4)_2$/50 mg EEG electrode achieved a high specific capacity of 822.1 $C \cdot g^{-1}$ at 1 $A \cdot g^{-1}$, significantly outperforming pristine $NiMn(PO_4)_2$. In an asymmetric configuration ($NiMn(PO_4)_2$/EEG//AC), the device delivered an energy density of 40.0 $Wh \cdot kg^{-1}$, a peak power density of 6538 $W \cdot kg^{-1}$, and retained 87% of its capacitance after 5000 cycles at 5 $A \cdot g^{-1}$. These results underscore the synergistic contribution of EEG towards improved electrical conductivity and redox kinetics, while demonstrating the potential of wastewater sludge-derived AC for sustainable electrode development.

Overall, this research integrates synthesis, characterisation, and electrochemical evaluation to elucidate the role of heteroatom-doped EEG in enhancing the electrochemical behaviour of $NiMn(PO_4)_2$-based electrodes. By uniquely combining $NiMn(PO_4)_2$, heteroatom-doped graphene, and waste-derived activated carbon, this study presents an innovative, sustainabilityoriented approach to device design. These findings contribute to the advancement of scalable, sustainable energy storage technologies.

KEYWORDS

i. Energy storage
ii. Hybrid supercapacitors
iii. Activated carbon
iv. Electrochemically exfoliated graphene
v. Nickel-manganese phosphates
vi. Fermi-level shift
vii. Hydrothermal synthesis

TABLE OF CONTENTS

LIST OF FIGURES

LIST OF TABLES

LIST OF ABBREVIATIONS

Abbreviations	**Expansion**
($NiMn(PO_4)_2$	Nickel-manganese phosphate
(LIBs)	Lithium-ion batteries
EDLCs	Electric double-layer capacitors
NMPs	Nickel-manganese phosphates
TMPs	Transition metal phosphates
EEG	Electrochemically exfoliated graphene
$NiMn(PO_4)_2$/EEG	Nickel-manganese phosphate/electrochemically exfoliated graphene
SEM–EDS	Scanning Electron Microscopy with Energy Dispersive X-ray Spectroscopy
XRD	X-ray Diffraction
HR-SEM	High resolution scanning electron microscopy
FTIR	Fourier transform infrared spectroscopy
XPS	X-ray Photoelectron Spectroscopy
CV	Cyclic voltammetry
GCD	Galvanostatic charge-discharge
EIS	Electrochemical impedance spectroscopy
AC	Activated carbon
C	Capacitance
PVA	Polyaniline, polythiophene
HSCs	Hybrid supercapacitors
ΔV	Operating voltage window
V_0	Operating voltage

R_{ES}	Equivalent series resistance
CCCD	Constant current charge-discharge
ESW	Electrochemical stability window
HR-TEM	High-resolution transmission electron microscopy
EDS	Energy Dispersive X-ray Spectroscopy
SEM	Scanning electron microscopy
TEM	Transmission electron microscopy
OPW	Operating potential window
OVW	Operating voltage window
PZV	Potential of zero voltage
CC	Constant current
C_S	Specific capacitance
R_{CT}	Charge-transfer resistance
R_S	Solution resistance
PVDF	Polyvinylidene fluoride
NMP	N-methyl-2-pyrrolidone
H_2SO_4	Sulfuric acid
H_3PO_4	Phosphoric acid
DC	Direct current
CB	Carbon black
rGO	Reduced graphene oxide
CNTs	Carbon nanotubes
EDL	Electric double-layer
AFM	Atomic force microscopy

DR	Double-resonance
TR	Triple-resonance
TO	Transverse optical
LO	Longitudinal optical
HOMO	Highest occupied molecular orbital
LUMO	Lowest unoccupied molecular orbital
WWA	Wastewater sludge
WWTP	Wastewater treatment plant

CHAPTER 1

INTRODUCTION

1.1 Background

Escalating environmental challenges, such as climate change, resource depletion, and energy insecurity, are largely attributed to the long-standing dependence on fossil fuels [1]. These global issues have catalysed a transition towards cleaner and more sustainable energy systems. Renewable sources such as solar and wind power are increasingly being deployed as alternatives; however, their inherent intermittency and variability pose significant obstacles to maintaining a reliable and stable energy supply [2–5].

To address these challenges, advanced energy storage technologies are essential to bridge the gap between energy generation and consumption. Among the leading electrochemical energy storage systems are supercapacitors, rechargeable batteries, and fuel cells. Supercapacitors, in particular, have attracted considerable attention owing to their distinctive features, including high power density, rapid charge-discharge capability (typically within seconds to minutes), excellent thermal tolerance, and outstanding cycling stability exceeding one million cycles [6–8]. These attributes make them particularly suitable for applications such as regenerative braking, uninterruptible power supplies, portable electronics, and renewable energy buffering [6].

Despite these advantages, supercapacitors are inherently constrained by their relatively low energy density. In contrast, lithium-ion batteries (LIBs) offer much higher energy densities, up to approximately 300 Wh Kg^{-1}, but exhibit lower power delivery, slower charging rates, and limited cycle life [6,9]. This performance trade-off has driven growing research interest in alternative energy storage technologies that can integrate the advantages of both systems.

1.2 Hybrid Supercapacitors

To overcome the limitations inherent to individual energy storage technologies, namely the low energy density of supercapacitors and the restricted power density and cycling stability of batteries, hybrid energy storage systems have emerged as a promising solution [10–13]. Commonly referred to as hybrid supercapacitors, supercapatteries, or hybrid electrochemical energy storage devices, these systems are designed to combine the rapid charge-discharge characteristics of electric double-layer capacitors (EDLCs) with the high energy storage capacity of faradaic (battery-type) electrodes [10–18].

As illustrated conceptually in **Figure 1.1(a)**, hybrid devices employ a dual charge storage mechanism: non-faradaic (capacitive) processes at the EDLC electrode and faradaic (pseudocapacitive or battery-like) reactions at the other [14]. This architecture enables the device to achieve both high power and high energy densities simultaneously. The effectiveness of hybrid systems, however, depends heavily on the development of advanced electrode materials exhibiting high surface area, outstanding electrical conductivity, electrochemical durability, and multiple redox-active sites [19].

The growing scientific interest in hybrid systems is evidenced by a marked increase in research publications over the past decade, as shown in **Figure 1.1(b)**. This upward trend highlights the strategic importance of hybrid energy storage systems in next-generation technologies and the continual pursuit of high-performance, multifunctional electrode materials.

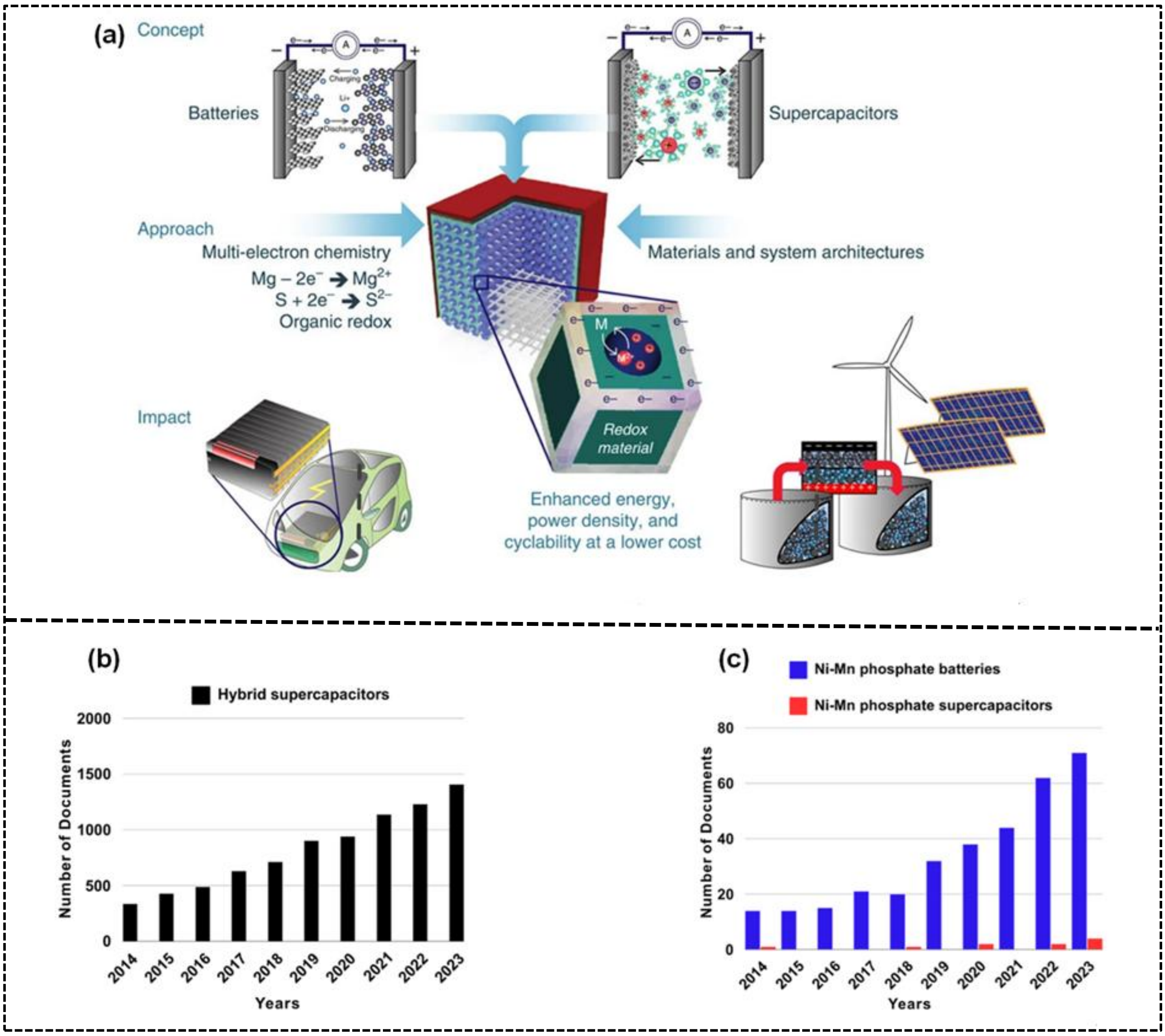

Figure 1.1. (a) Schematic representation of the evolution of integrated battery-supercapacitor systems. Reprinted with permission from Ref. [14], copyright 2016 Springer Nature. (b) Annual publication trends on hybrid supercapacitors, and (c) nickel-manganese batteries and nickel-manganese supercapacitors, based on a Scopus database search of article titles, abstracts, and keywords using the terms “hybrid supercapacitors”, “nickel-manganese batteries”, and “nickel-manganese supercapacitors”.

1.3 Electrode Materials for Hybrid Systems

The selection of suitable electrode materials plays a critical role in determining the efficiency, stability, and overall performance of hybrid devices. Considerable research has been devoted to exploring different classes of materials, including carbon-based nanostructures (such as graphene, carbon nanotubes, and activated carbon), conductive polymers (e.g. polyaniline and polypyrrole), transition metal oxides (such as RuO_2, MnO_2, NiO), and transition metal phosphates (TMPs) such as $Ni_3(PO_4)_2$, $Co_3(PO_4)_2$, and $Mn_3(PO_4)_2$ [3,20–23].

Among these, transition metal phosphates have gained particular attention due to their inherent electrochemical advantages, notably their abundance of redox-active sites, strong chemical stability, and relatively low cost. A subclass of significant interest is nickel-manganese phosphates (NMPs), which provide a synergistic redox mechanism arising from the combined electrochemical contributions of nickel and manganese ions. The phosphate anionic framework further enhances their structural stability and reversibility during charge-discharge processes, making them promising candidates for use in hybrid device architectures [24].

1.4 Nickel-Manganese Phosphates and Graphene Composites

Nickel-manganese phosphates exhibit several advantageous properties that make them attractive for energy storage applications. These include multiple oxidation states conducive to faradaic redox reactions, improved structural stability conferred by the phosphate framework, excellent electrochemical reversibility, and environmental abundance with low toxicity [22,23].

Despite these advantages, a major limitation of NMPs lies in their inherently low electrical conductivity, which restricts charge transport and rate capability. To address this challenge, recent studies have focused on composite engineering, particularly the integration of highly conductive carbonaceous materials such as electrochemically exfoliated graphene (EEG) [25–

27]. Graphene, owing to its ultra-high electrical conductivity, extensive specific surface area (~2600 $m^2 \cdot g^{-1}$), and exceptional mechanical strength, serves as an outstanding conductive matrix. When incorporated into phosphate-based systems, EEG can significantly enhance electron transport pathways, improve electrode-electrolyte interactions, and accelerate electrochemical kinetics [25–27].

Nevertheless, as illustrated in **Figure 1.1(c)**, the application of NMPs, particularly in combination with advanced carbon supports such as EEG, within hybrid device systems remains relatively underexplored. This gap highlights the need for continued research into the rational design and optimisation of NMP/graphene-based nanocomposites for high-performance energy storage.

1.5 Problem Statement

Escalating environmental degradation, energy insecurity, and the rapid progression of climate change, primarily resulting from extensive fossil fuel consumption, have intensified the global pursuit of sustainable and efficient energy technologies. In 2022 alone, fossil fuel consumption accounted for approximately 75% of global energy use, resulting in 33.5 billion tonnes of CO_2 emissions. Renewable energy sources, including solar and wind, are increasingly viable alternatives; however, their intermittency and reliance on variable conditions compromise the stability of the energy supply. Electrochemical energy storage systems, such as supercapacitors, batteries, and fuel cells, are therefore essential for maintaining supply-demand equilibrium.

Each technology presents inherent trade-offs. As illustrated in **Figure 1.2**, the Ragone plot compares the energy and power densities of commercial systems [6]. Lithium-ion batteries dominate the energy storage market due to their high energy density (up to approximately 300 $Wh \cdot kg^{-1}$), but are constrained by moderate cycle life, limited thermal stability, and slow charge kinetics. In contrast, supercapacitors occupy the high-power, low-energy region of the Ragone plot, providing rapid charge-discharge rates, exceptional cycling stability (often exceeding 10^6 cycles), and strong thermal resilience.

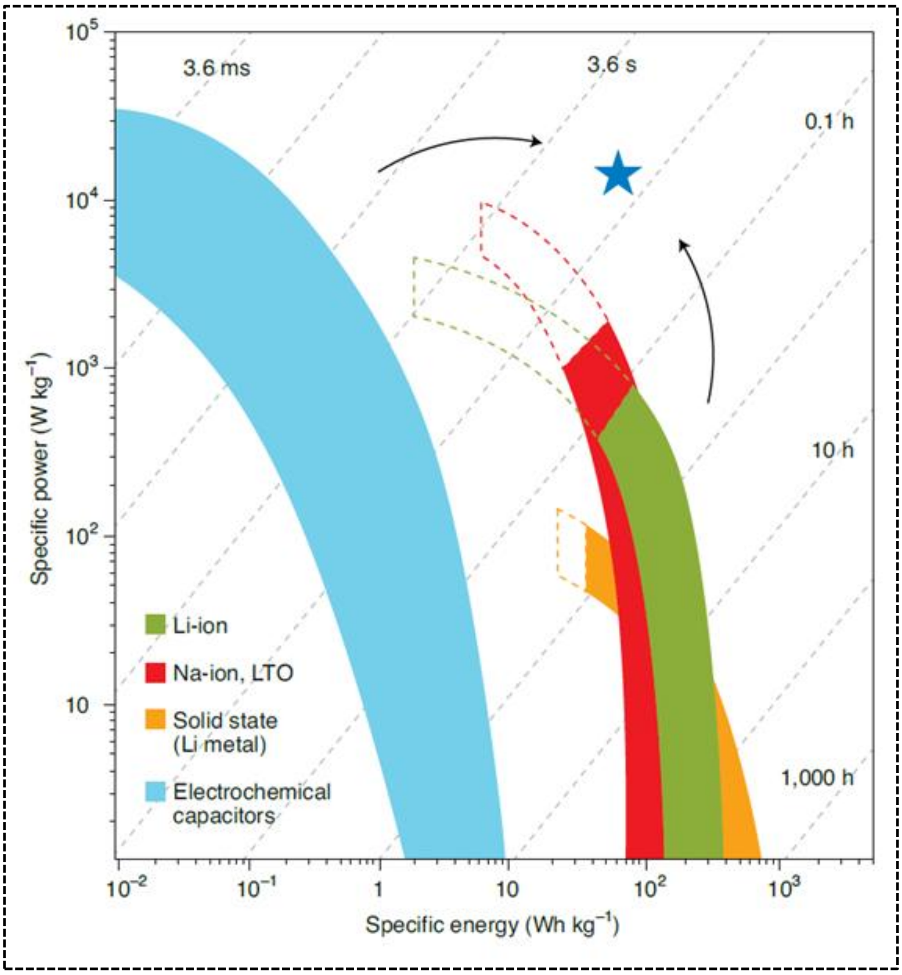

Figure 1.2. Ragone plot illustrating the relationship between power density and energy density for various commercial energy storage devices. Reprinted with permission from Ref [6].

As neither LIBs nor supercapacitors can independently deliver both high energy and high-power densities, a significant performance gap remains, as depicted by the starred region in **Figure 1.2** [6,6,10,12,13]. This gap is characterized by target energy densities in the range of 100 to 300 Wh·kg^{-1} and power densities between 1,000 and 10,000 W·kg^{-1}. These specifications highlight the challenge of creating a storage system that exceeds the capabilities of current technology. This gap has driven the development of hybrid energy storage systems, particularly hybrid supercapacitors, which integrate the complementary features of both technologies within a single device.

Transition metal phosphates, such as nickel-manganese phosphate ($NiMn(PO_4)_2$), have emerged as promising electrode materials, offering multiple oxidation states, stable crystal structures, and environmental benignity[28–30]. However, their low specific surface area, poor intrinsic conductivity, and limited charge transport restrict their energy storage performance[24,31].

Electrochemically exfoliated graphene (EEG) has been identified as a suitable conductive additive to overcome these drawbacks. EEG possesses a high proportion of monolayer graphene (>70%), excellent electrical conductivity, and strong chemical stability, all achieved without the need for chemical reduction steps. When integrated with $NiMn(PO_4)_2$, EEG can substantially improve conductivity, facilitate charge transfer, and enhance electrochemical kinetics and structural durability[32,33].

Despite these theoretical advantages, research on $NiMn(PO_4)_2$/EEG composites in hybrid devices remains limited. Existing studies rarely explore their synergistic behaviour under complete device configurations, revealing a crucial research gap.

This study, therefore, aims to synthesise, characterise, and evaluate a novel $NiMn(PO_4)_2$/EEG nanocomposite electrode for hybrid device applications. The goal is to develop a high-performance system capable of delivering improved energy and power densities, superior cycling stability, and robust structural integrity, thereby contributing to the advancement of next-generation electrochemical energy storage.

1.6 Justification of the Study

Recent literature on the electrochemical performance of nickel- and manganese-based electrode materials highlights the superior specific capacity of nickel-manganese phosphate electrodes, attributed to their high ion-exchange capability, multiple redox-active centres, excellent electrochemical activity, and robust thermal and chemical stability. Morphological design, such as nanosheets, nanorods, or porous architectures, strongly influences ion diffusion pathways and, consequently, overall electrochemical performance. Despite these advantages, transition metal phosphates inherently suffer from low electrical conductivity and limited structural stability. However, these limitations can be mitigated through composite formation with conductive materials such as graphene, which enhances both surface area and charge transport, thereby improving electrochemical characteristics.

The introduction of bimetallic phosphate systems marks a significant advancement in overcoming the limitations of single-metal electrodes. For example, Li *et al.* [28] demonstrated that the incorporation of manganese into the nickel phosphate octahydrate structure enhances electronic conductivity through synergistic redox interactions. This finding underscores the potential of bimetallic phosphate electrodes to deliver superior electrochemical performance. Furthermore, the integration of electrochemically exfoliated graphene (EEG), a material rich in monolayer graphene and exhibiting high intrinsic conductivity without chemical reduction, remains an underexplored yet promising avenue for NiMn phosphate systems. The combination of EEG with NiMn phosphates is expected to significantly improve charge mobility, structural stability, and energy storage capability.

The electrochemical performance of nickel-manganese-based supercapacitor devices reported in the literature indicates that energy and power densities derived from laboratory-scale measurements often overestimate practical device performance. As suggested by previous studies [29,30], realistic values can be obtained by applying a correction factor of approximately five. When adjusted accordingly, the reported maximum energy and power densities of NiMn phosphate-based supercapacitors fall below benchmark values, underscoring the need for further performance enhancement. Consequently, this study proposes the development of a nickel-manganese phosphate/electrochemically exfoliated graphene ($NiMn(PO_4)_2$/EEG) nanocomposite-based hybrid supercapacitor as a next-generation electrode system to overcome these limitations and achieve superior energy storage performance.

1.7 Research Aim and Objectives

1.7.1 Aim

The primary aim of this research is to design and develop a novel nickel-manganese phosphate/electrochemically exfoliated graphene ($NiMn(PO_4)_2$/EEG) nanocomposite electrode for hybrid supercapacitor applications. The study seeks to enhance critical electrochemical parameters energy storage capacity, power and energy densities, and cycling stability through material optimisation and device integration.

1.7.2 Objectives

To achieve this aim, the following specific objectives are outlined:

i. Synthesis of electrochemically exfoliated graphene (EEG) powder and thin film via a two-step intercalation and exfoliation.

ii. Synthesis of nickel-manganese phosphate ($NiMn(PO_4)_2$) and nickel-manganese phosphate/electrochemically exfoliated graphene ($NiMn(PO_4)_2$/EEG) nanocomposites using a hydrothermal autoclave-assisted method.

iii. Characterisation of the structural, morphological, and compositional properties of the synthesised materials using: Scanning Electron Microscopy with Energy Dispersive X-ray Spectroscopy (SEM–EDS), X-ray Diffraction (XRD), High Resolution Scanning

Electron Microscopy (HR-SEM), Fourier Transform Infrared Spectroscopy (FTIR), Raman Spectroscopy, and X-ray Photoelectron Spectroscopy (XPS).

iv. Fabrication and electrochemical evaluation of $NiMn(PO_4)_2$/EEG composite electrodes using a Bio-Logic SP-150 potentiostat/galvanostat, applying techniques such as cyclic voltammetry (CV), galvanostatic charge-discharge (GCD), and electrochemical impedance spectroscopy (EIS).

v. Assembly of a hybrid energy storage device employing the optimised $NiMn(PO_4)_2$/EEG nanocomposite as the active electrode and activated carbon (AC) as the negative electrode.

vi. Device-level electrochemical testing of the fabricated hybrid system, assessing energy and power densities, coulombic efficiency, and long-term cycling stability.

1.8 Research Questions

This study addresses the following key research questions:

i. How does the incorporation of electrochemically exfoliated graphene (EEG) influence the structural, morphological, and electrochemical properties of $NiMn(PO_4)_2$-based electrodes?

ii. How do the quality and distribution of the EEG within the $NiMn(PO_4)_2$/EEG composite affect overall electrochemical performance, including capacitance, conductivity, and cycling stability?

iii. Can the $NiMn(PO_4)_2$/EEG nanocomposite achieve enhanced energy and power densities specifically exceeding ~100 $Wh\cdot kg^{-1}$ and ~1 $kW\cdot kg^{-1}$, respectively, while maintaining long-term cycling stability (~100% retention over 10,000 cycles)?

iv. What is the dominant charge storage mechanism in the $NiMn(PO_4)_2$/EEG composite system, and how does it differ from that of pristine $NiMn(PO_4)_2$?

1.9 Scope and Limitations of this Study

This research focuses on the synthesis, characterisation, and electrochemical evaluation of $NiMn(PO_4)_2$/EEG composites at the laboratory scale, using aqueous and hybrid electrolytes. Device-level optimisation and commercial scalability are beyond the present scope.

1.10 Outline of the Dissertation

This thesis is organised into five chapters, each addressing a critical aspect of the research and collectively guiding the development and evaluation of $NiMn(PO_4)_2$/EEG nanocomposites for hybrid supercapacitor applications:

Chapter 1: Introduction: Presents the background, motivation, problem statement, justification of the study aims, objectives, research questions, and scope.

Chapter 2: Literature Overview on Supercapacitors: Provides an in-depth review of energy storage technologies, focusing on hybrid systems and electrode materials.

Chapter 3: Overview of Characterization Techniques: This section summarizes the key physicochemical and electrochemical techniques used in this study. Structural and morphological analyses were performed using XRD, Raman spectroscopy, FTIR, XPS, SEM-EDS, and TEM, and surface area measurements. Electrochemical performance was evaluated through cyclic voltammetry (CV), galvanostatic charge-discharge (GCD), and electrochemical impedance spectroscopy (EIS).

Chapter 4: Experimental Methods: Describes the synthesis of EEG, $NiMn(PO_4)_2$, and their composites, along with characterisation and electrochemical testing methods.

Chapter 5: Electrochemically Exfoliated Graphene Thin Films: Presents and discusses results, including structural, morphological, and electrochemical analyses of heteroatom-doped electrochemically exfoliated graphene (EEG) powder and thin film.

Chapter 6: Ni-Mn Phosphate/Electrochemically Exfoliated Graphene Composite For Hybrid Supercapacitors: Presents and discusses results, including structural, morphological, and electrochemical analyses of EEG, $NiMn(PO_4)_2$, and $NiMn(PO_4)_2$/EEG composite materials. Additionally, the electrochemical performance of electrodes fabricated from $NiMn(PO_4)_2$ and $NiMn(PO_4)_2$/EEG composites is evaluated and discussed. and evaluates full-device performance.

Chapter 7: Conclusions and Recommendations: Summarises key findings, draws conclusions on the electrochemical viability of the $NiMn(PO_4)_2$//EEG system, and suggests directions for future research and practical implementation.

References

[1] M. Li, M. Li, M. Zhao, B. Wu, S. Mourdikoudis, S. Wei, F.M. Oliveira, J. He, L. Děkanovský, J. Luxa, S. Yang, Z. Sofer, Rational design of crystalline/amorphous nickel manganese phosphate octahydrate heterostructure for high-performance aqueous and all-solid-state asymmetric supercapacitors, Chemical Engineering Journal 482 (2024) 148895. https://doi.org/10.1016/j.cej.2024.148895.

[2] P.K. Katkar, S.A. Patil, J.H. Jeon, H.R. Na, N.S. Padalkar, S.-K. Jerng, S. Lee, S.-H. Chun, Urea-assisted Nickel-Manganese phosphate composite microarchitectures with ultralong lifecycle for flexible asymmetric solid-state supercapacitors: A binder-free approach, Energy & Fuels 36 (2022) 13356–13369. https://doi.org/10.1021/acs.energyfuels.2c02875.

[3] X. Li, A.M. Elshahawy, C. Guan, J. Wang, Metal phosphides and phosphates-based electrodes for electrochemical supercapacitors, Small 13 (2017). https://doi.org/10.1002/smll.201701530.

[4] W. Raza, F. Ali, N. Raza, Y. Luo, K.-H. Kim, J. Yang, S. Kumar, A. Mehmood, E.E. Kwon, Recent advancements in supercapacitor technology, Nano Energy 52 (2018) 441–473. https://doi.org/10.1016/j.nanoen.2018.08.013.

[5] S.N.K., Pavithra, S.M. Jeong, C.S. Rout, MXene–carbon based hybrid materials for supercapacitor applications, Energy Advances 3 (2024) 341–365. https://doi.org/10.1039/D3YA00502J.

[6] P. Simon, Y. Gogotsi, Perspectives for electrochemical capacitors and related devices, Nat. Mater. 19 (2020) 1151–1163. https://doi.org/10.1038/s41563-020-0747-z.

[7] S. Nagamuthu, S. Vijayakumar, S.H. Lee, K.S. Ryu, Hybrid supercapacitor devices based on MnCo 2 O 4 as the positive electrode and FeMn 2 O 4 as the negative electrode, Appl. Surf. Sci. 390 (2016) 202–208. https://doi.org/10.1016/j.apsusc.2016.08.072.

[8] A. Muzaffar, M.B. Ahamed, K. Deshmukh, J. Thirumalai, A review on recent advances in hybrid supercapacitors: Design, fabrication and applications, Renewable and Sustainable Energy Reviews 101 (2019) 123–145. https://doi.org/10.1016/j.rser.2018.10.026.

[9] J. Chen, Jiajun, Recent Progress in Advanced Materials for Lithium Ion Batteries, Materials 6 (2013) 156–183. https://doi.org/10.3390/ma6010156.

[10] M.R. Lukatskaya, B. Dunn, Y. Gogotsi, Multidimensional materials and device architectures for future hybrid energy storage, Nat. Commun. 7 (2016). https://doi.org/10.1038/ncomms12647.

[11] Carbon materials for electrochemical capacitors, J. Power Sources 195 (2010) 7880–7903. https://doi.org/10.1016/J.JPOWSOUR.2010.06.036.

[12] K. Naoi, P. Simon, New Materials and New Configurations for Advanced Electrochemical Capacitors, Journal of The Electrochemical Society (JES) (2008). http://oatao.univ-toulouse.fr/3934/1/Naoi_3934.pdf (accessed May 21, 2016).

[13] P. Simon, Y. Gogotsi, Materials for electrochemical capacitors, Nat. Mater. 7 (2008) 845–854.

[14] M.R. Lukatskaya, B. Dunn, Y. Gogotsi, Multidimensional materials and device architectures for future hybrid energy storage, Nat. Commun. 7 (2016) 12647. https://doi.org/10.1038/ncomms12647.

[15] L. Feng, H. Xue, Advances in transition-metal phosphide applications in electrochemical energy storage and catalysis, ChemElectroChem 4 (2017) 20–34. https://doi.org/10.1002/celc.201600563.

[16] S. Rudra, H.W. Seo, S. Sarker, D.M. Kim, Supercapatteries as Hybrid Electrochemical Energy Storage Devices: Current Status and Future Prospects, Molecules 29 (2024) 243. https://doi.org/10.3390/molecules29010243.

[17] L. Feng, H. Xue, Advances in Transition-Metal Phosphide Applications in Electrochemical Energy Storage and Catalysis, ChemElectroChem 4 (2017) 20–34. https://doi.org/10.1002/celc.201600563.

[18] P. Simon, Y. Gogotsi, Materials for electrochemical capacitors, Nat. Mater. 7 (2008) 845–854.

[19] T. Ma, H. Yang, L. Lu, Development of hybrid battery-supercapacitor energy storage for remote area renewable energy systems, Appl. Energy 153 (2015) 56–62. https://doi.org/10.1016/j.apenergy.2014.12.008.

[20] A. Samal, C. Mohanty, N. Das, R. Das, M.F. Kühnel, A review on metal phosphate based graphene hybrids: Emerging composite materials for vast applications, Mater. Today Chem. 38 (2024) 102096. https://doi.org/10.1016/j.mtchem.2024.102096.

[21] A.A. Mirghni, K.O. Oyedotun, O. Fasakin, B.A. Mahmoud, D.J. Tarimo, N. Manyala, High-performance bimetallic Ni-Mn phosphate hybridized with 3-D graphene foam for novel hybrid supercapacitors, J. Energy Storage 31 (2020) 101584. https://doi.org/10.1016/j.est.2020.101584.

[22] N. Chen, J. Zhou, Q. Kang, H. Ji, G. Zhu, Y. Zhang, S. Chen, J. Chen, X. Feng, W. Hou, Amorphous vanadyl phosphate/graphene composites for high performance

supercapacitor electrode, J. Power Sources 344 (2017) 185–194. https://doi.org/10.1016/j.jpowsour.2017.01.119.

[23] A.A. Mirghni, K.O. Oyedotun, O. Fasakin, B.A. Mahmoud, D.J. Tarimo, N. Manyala, High-performance bimetallic Ni-Mn phosphate hybridized with 3-D graphene foam for novel hybrid supercapacitors, J. Energy Storage 31 (2020) 101584. https://doi.org/10.1016/j.est.2020.101584.

[24] A. Samal, C. Mohanty, N. Das, R. Das, M.F. Kühnel, A review on metal phosphate based graphene hybrids: Emerging composite materials for vast applications, Mater. Today Chem. 38 (2024) 102096. https://doi.org/10.1016/j.mtchem.2024.102096.

[25] P. Forouzandeh, V. Kumaravel, S.C. Pillai, Electrode materials for supercapacitors: A review of recent advances, Catalysts 10 (2020) 969. https://doi.org/10.3390/catal10090969.

[26] M. Sarno, Nanotechnology in energy storage: The supercapacitors, Stud. Surf. Sci. Catal. 179 (2019) 431–458. https://doi.org/10.1016/B978-0-444-64337-7.00022-7.

[27] Z.S. Iro, C. Subramani, S.S. Dash, A brief review on electrode materials for supercapacitor, Int. J. Electrochem. Sci. 11 (2016) 10628–10643. https://doi.org/10.20964/2016.12.50.

[28] S.J. Marje, P.K. Katkar, S.S. Pujari, S.A. Khalate, A.C. Lokhande, U.M. Patil, Regulated micro-leaf like nickel pyrophosphate as a cathode electrode for asymmetric supercapacitor, Synth. Met. 259 (2020) 116224. https://doi.org/10.1016/J.SYNTHMET.2019.116224.

[29] P.K. Katkar, S.J. Marje, S.S. Pujari, S.A. Khalate, P.R. Deshmukh, U.M. Patil, Single-pot hydrothermal synthesis of manganese phosphate microrods as a cathode material

for highly stable flexible solid-state symmetric supercapacitors, Synth. Met. 267 (2020) 116446. https://doi.org/10.1016/J.SYNTHMET.2020.116446.

[30] P.K. Katkar, Z.A. Sheikh, V.D. Chavan, S.W. Lee, In-situ growth of 3D amorphous Ni-Co-Mn phosphate on 2D Ti3C2Tx nanocomposite for commercial-level hybrid energy storage application, J. Mater. Sci. Technol. 206 (2025) 282–296. https://doi.org/10.1016/J.JMST.2024.03.044.

[31] T. Kgwadibane, N.W. Hlongwa, X.G. Fuku, M.J. Madito, Recent advances in nickel-manganese phosphates-based electrodes for hybrid supercapacitors, J. Energy Storage 139 (2025). https://doi.org/10.1016/j.est.2025.118782.

[32] N.S. Mankge, M.J. Madito, N.W. Hlongwa, A.T. Kuvarega, Review of electrochemical production of doped graphene for energy storage applications, J. Energy Storage 46 (2022). https://doi.org/10.1016/j.est.2021.103527.

[33] N.S. Mankge, D.Y. Momodu, N.W. Hlongwa, K. Makgopa, A.T. Kuvarega, M.J. Madito, Hybrid cobalt-nickel oxalate/electrochemically exfoliated doped graphene composite for supercapacitor applications, Synth. Met. 307 (2024) 117652. https://doi.org/10.1016/J.SYNTHMET.2024.117652.

[34] M. Li, M. Zhao, B. Wu, S. Mourdikoudis, S. Wei, F.M. Oliveira, J. He, L. Děkanovský, J. Luxa, S. Yang, Z. Sofer, Rational design of crystalline/amorphous nickel manganese phosphate octahydrate heterostructure for high-performance aqueous and all-solid-state asymmetric supercapacitors, Chemical Engineering Journal 482 (2024). https://doi.org/10.1016/j.cej.2024.148895.

[35] Y. Gogotsi, P. Simon, True Performance Metrics in Electrochemical Energy Storage, Science (1979). 334 (2011) 917–918. https://doi.org/10.1126/science.1213003.

[36] A. Balducci, D. Belanger, T. Brousse, J.W. Long, W. Sugimoto, Perspective—A Guideline for Reporting Performance Metrics with Electrochemical Capacitors: From Electrode Materials to Full Devices, J. Electrochem. Soc. 164 (2017) A1487–A1488. https://doi.org/10.1149/2.0851707jes.

CHAPTER 2

LITERATURE OVERVIEW ON SUPERCAPACITORS

2.1 Introduction

This chapter provides an overview of nickel-manganese phosphate integrated with carbon-based materials for supercapacitors. It begins by introducing electrochemical capacitors, outlining their fundamental operating principles, classifications, and the distinctions between electric double-layer capacitors (EDLCs) and pseudocapacitors. The chapter then discusses the main electrochemical evaluation techniques used to determine capacitance, energy and power densities, and cycling stability, followed by an examination of the vital role played by electrolytes in influencing device performance. The discussion further highlights the significance of metal phosphates as pseudocapacitive materials, focusing on the electrochemical characteristics, advantages, and limitations of nickel-manganese phosphate-based electrodes. Additionally, various synthesis methods and crystal structure aspects that affect their electrochemical behavior are reviewed. To overcome inherent conductivity challenges, the incorporation of carbon-based materials is examined as a strategy to enhance charge transport and stability. Finally, the synergistic interaction between nickel-manganese phosphate and carbon materials is discussed, and existing research gaps are identified to establish the motivation for the present study.

This chapter is published as: T. Kgwadibane et al., J. Energy Storage 139 (2025) 118782.

2.2 Overview of Electrochemical Capacitors

Electrochemical capacitors, commonly referred to as supercapacitors, are energy storage devices that bridge the gap between conventional capacitors and batteries. They combine the high-power density and rapid charge-discharge capability of capacitors with the comparatively high energy density of batteries. Based on their charge storage mechanisms, electrochemical capacitors are broadly classified into two main categories: electric double-layer capacitors (EDLCs) and pseudocapacitors. These mechanisms differ fundamentally in the manner by which charge is stored and released, and their principal characteristics are schematically illustrated in **Figure 2.1**.

In supercapacitor systems, energy storage occurs either through the electrostatic accumulation of charge at the electrode-electrolyte interface or via fast and reversible faradaic redox reactions taking place at or near the surface of the electrode material [1]. On the basis of these distinct mechanisms, supercapacitors are generally categorised into the following types:

i. Electrochemical Double-Layer Capacitors (EDLCs)
ii. Pseudocapacitors, which encompass surface redox and intercalation-type mechanisms [2].

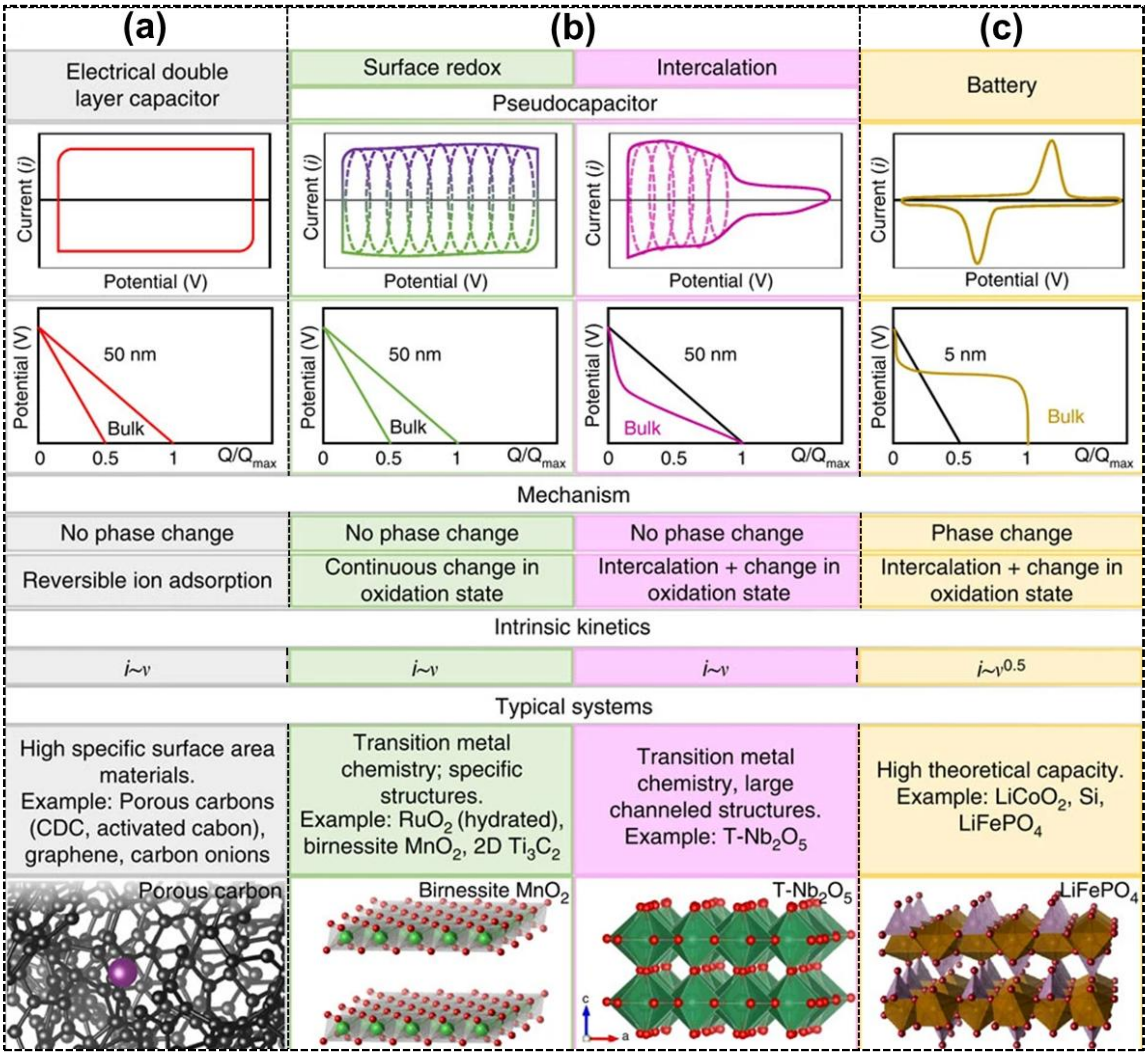

Figure 2.1. Schematic illustration of characteristic charge storage mechanisms in (a) electric double-layer capacitors (EDLCs), (b) pseudocapacitors showing surface redox and intercalation-type processes, and (c) battery-type materials exhibiting distinct electrochemical behavior. Reprinted with permission from Ref. [24], Copyright 2016, Springer Nature.

2.2.1 Electrochemical Double-Layer Capacitors (EDLCs)

EDLCs operate through non-faradaic mechanisms involving the physical adsorption of electrolyte ions onto the surface of high-surface-area and electrochemically stable carbon-based electrodes, such as activated carbon, carbon nanotubes, and graphene [1][3][4,5]. Upon applying a potential, an electric double layer forms at the electrode-electrolyte interface. Electrons accumulate on the electrode surface and are balanced by counter-ions in the electrolyte [1,6,7]. This process is effectively described by the Helmholtz model, where capacitance (C) is defined as:

$$C = \frac{\varepsilon A}{d} \tag{2.1}$$

where ε is the dielectric constant of the medium, A is the surface area of the electrode, and d is the effective thickness of the double layer [4,5].

The performance of EDLCs is highly dependent on surface characteristics, particularly pore structure and accessible surface area. As shown in **Figure 2.1(a)**, EDLCs typically exhibit a rectangular cyclic voltammetry (CV) profile and a triangular galvanostatic charge/discharge (GCD) curve, which are hallmarks of ideal capacitive behavior. Due to the absence of phase changes or redox reactions, EDLCs deliver excellent cycling stability (often >1,000,000 cycles), high-rate performance, and minimal degradation over extended operation [8]. However, their energy density remains inherently low due to the lack of faradaic contributions [9].

2.2.2 Pseudocapacitors

Pseudocapacitors store charge through fast and reversible faradaic redox reactions either at the surface (surface redox) or via ion intercalation within the bulk of the electrode material. This mechanism enables higher energy storage compared to EDLCs due to the involvement of charge transfer reactions. Surface redox pseudocapacitors are based on materials that undergo electron-transfer reactions at or near the surface. These materials may display EDLC-like cyclic voltammetry behavior, but with additional redox peaks corresponding to faradaic activity [10]. Representative materials include transition metal oxides, metal sulfides (e.g., MoS_2, WS_2, FeS_2), and conductive polymers (e.g., polyaniline, polythiophene, PVA) [1,11–14]. In contrast, intercalation-type pseudocapacitors allow for ion insertion into the electrode material without significant crystallographic phase changes. Common examples include TiO_2, Nb_2O_5, and MoO_3. These materials utilize the bulk of the electrode for charge storage, facilitating higher capacitance and energy density while preserving good cycling stability [5,15,16].

Pseudocapacitive materials typically exhibit superior energy storage performance compared to EDLCs, while still maintaining good rate capability and durability [17–19]. However, their performance is strongly influenced by the material's nanostructure, electrical conductivity, and ion transport dynamics.

2.2.3 Battery-Type Faradaic Reactions

In battery-type electrodes, energy storage is governed by diffusion-controlled redox reactions involving bulk ion transport and lattice structure modifications. These systems exhibit behaviors akin to conventional batteries and rely on solid-state ion diffusion. Typical materials include transition metal oxides/hydroxides, metal sulfides/selenides, and phosphates, particularly when operated in alkaline electrolytes [8]. These materials are characterized by phase transitions during charge/discharge, resulting in distinct redox peaks in CV and flat plateaus in GCD curves, as illustrated in **Figure 2.1(c)** [3,20–22]. The current response (i) in these systems follows a square root dependency on scan rate ($i{\sim}v^{0.5}$), indicative of semi-infinite diffusion control [8].

2.2.4 Hybrid Supercapacitors

Hybrid supercapacitors (HSCs) aim to bridge the gap between batteries and traditional capacitors by integrating two distinct types of electrodes: one capacitive (e.g., carbon-based) and one faradaic (e.g., transition metal compound) [23]. This asymmetric configuration enables HSCs to achieve a broader operating voltage window (ΔV), higher energy density, and improved rate performance [3,20–22]. In HSCs, the faradaic electrode contributes significantly to the energy storage capacity through redox processes, while the EDLC-type electrode ensures rapid charge/discharge and structural stability. The synergistic effect of combining these two charge storage mechanisms results in a device capable of delivering both high energy and high power, making HSCs ideal for advanced applications in flexible, portable, and grid-level storage systems.

2.3 Performance Evaluation of Electrochemical Capacitors

The electrochemical performance of hybrid supercapacitors is typically assessed through several key parameters that collectively determine their energy storage efficiency, rate capability, and operational stability. According to Zhang and Pan et al. [25], the most critical metrics for evaluating both working electrodes (half-cells) and assembled devices (full cells) include capacitance, operating voltage (V_0), and equivalent series resistance (R_{ES}). These parameters directly influence the energy density and power density of the supercapacitor system [25]. Additional factors such as time constant, charge-discharge efficiency, and cycling stability are also vital, especially in the context of long-term operational reliability and commercial scalability. These performance metrics are strongly affected by electrode composition, morphology, and cell configuration, as well as by the physicochemical properties of the electrolyte.

As illustrated in **Figure 2.2,** the influencing parameters are represented in light purple, while the corresponding test methodologies are indicated in white. Among the commonly employed electrochemical techniques are:

i. Cyclic Voltammetry (CV): Used to evaluate redox behavior, capacitive response, and charge-discharge reversibility.
ii. Galvanostatic Charge-Discharge (GCD): Provides quantitative data on specific capacitance, energy density, power density, and cycling performance.

iii. Electrochemical Impedance Spectroscopy (EIS): Offers insights into charge transfer resistance, ion diffusion behavior, and internal resistance of the system.

These techniques collectively provide a comprehensive understanding of the supercapacitor's behavior under various operating conditions. The parameters obtained from CV, GCD, and EIS measurements form the foundation for calculating the overall electrochemical efficiency and reliability of supercapacitors.

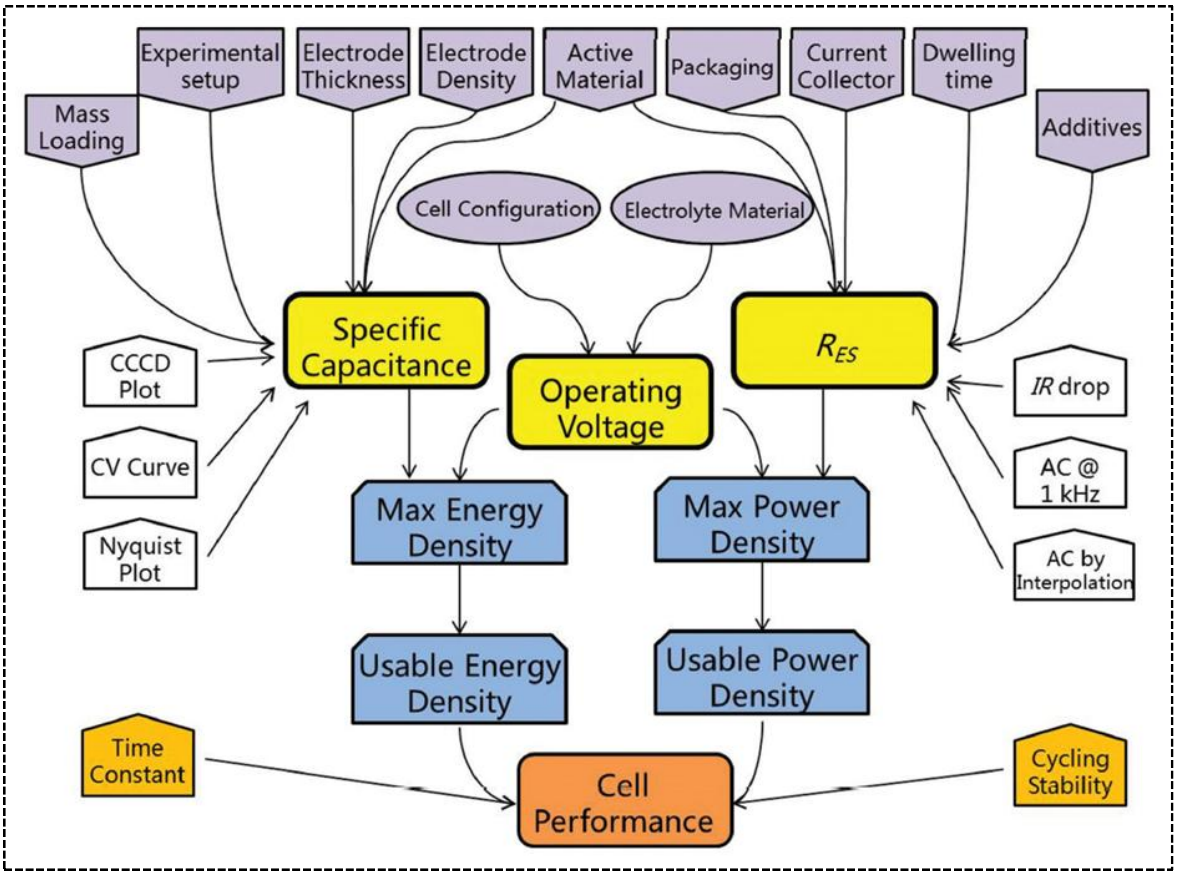

Figure 2.2. Schematic representation of major performance parameters, influencing factors, and associated electrochemical methods employed in evaluating supercapacitor performance. Reprinted with permission from Ref. [50].

2.3.1 Cyclic Voltammetry

The potential range over which the voltage is swept is referred to as the operating potential window (V_0), and the rate of potential change is termed the scan rate (typically in mV s^{-1}). The instantaneous current response during anodic and cathodic sweeps reflects the underlying redox reactions and charge storage mechanisms. Furthermore, CV testing is widely employed to determine the appropriate operating potential window for electrode materials and to assess the reversibility of the charge-discharge processes [26,27].

2.3.2. Galvanostatic Charge-Discharge

Galvanostatic charge-discharge (GCD), also known as constant current charge-discharge (CCCD) testing, is one of the most used methods for evaluating supercapacitors under direct current conditions [28]. In this technique, the cell or electrode is charged and discharged at a constant current while maintaining a predetermined maximum potential (V_0). The output is a potential versus time curve, from which key electrochemical parameters such as specific capacity, specific capacitance, energy density, power density, and cycling stability can be extracted.

This method provides highly reproducible data and is particularly valuable for assessing the rate capability and long-term performance of supercapacitor electrodes. All three fundamental parameters shown in **Figure 2.2,** capacitance, operating voltage, and internal resistance, can be derived from GCD data and subsequently used to calculate related performance metrics. For hybrid supercapacitors employing both capacitive and battery-type electrodes, it is essential to calculate the specific charge (C g^{-1}), specific capacity (mAh g^{-1}), and specific capacitance (F g^{-1}) from the discharge portion of the GCD curve using equations (2.2-2.4), respectively.

$$\text{Specific charge} = \frac{Q}{3.6} = \frac{I\times\Delta t}{3.6} \qquad (2.2)$$

where Q is the total charge stored (coulombs). This charge is calculated by ($Q = \int i \times t$), I is the current density (A/g), and Δt is the discharge time (s) [29]:

$$\text{Specific capacity (mAh g}^{-1}) = \frac{\mathrm{Q}}{\mathrm{m}} = \frac{i\,\Delta t}{m} \tag{2.3}$$

$$\text{Specific capacitance (F g}^{-1}) = \frac{\text{Specific capacity} \times 3600}{\Delta V} \tag{2.4}$$

where ΔV is the potential window (V) of the electrode in the three-electrode configuration.

In hybrid systems, one electrode behaves predominantly capacitive, while the other follows a battery-type faradaic mechanism. Since their potential ranges and charge-storage capacities differ, maintaining charge balance ($Q^+ = Q^-$) between the positive and negative electrodes is crucial for achieving maximum cell potential and energy density. The optimized mass ratio between electrodes is determined using equation (2.5) [30–35]:

$$\frac{m_+}{m_-} = \frac{C_- \times \Delta V_-}{C_+ \times \Delta V_+} \tag{2.5}$$

where C_+ and C_- represent the specific capacitances, and ΔV_+ and ΔV_- are the potential windows of the positive and negative electrodes, respectively.

The energy density (E_d) and power density (P_d) were calculated from the GCD profiles using [32,33]:

$$E_d\ (Wh\ \mathrm{kg}^{-1}) = \left(\frac{I}{m}\right)\frac{\int V(t)dt}{3.6} \tag{2.6}$$

$$P_d(W\ \mathrm{kg}^{-1}) = \frac{3.6\ E_d}{\Delta t} \tag{2.7}$$

where I/m is the specific current (A/g), $\int V(t)dt$ is the integral of the discharge curve and Δt is the discharge time (s).

2.3.3 Electrochemical Impedance Spectroscopy

Electrochemical impedance spectroscopy (EIS) is a frequency-domain technique used to evaluate the impedance response of a supercapacitor. The data are typically represented as Nyquist plots (imaginary impedance Z''versus real impedance Z') and Bode plots (phase angle versus frequency) [25,36,37].

In a Nyquist plot, the high-frequency intercept on the real axis corresponds to the equivalent series resistance (R_{ES}), which is a key determinant of power capability and energy efficiency. Modeling of the impedance spectra through equivalent circuit analysis provides further insight into charge transfer resistance, ion diffusion, and capacitive behavior within the electrode–electrolyte system [66–68]. EIS can also be used to estimate capacitance, energy, and power performance by fitting frequency-dependent data [38,39].

2.3.4 Cycling Stability and Time Constant

Long-term stability is one of the most desirable features of supercapacitors, with advanced devices demonstrating cycle lives exceeding 10^6 charge-discharge cycles. The capacitance retention is typically calculated from GCD data by comparing the capacitance after thousands of cycles with its initial value.

Another key dynamic parameter is the time constant (τ), which quantifies how rapidly a device can deliver stored energy. It is defined as the product of the equivalent resistance and total capacitance of the cell, as given by:

$$\tau = R_{ES} \times C_T \tag{2.8}$$

A smaller τ value indicates faster response and better power delivery. In commercial supercapacitors, τ generally ranges between 0.5 and 3.6 s, reflecting their rapid charge–discharge characteristics [40].

2.4 Role of Electrolytes in Electrochemical Capacitors

Electrolytes are essential components in electrochemical energy storage systems, directly influencing energy density, power density, ionic conductivity, and cycling stability. The electrochemical stability window (ESW) determines the maximum operating voltage, and since energy density ($E = \frac{1}{2} CV^2$) scales quadratically with voltage, electrolyte selection critically defines device performance. Key electrolyte properties ion mobility, conductivity, viscosity, and electrode compatibility, also govern internal resistance, charge transfer kinetics, and long-term stability [41].

Electrolytes are generally categorized as aqueous or non-aqueous, each offering distinct advantages. Aqueous electrolytes, acidic (H_2SO_4, HCl), alkaline (KOH, NaOH, LiOH), and neutral (Na_2SO_4, Li_2SO_4, $NaNO_3$) are widely used due to high ionic conductivity and low cost. Acidic systems provide high proton conductivity (~0.8 S cm^{-1} for 1 M H_2SO_4 at 25 °C) but can corrode metal-based electrodes. Alkaline electrolytes, particularly KOH (~0.6 S cm^{-1} for 6 M at 25 °C), enable fast redox reactions in transition metal oxides and phosphates, achieving capacitances >2000 F g^{-1} in optimized composites [41]. However, long-term cycling may cause surface oxidation and dissolution. Neutral electrolytes offer moderate conductivity and wider potential windows (~1.6 V), improving durability (>90 % retention after 10 000 cycles) while reducing corrosion [41].

Non-aqueous electrolytes, including organic solvents (e.g., acetonitrile, propylene carbonate) and ionic liquids, expand the ESW to 2.5 - 4 V, enhancing energy density. Their drawbacks include low conductivity, higher cost, and safety risks for organics; ionic liquids offer non-volatility and stability but suffer from high viscosity and expense.

Comparative studies show that carbon-based electrodes perform best in acidic media, while transition-metal phosphates, such as Ni-Mn phosphates, excel in alkaline electrolytes due to superior redox kinetics and ion mobility [41]. Neutral electrolytes balance these effects, enabling longer life and moderate voltage operation ideal for hybrid supercapacitors. Nonetheless, balancing voltage stability and ionic resistance remains challenging. Future directions include tailored electrolytes with redox additives, hybrid solvent systems, and gel polymer matrices to improve conductivity, voltage range, and electrode compatibility for next-generation high-performance hybrid supercapacitors.

2.5 Metal Phosphates in Electrochemical Capacitors

In the past decade, considerable attention has been devoted to the development and performance evaluation of nickel-manganese phosphate ($NiMn(PO_4)_2$) electrodes and their composites with carbonaceous materials, especially graphene, for supercapacitor applications [91,95–98]. This section reviews key experimental studies that have demonstrated the influence of synthesis conditions, morphological engineering, and hybridization strategies on electrochemical behavior.

2.5.1 Electrochemical Performance of Nickel-Manganese Phosphate-Based Electrodes

Septiani et al. synthesized amorphous nickel phosphate nanotubes ($NiHPO_4{\cdot}3H_2O$) using nickel glycerate templates via a solvothermal approach **(Figure 2.3(a))** [42]. Among the calcined samples, NiHPi-500 exhibited the highest specific capacitance of 502 F g^{-1} at 0.5 A g^{-1}, attributed to its improved electrical conductivity and enlarged surface area, while maintaining 94.8% capacitance retention after 5000 cycles. The corresponding asymmetric supercapacitor (NiHPi-500//AC) achieved an energy density of 50 Wh kg^{-1} with excellent cycling stability **(Figures 2.3(b,c))** [42]. Likewise, Raissa et al. prepared nickel phosphate (NiP) via a hydrothermal route and reported that the sample calcined at 600 °C delivered the best performance, with a specific capacity of 516 C g^{-1} at 0.62 A g^{-1} and an energy density of 52 Wh kg^{-1} in an asymmetric device [43].

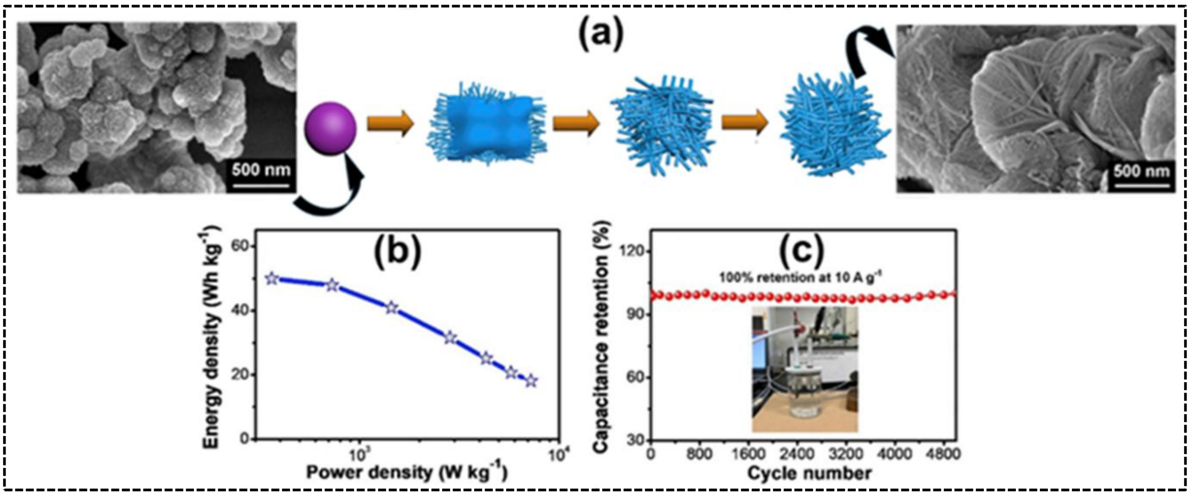

Figure 2.3. (a) Schematic illustration of the formation mechanism of nanotube-assembled nickel phosphate-based 2D architectures with corresponding morphology images. (b) Ragone plot of the assembled device. (c) Cycling stability performance of the device. Reprinted with permission from Ref. [42], Copyright 2020, Elsevier.

In another study, Omar et al. synthesized nickel phosphate ($Ni_3(PO_4)_2$) electrodes via a sono-chemical method, followed by calcination at 300 °C (N300), 600 °C (N600), and 900 °C (N900) **(Figure 2.4(a))** [44]. Increasing calcination temperature led to particle coarsening and reduced electrochemical activity. Among the samples, N300 exhibited the highest specific capacity of 620 C g^{-1} at 0.4 A g^{-1}, outperforming N600 (46 C g^{-1}) and N900 (14 C g^{-1}) **(Figures 2.4(b–d))**. The superior performance of N300 was attributed to its amorphous nature and abundance of electroactive sites. The corresponding asymmetric supercapacitor (N300//AC, **Figure 2.4(e)**) operated within 0 - 1.45 V, achieving an energy density of 76 Wh kg^{-1} at 599 W kg^{-1} and retaining 88.5% of its capacity after 3000 cycles **(Figures 2.4(f,g))** [101]. Furthermore, manganese phosphate ($Mn_3(PO_4)_2·3H_2O$) nanosheets fabricated by Dai et al. showed pseudocapacitive behavior [45]. Among the samples treated at 450, 600, and 750 °C, the M2 electrode achieved the highest specific capacitance (~380 F g^{-1} at 0.5 A g^{-1}). An asymmetric cell with M3 as the positive electrode achieved an energy density of 32.32 Wh kg^{-1} at 4250 W kg^{-1}.

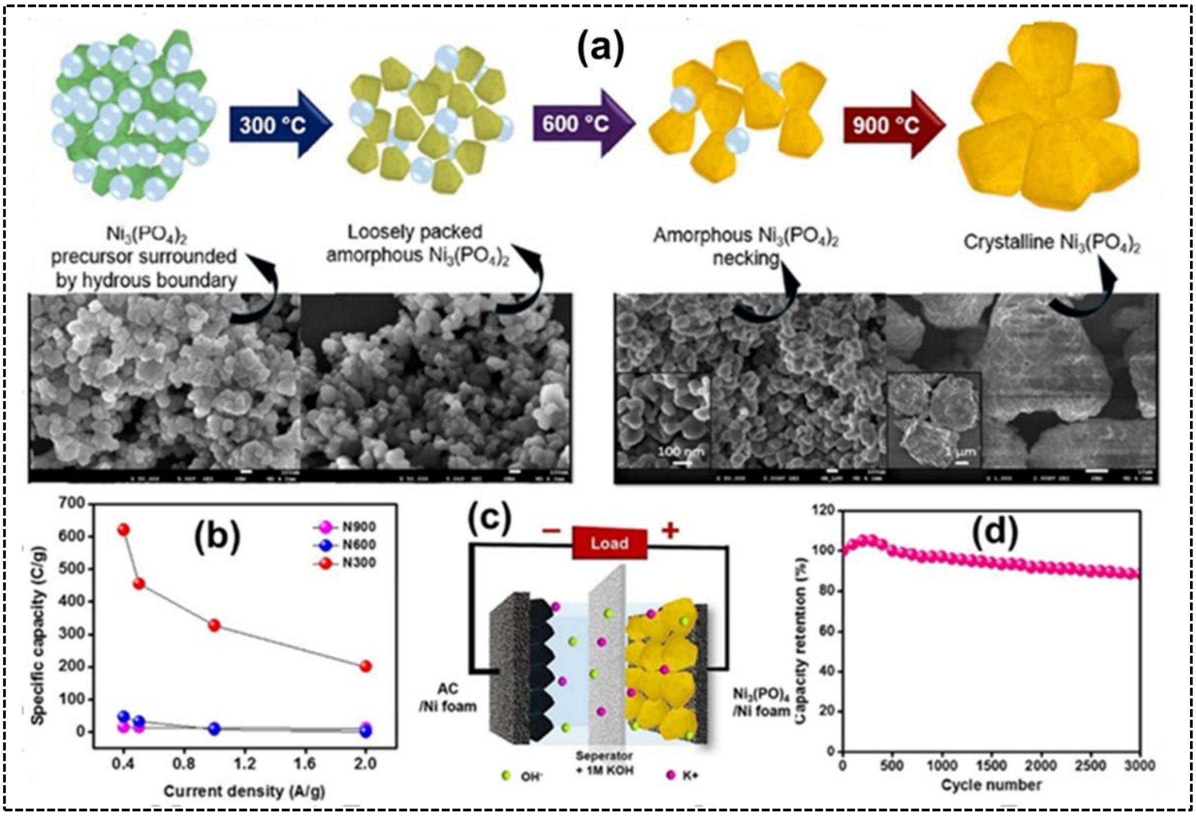

Figure 2.4. (a) Schematic illustration of the formation mechanism of N0, N300, N600, and N900 at different calcination temperatures with corresponding morphology images. (b) Specific capacity comparison of N300, N600, and N900 electrodes. (c) Schematic representation of the assembled device. (d) Cycling stability performance of the device. Reprinted with permission from Ref. [44], Copyright 2016, Royal Society of Chemistry.

A comparative summary in **Table 2.1** highlights how nano-architectures such as nanotubes and nanosheets significantly improve ion diffusion and active site accessibility. These benefits, combined with the inherent chemical stability of phosphate-based frameworks due to strong P-O bonds, support their promise as durable and high-performance electrode materials for supercapacitors.

Table 2.1. Electrochemical performance of recently reported metal phosphate-based electrode materials.

Electrode materials	**Morphology**	**Electrolyte**	**Potential window**	**Specific capacity/capacitance**	**Cycles (Stability)**	**Ref.**
$NiHPO_4 \cdot 3H_2O$	2D sheet-like	1 M KOH	0.0 - 0.45 V/Ag/AgCl	502 F/g at 0.5 A/g	5000 (94.8%) at 10A/g	[42]
$Ni_3(PO_4)_2$	Particles (amorphous)	1 M KOH	0.0 - 0.45 V/Ag/AgCl	608 C/g at 0.4 A/g	-	[44]
Nickel phosphate	Rod shape	2 M KOH	0.0 to 0.5 V/Ag/AgCl	516 C/g at 0.62 A/g	-	[43]
$Ni_3(PO_4)_2 \cdot 8H_2O$	Microsheets	1 M KOH	0.0 - 0.5 V/SCE	471 C/g at 0.5 mA/cm^2	-	[46]
$Mn_3(PO_4)_2 \cdot 3H_2O$	Nanosheets	2 M KOH	-0.3 to 0.5 V/SCE	~380 F/g at 0.5 A/g	2000 (~60%) at 2A/g	[45]
Graphene-$Mn_3P_2O_8$	Micro-rods	6 M KOH	0.0 - 0.4 V/Ag/AgCl	345.4 F/g (38.4 mA h/g) at 0.5 A/g	5000 (~100%) at 5A/g	[47]
$Mn_3(PO_4)_2$/graphene foam	Micro-rods	6 M KOH	0.0 - 0.4 V/Ag/AgCl	270 F/g at 0.5 A/g	1000 (~99%) at 5A/g	[48]
$Mn_3(PO_4)_2$	Nanosheets	2 M KOH	-0.5 - 0.6 V/SCE	203 F/g at 0.5 A/g	10000 (91.1%) at 1.0 A/g	[49]
$NaNiPO_4$	Nanosheets	2 M NaOH	0.0 to 0.6 V/Hg/HgO	125 F/g at 0.1 A/g	2000 (99%) at 1A/g	[50]
$Ni_{11}(HPO_3)_8(OH)_6$	Hexagonal polyhedrons	3 M KOH	0.0 - 0.5 V/SCE	295 F/g at 0.625 A/g	1000 (99.3%) at 0.625A/g	[51]
$Ni_3(PO_4)_2$/graphene foam	Nano-rods	6 M KOH	0.0 - 0.4 V/Ag/AgCl	462 F/g at 0.5 A/g	2000 (92%) at 10A/g	[52]

2.5.2 Advantages and Drawbacks of Nickel-Manganese Phosphates

Nickel-manganese phosphates (NMPs) possess a unique combination of physicochemical and electrochemical properties that make them promising electrode materials for hybrid supercapacitors. Compared with other transition-metal phosphates and oxides, they offer a balanced synergy of redox activity, chemical stability, and tunable composition **(Figure 2.5)**.

Advantages of Nickel-Manganese Phosphates:

i. Synergistic redox activity: The coexistence of Ni^{2+}/Ni^{3+} and $Mn^{2+}/Mn^{3+}/Mn^{4+}$ redox couples enable multiple faradaic reactions, resulting in high specific capacitance and energy density [47,53,54].
ii. Structural stability: Strong P–O covalent bonds in the phosphate lattice minimize metal ion dissolution and suppress phase collapse during cycling, enhancing durability [54–56].
iii. Abundance and sustainability: Ni, Mn, and phosphate precursors are cost-effective, widely available, and environmentally benign alternatives to Ru- or Co-based materials [57–62].
iv. Compositional flexibility: Adjusting the Ni/Mn ratio tunes electrochemical performance Mn improves redox activity, while Ni enhances conductivity and mechanical strength [53,54,63].

Despite their advantages, NMP electrodes face several challenges (**Figure 2.5**):

i. Low electronic conductivity: The phosphate framework limits charge transport, often necessitating conductive additives such as graphene, CNTs, or MXenes [48,52,64–66].
ii. Structural degradation: Repeated ion insertion/extraction induces mechanical strain, phase transitions, and agglomeration, reducing cycling stability [45,49,54].
iii. Complex synthesis: Achieving nanoscale, phase-pure materials often require multi-step or high-temperature synthesis, hindering scalability [67–69].
iv. Performance trade-offs: Increasing Mn content enhances capacitance but may accelerate degradation without structural stabilization [47,63,70].

Overall, the redox versatility, stability, and tunability of Ni-Mn phosphates make them strong candidates for next-generation hybrid supercapacitors. However, addressing their low conductivity and structural fragility requires innovative design strategies such as carbon hybridization, bimetallic integration, and controlled synthesis optimization to fully realize their electrochemical potential [47,63,71,72].

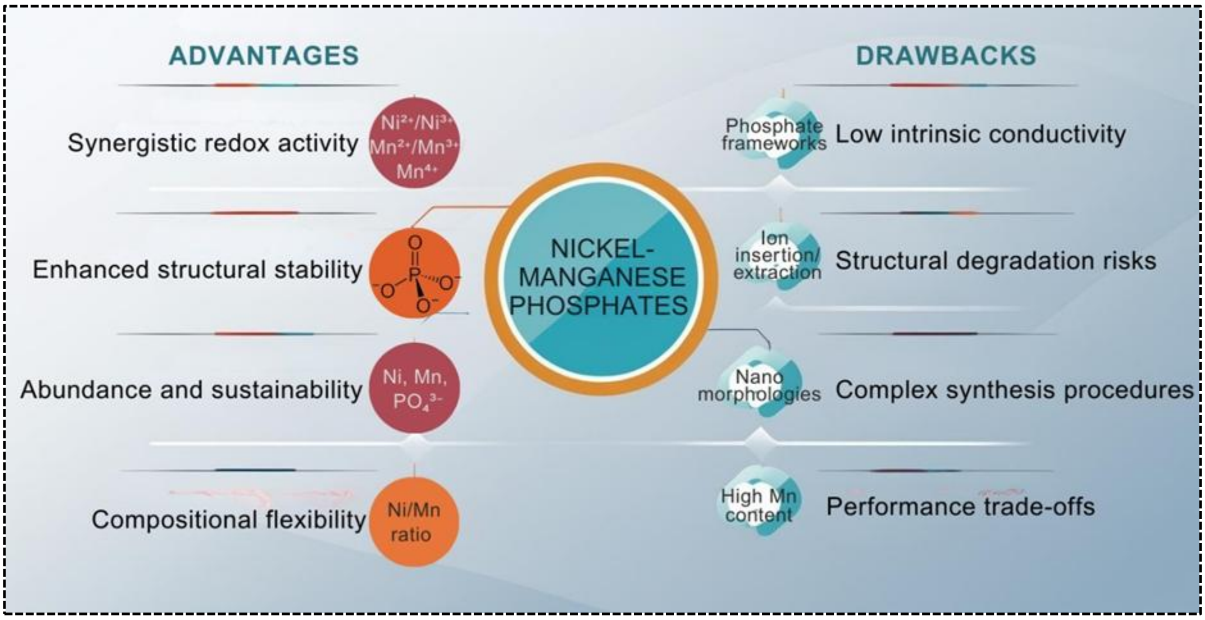

Figure 2.5. Schematic summary illustrating the key advantages and inherent limitations of nickel-manganese phosphates

2.5.3 Synthesis Strategies for Nickel-Manganese Phosphate-Based Electrodes

The synthesis method plays a critical role in defining the structural, morphological, and electrochemical characteristics of nickel-manganese phosphate (Ni-Mn phosphate) materials used in hybrid supercapacitors. These methods are generally categorized into two broad approaches: top-down, which involves breaking down bulk materials into nanostructures using mechanical or chemical treatments, and bottom-up, which builds nanostructures atom by atom or molecule by molecule through controlled chemical reactions. Each strategy offers unique advantages in tailoring properties at the nanoscale [58,73,74].

2.5.3.1 Hydrothermal and Solvothermal Synthesis

Hydrothermal and solvothermal methods are widely adopted for producing mono-, bi-, and tri-metallic phosphates. These techniques involve reacting metal salts and phosphate precursors under high-pressure and high-temperature conditions in sealed Teflon-lined autoclaves [69] [70]. [71]. This method is favored for its ability to yield high-purity, homogeneous materials with controllable morphology and surface area factors critical for optimizing ion diffusion and redox kinetics in supercapacitors. Moreover, it is considered environmentally benign due to water-based solvents and minimal use of organic reagents [75].

2.5.3.2 Chemical Precipitation

The chemical precipitation method is a simple, scalable route for producing Ni-Mn phosphate materials with tunable composition and morphology. It involves the reaction between metal salts and phosphate precursors in solution, followed by product recovery through filtration, washing, and drying. By adjusting synthesis parameters such as pH, temperature, and precursor concentrations, researchers can obtain materials with controlled crystalline and particle size [76].

2.5.3.3 Sono-chemical Synthesis

Sono-chemical synthesis utilizes high-frequency ultrasound waves to generate localized high-temperature and high-pressure environments via acoustic cavitation. This technique promotes the rapid nucleation and formation of nanocrystals with enhanced surface area and porosity, ideal for supercapacitor applications [77][78].

2.5.3.4 Microwave-Assisted Synthesis

Microwave-assisted synthesis offers a fast, energy-efficient alternative to conventional heating techniques. It provides uniform thermal distribution, facilitating the formation of highly crystalline and porous nanostructures in shorter durations [79] [80].

Each synthesis technique presents its own benefits and trade-offs in terms of reaction time, scalability, material quality, and cost. **Table 2.2** provides a comparative summary of these methods and their key characteristics relevant to the preparation of high-performance phosphate-based electrodes for hybrid supercapacitors.

As summarized in **Table 2**, the various synthesis methods enable precise control over the morphology, porosity, and crystallinity of nickel-manganese phosphate materials. Hydrothermal and solvothermal approaches provide excellent structural control, producing high-purity and well-defined nanostructures. Chemical precipitation offers simplicity, scalability, and cost-effectiveness, while sono-chemical synthesis enables rapid formation of hybrid composites with enhanced electrochemical performance. Microwave-assisted synthesis provides fast, energy-efficient processing, making it suitable for large-scale production. Current research focuses on optimizing these methods for sustainable, scalable fabrication and on integrating conductive frameworks to overcome the intrinsic conductivity limitations of phosphates. Such advancements are vital for translating laboratory-scale nickel-manganese phosphate electrodes into practical, high-performance hybrid supercapacitor devices.

Table 2.2: Comparison of synthesis methods for transition metal phosphate-based electrode materials.

Method	**Reaction Conditions**	**Advantages**	**Limitations**	**Typical Morphologies**	**Electrochemical Highlights**
Hydrothermal/ Solvothermal	High temperature and pressure in sealed autoclaves	- High crystallinity - Tunable morphology - Eco-friendly solvents	- Long reaction time - Requires high-pressure vessels	Nanorods, nanowires, nanosheets	Co-Mn phosphate: 571 F/g, 88% retention over 8000 cycles [69].
Chemical Precipitation	Mild conditions; aqueous media; pH- and concentration-controlled	- Simple and cost-effective - Scalable -Morphology control	- Post-synthesis treatment is often required - Potential for inhomogeneity	Nanoparticles, nanowires, and nanoflakes	$Ni_2P_2O_7$ nanowires: 772.5 F/g, 94% retention over 3 000 cycles [81]. $Co_3(PO_4)_2$ flakes: 132 and 210 F/g, >95% retention over 800 cycles [82].

Sono-chemical	Ultrasonic irradiation; ambient to mild heating	- Rapid synthesis - High surface area - Enables hybrid composites	- Scale-up difficulty - Requires ultrasonic equipment	Nanospheres, porous composites	Zn-Co-Mn: 1022 C/g, 45 Wh/kg [78]. Co-Cu-Mn: 340 C/g, 90% retention [77].
Microwave-Assisted	Microwave radiation for uniform, fast heating	- Short reaction time - Energy-efficient - Uniform particle growth	- Limited to microwave-absorbing systems - Higher equipment cost	Porous, crystalline nanostructures	NiO: 370 F/g (vs. 101 F/g via reflux) [79]. COMAP with enhanced performance

2.5.4 Crystal Structure Considerations for Nickel-Manganese Phosphate Electrodes

The crystal structure of electrode materials significantly influences their electrochemical behavior, especially in the context of hybrid supercapacitors. Nickel-manganese phosphate-based compounds are particularly attractive due to their strong coordination between metal centers and phosphate ligands, which promotes high chemical and structural stability. Their open-framework architectures facilitate rapid ion diffusion and efficient charge transfer during redox reactions, enhancing their suitability for pseudocapacitive applications [83]. These materials often display flexible coordination geometries and variable oxidation states, supporting robust redox activity and resilience under cycling. The phosphate functional groups contribute to reversible structural transformations, improving long-term stability and performance [58,84].

Liu et al. systematically investigated a series of lithium-rich spinel materials with the general formula $Li_{1+x}Ni_{0.05}Mn_{1.95-x}O_4$ ($0 \leq x \leq 0.10$), synthesized via a solution combustion method, to examine the relationship between composition, crystal structure, morphology, and electrochemical performance **(Figure 2.6)** [56]. X-ray diffraction (XRD) analysis confirmed high phase purity and sharp reflections characteristic of the cubic spinel structure (space group $Fd\bar{3}m$, JCPDS No. 35-0782) across all samples. As illustrated in **Figure 2.6(a)**, increasing Li content caused a systematic shift of the (440) diffraction peak toward higher 2θ values, signifying progressive lattice contraction. This structural change results from the substitution of larger Mn^{3+} ions (≈0.072 nm) by smaller Mn^{4+} ions (≈0.067 nm) and shorter Li-O bonds (≈0.195 nm), leading to reduced unit cell volume and improved mechanical stability.

Li doping also affected crystal orientation, as shown in **Figure 2.6(b)**, where the intensity ratios I(111)/I(400) and I(111)/I(440) varied with Li concentration, indicating preferred crystal growth along the (400) and (440) planes. The optimized LNMO-0.02 sample exhibited uniform truncated octahedral morphology (average particle size ≈200 nm) observed by TEM (**Figure 2.6(c))**, with distinct lattice fringes corresponding to the (111) plane confirmed through HRTEM and SAED analyses (Figure 4(d)). The atomic-scale model in Figure 4(e) depicts Li^+ transport pathways across the (111), (100), and (110) crystal facets-where (111) planes reduce Mn dissolution, while (100) and (110) promote rapid ion transport.

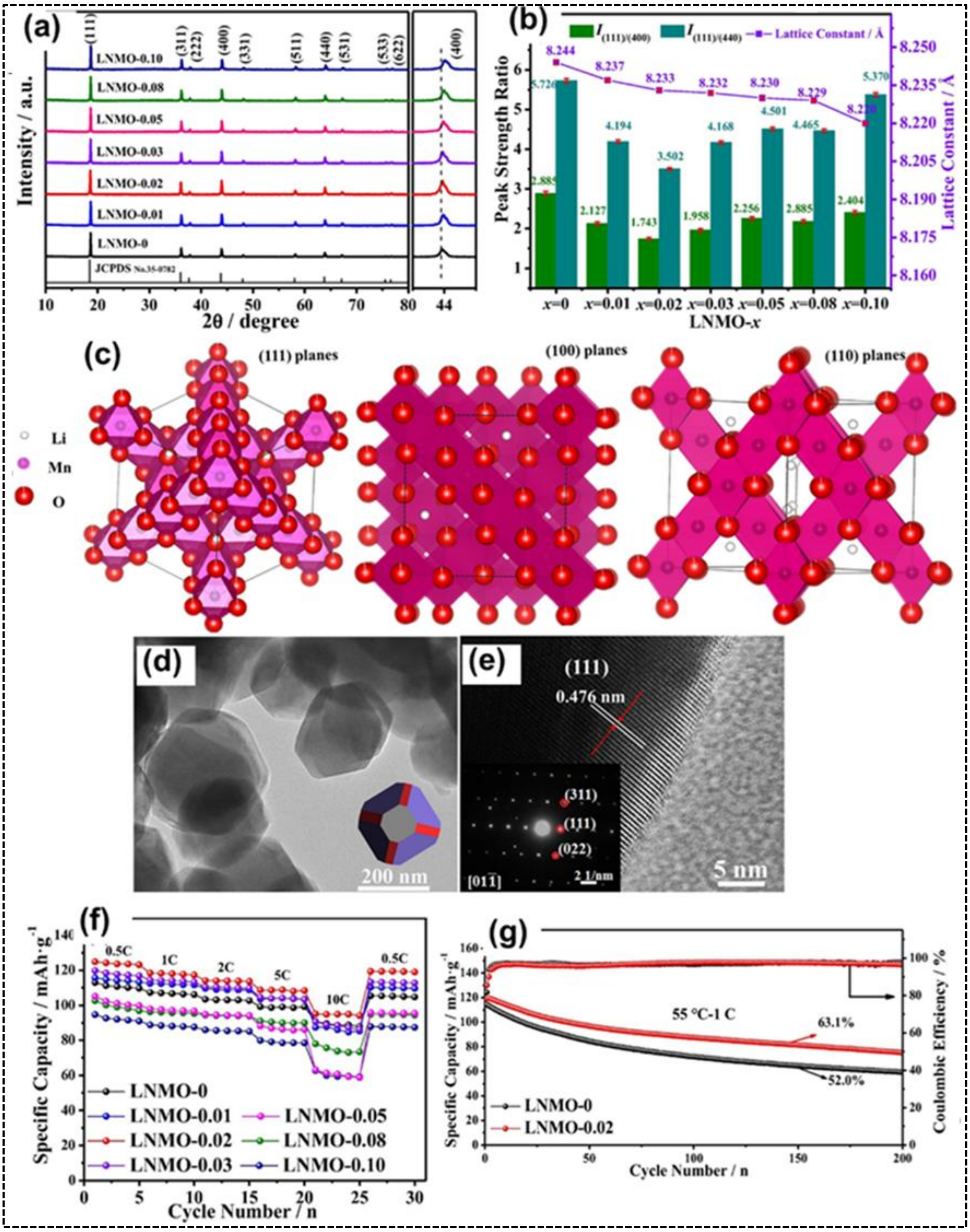

Figure 2.6. (a) XRD patterns of $Li_{1+x}Ni_{0.05}Mn_{1.95-x}O_4$ ($0 \leq x \leq 0.10$) showing a systematic shift of the (440) peak toward higher angles with increasing Li content, indicating lattice contraction. (b) Variation of intensity ratios I(111)/I(400) and I(111)/I(440) with Li content, reflecting changes in preferred crystal orientation. (c) Atomic models illustrating the (111), (100), and

(110) crystal facets. (d) TEM image of the LNMO-0.02 sample displaying a uniform truncated octahedral morphology. (e) HRTEM and SAED images showing lattice fringes (0.476 nm) corresponding to the (111) plane. Electrochemical performance of $Li_{1.02}Ni_{0.05}Mn_{1.93}O_4$: (f) Discharge capacities at various current rates. (g) cycling stability at 15 C. Reprinted with permission from Ref. [64], Copyright 2020, Elsevier Inc.

Li-Ni co-doping further modified the local crystal environment by compressing MnO_6 octahedra and expanding LiO_4 tetrahedra, reducing lattice strain and enabling efficient Li^+ diffusion. Ni^{2+} incorporation stabilized Mn^{4+} and suppressed Jahn-Teller distortion, enhancing the structural integrity of the spinel framework. These optimized structural and morphological features led to excellent electrochemical performance: the $Li_{1.02}Ni_{0.05}Mn_{1.93}O_4$ electrode delivered discharge capacities of 119.8, 107.1, and 97.9 $mAh\cdot g^{-1}$ at 1C, 5C, and 10C, respectively **(Figure 2.6(f))**, and retained 91.7% of its capacity after 1000 cycles at 15C **(Figure 2.6(g))**. Furthermore, the material demonstrated strong thermal stability, maintaining 118.5 $mAh\cdot g^{-1}$ at 55 °C and 1C, with 63.1% capacity retention after prolonged cycling [56].

Chu et al. synthesized a microscale (~10 µm) Ni-Co-Mn ternary composite oxide anode via a two-step process combining hydroxide co-precipitation and high-temperature annealing **(Figure 2.7(a))** [62]. The resulting material exhibited a uniform spherical morphology with a narrow particle size distribution **(Figure 2,7(b–d))** [65]. X-ray diffraction **(Figure 2.7(f))** confirmed the coexistence of dual crystalline phases: NiO (PDF#73-1519, space group Fm-3m) and $MnCo_2O_4$ (PDF#84-0482, space group Fd-3m). The NiO phase displayed a lattice spacing of 0.245 nm corresponding to the (111) plane, while $MnCo_2O_4$ exhibited 0.291 nm indexed to the (220) plane. The integration of rock-salt (NiO) and spinel ($MnCo_2O_4$) phases enhanced both structural stability and electrochemical functionality.

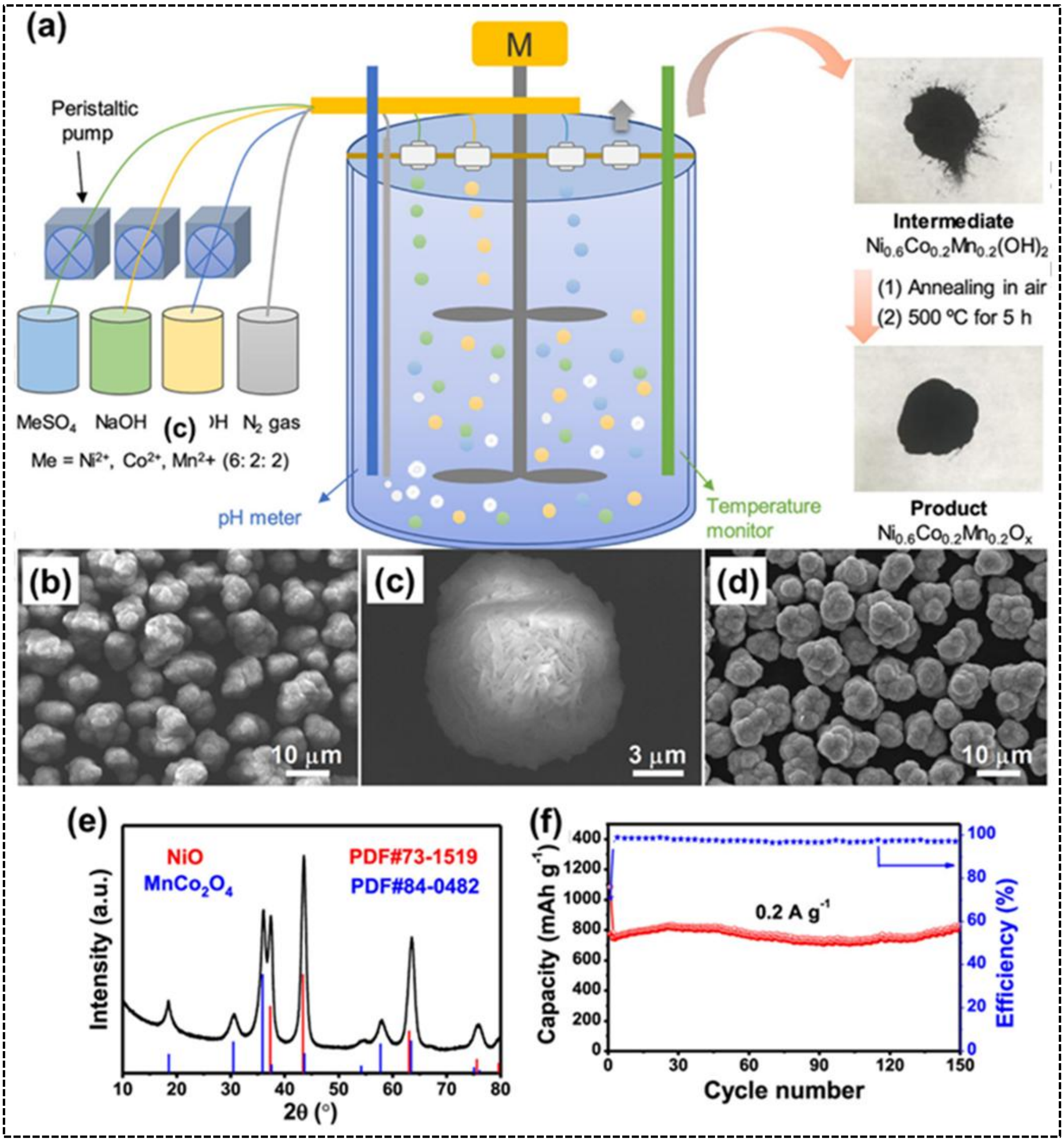

Figure 2.7: (a) Schematic illustration of the synthesis route combining hydroxide co-precipitation and high-temperature annealing. (b, c) SEM images of the $Ni_{0.6}Co_{0.2}Mn_{0.2}(OH)_2$ precursor showing uniform spherical morphology. (d) SEM image of $Ni_{0.6}Co_{0.2}Mn_{0.2}O_x$. (e) XRD patterns confirming the coexistence of NiO and $MnCo_2O_4$ phases. (f) Electrochemical cycling performance of the $Ni_{0.6}Co_{0.2}Mn_{0.2}O_x$ electrode. Reprinted with permission from Ref. [65], Copyright 2021, American Chemical Society.

By integrating the synergistic electrochemical properties of Ni, Co, and Mn oxides, the ternary composite electrode demonstrated excellent performance, including high specific capacity, superior rate capability, and long-term cycling stability. It achieved a specific capacity of 782 mAh g^{-1} at 0.2 A g^{-1} with minimal degradation over 150 cycles **(Figure 7(g))** [65]. Furthermore, the electrode retained 560 mAh g^{-1} after 500 cycles at 1.0 A g^{-1} and 504 mAh g^{-1} at 5.0 A g^{-1}, underscoring its outstanding rate performance. These results highlight the potential of Ni-Co-Mn-based phosphate composites as advanced electrode materials for hybrid supercapacitors, offering a viable route toward achieving higher energy and power densities in next-generation energy storage systems [62].

Soserov et al. explored $LiNi_{1/2}Mn_{1/2}PO_4$ and $NaNi_{1/2}Mn_{1/2}PO_4$ with olivine- and maricite-type structures, respectively. These phosphates exhibited uniform metal ion distribution and excellent chemical stability under alkaline conditions. In contrast, Ni-Mn oxides with ilmenite-type structures featured shared octahedral faces between Ni^{2+} and Mn^{4+} ions, enhancing redox activity. Morphological analyses revealed varying particle sizes and shapes, affecting ion transport and electrochemical kinetics. Electrochemical tests demonstrated that phosphate-based structures such as olivine retained their crystalline integrity and delivered superior cycling performance over 5000 cycles. These observations underscore the role of structural design phase type, morphology, and crystallographic orientation in determining long-term electrode performance [54].

2.5.5 Carbon Integration in Nickel-Manganese Phosphate Electrodes

Although nickel-manganese-based phosphate electrodes exhibit remarkable structural robustness and intrinsic redox activity, their practical electrochemical performance is often hindered by low intrinsic electrical conductivity and limited ion transport efficiency. To overcome these challenges, extensive research has focused on two primary enhancement strategies: (i) integration with conductive carbonaceous frameworks and (ii) incorporation of multiple metallic cations to form bimetallic phosphates [48,52,64–66]. In particular, combining bimetallic nickel-manganese phosphates (Ni-Mn phosphates) with conductive carbon scaffolds has proven highly effective. These hybrid materials synergistically merge the multi-redox functionality of Ni and Mn cations with the superior conductivity, mechanical stability, and high surface area of carbon frameworks, resulting in improved charge transport, faster ion diffusion, and enhanced electrochemical reversibility [85,86].

The incorporation of conductive carbon materials, such as graphene, carbon nanotubes (CNTs), and porous carbon foams, has proven highly effective in enhancing the overall electrochemical properties of transition metal phosphates. Graphene-based composites, in particular, provide large surface areas, excellent conductivity, and strong mechanical support for uniform dispersion of active materials [48,52,64–66].

Madito et al. demonstrated this advantage by incorporating $Mn_3P_2O_8$ into a graphene scaffold via a hydrothermal method [47]. Raman spectroscopy and electrochemical measurements revealed substantial improvements in charge transfer and conductivity, accompanied by bandgap narrowing and reduced interfacial resistance (**Figure 2.8(a,b)** [47]. Similarly, Mirghni et al. synthesized $NiCo(PO_4)_3$/graphene foam (GF) composites through a hydrothermal approach [87]. The resulting three-dimensional graphene framework provided uniform anchoring of $NiCo(PO_4)_3$ nanoplatelets without disrupting their flower-like morphology. Nitrogen adsorption-desorption isotherms confirmed a hierarchical porous structure, with micropores facilitating charge storage and mesopores promoting ion transport. The surface area increased from 2.9 $m^2\ g^{-1}$ for pristine $NiCo(PO_4)_3$ to 6.1 $m^2\ g^{-1}$ for $NiCo(PO_4)_3$/GF, enabling greater electrolyte accessibility and enhanced redox utilization. These improvements translated into superior specific capacitance and cycling stability, attributed to the synergistic redox contributions of Ni^{2+}/Ni^{3+} and Co^{2+}/Co^{3+} couples in combination with the high conductivity of the graphene network.

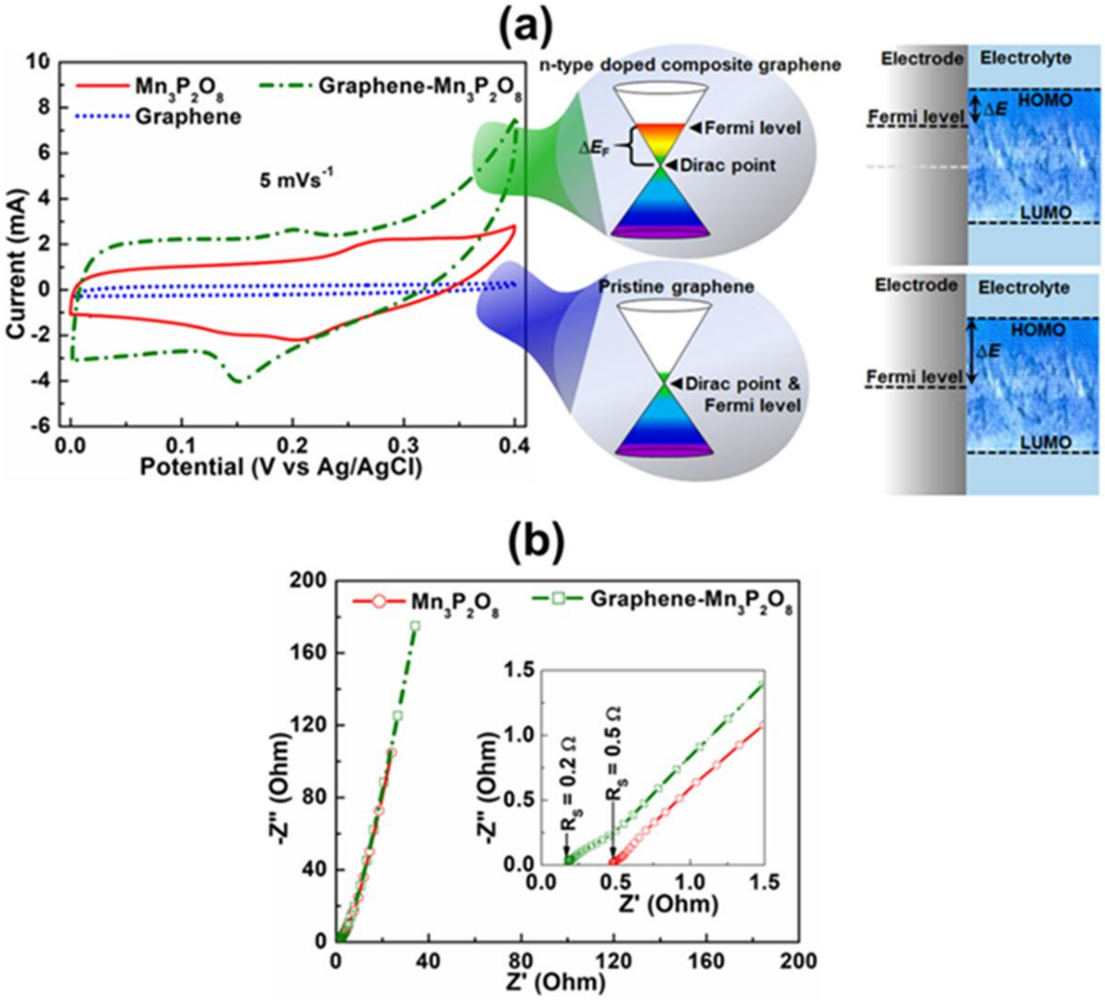

Figure 2.8. (a) Cyclic voltammetry (CV) curves of the electrodes, with a schematic illustration depicting the Fermi level shift in doped graphene and the corresponding reduction in the interfacial potential energy barrier (ΔE) for charge transfer between the electrode and electrolyte. (b) Nyquist plots showing the electrochemical impedance behavior of the electrodes. Reprinted with permission from Ref. [47], Copyright 2021, American Chemical Society.

Katkar et al. developed ternary Ni-Co-Mn phosphate nanoparticles anchored on MXene nanosheets **(Figure 2.9(a))**, achieving a high specific capacity of 342 mAh g^{-1} with nearly full retention after 5000 cycles [71]. A solid-state hybrid device, assembled using these materials as the positive electrode and reduced graphene oxide (rGO) as the negative electrode, delivered an energy density of 22 Wh kg^{-1} and maintained 95.4% of its capacity after 5000 cycles **(Figures 2.9(b,c))** [71]. In a related study, binder-free mesoporous Ni-Mn phosphate microarchitectures synthesized on nickel foam exhibited a specific capacity of 545 C g^{-1} with complete retention after 6000 cycles. A flexible solid-state device fabricated from these materials achieved an energy density of 48.2 Wh kg^{-1} with stable performance over 5000 cycles [71]. While carbon integration markedly improves electrical conductivity, ion diffusion, and mechanical resilience, it does not fully resolve the issue of limited intrinsic redox capacity. Therefore, compositional tuning through bimetallic phosphate systems has been adopted as a complementary approach to further enhance electrochemical activity.

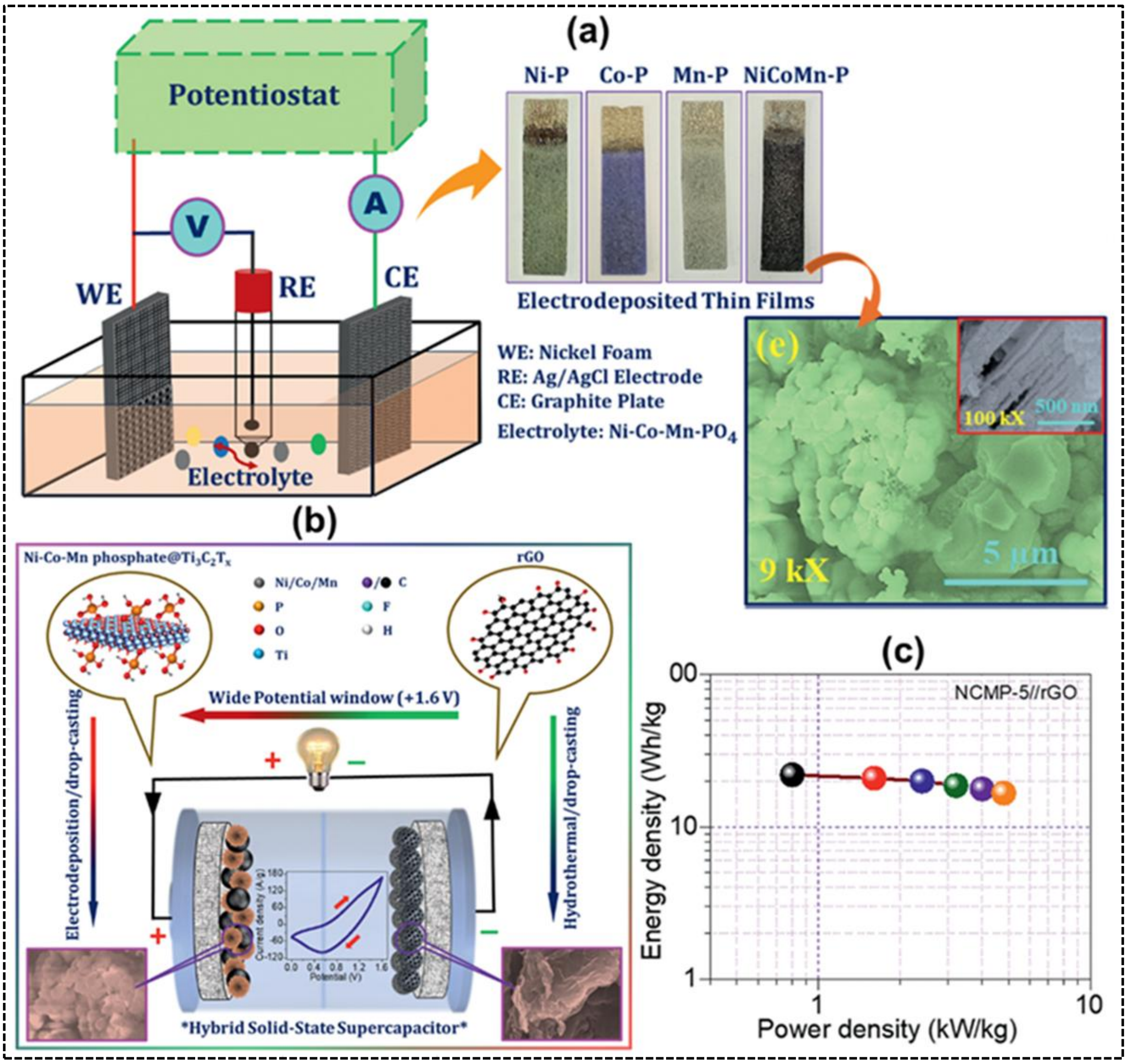

Figure 2.9. Schematic illustration of the electrodeposition process for Ni-Co-Mn phosphate growth on nickel foam (NF). (b) Schematic representation of the NCMP-5//rGO hybrid solid-state supercapacitor device, and (c) corresponding Ragone plot showing energy and power performance. Reprinted with permission from Ref. [71], Copyright 2025, Elsevier.

2.5.6 Synergistic Effects in Nickel-Manganese Phosphate Composite Electrodes

Introducing two or more metal cations into the phosphate framework creates synergistic effects that enhance electronic conductivity, structural robustness, and redox kinetics. Li et al. employed density functional theory (DFT) to compare nickel phosphate octahydrate with nickel-manganese phosphate octahydrate, revealing that manganese incorporation reduced the band gap from 1.9 eV to 1.2 eV thereby improving electronic conductivity and redox efficiency [99]. Similar findings have been reported for related transition metal phosphates such as $Co_3(PO_4)_2$, $Ni_2P_2O_7$, and $Mn_3(PO_4)_2$, where Ni-based phases exhibit high capacitance and Mn-based compounds demonstrate outstanding long-term stability [88–90].

Recent work has advanced these concepts through heterostructural and multicomponent designs. Li et al [99] fabricated $Ni_2Mn(PO_4)_2 \cdot 8H_2O$ heterostructures containing both crystalline and amorphous domains. This design enhanced charge transport pathways and mechanical stability, resulting in excellent cycling reversibility over 15,000 cycles **(Figure 2.10)**. The corresponding device achieved an energy density of 66.2 $Wh \cdot kg^{-1}$, demonstrating the effectiveness of heterostructure engineering. Nivetha et al. [70] reported manganese-doped nickel pyrophosphate prepared via chemical bath deposition, achieving a capacitance of 603 $F \cdot g^{-1}$ and 97% retention after 4000 cycles, attributed to the additional Mn redox-active sites and enhanced ion accessibility.

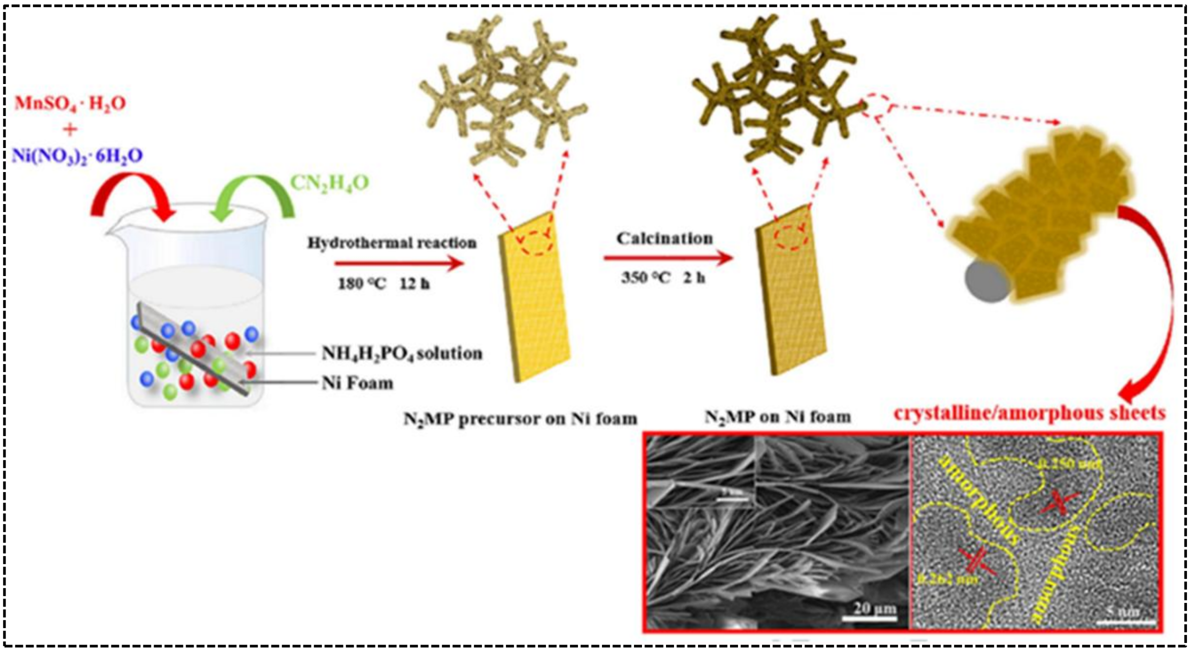

Figure 2.10. Schematic illustration of N_2MP synthesis with corresponding SEM and HRTEM images showing morphological and structural features. Reprinted with permission from Ref. [63], Copyright 2024, Elsevier.

In more complex architectures, Dong et al. [91] developed CNT@NCO@MCP hybrid electrodes, combining MnCoP nanosheets with $NiCo_2O_4$ nanograss on CNT-coated substrates. The hierarchical configuration offered excellent reversibility, high capacitance, and exceptional stability, retaining performance over 20,000 cycles. Similarly, Katkar et al. [71] synthesized ternary Ni-Co-Mn phosphate nanoparticles anchored on MXene nanosheets, achieving a specific capacity of 342 $mAh \cdot g^{-1}$ with nearly full retention after 5000 cycles. A solid-state device fabricated using this composite as the positive electrode and reduced graphene oxide (rGO) as the negative electrode delivered an energy density of 22 $Wh \cdot kg^{-1}$ with 95.4% retention after 5000 cycles. Further, binder-free mesoporous Ni-Mn phosphate microarchitectures grown directly on nickel foam have been reported to deliver a specific capacity of 545 $C \cdot g^{-1}$ and 100% retention after 6000 cycles [92]. A flexible solid-state device assembled from these electrodes provided an energy density of 48.2 $Wh \cdot kg^{-1}$, maintaining stable performance over 5000 cycles.

Monometallic transition metal phosphates often suffer from narrow potential windows, sluggish charge transfer, and structural degradation during cycling [93]. These drawbacks are effectively mitigated by developing binary or multi-metallic phosphate composites, where synergistic cation interactions enhance electrochemical performance. In Ni-Mn systems, this synergy improves structural integrity, electronic conductivity, ion diffusion, and redox activity, providing multiple accessible oxidation states and a higher density of electroactive sites for superior charge storage [94]. The simultaneous participation of Ni and Mn ions broadens the potential window, increases electroactive surface area, and delivers better pseudocapacitive performance than single-metal systems [95].

Studies summarized in **Tables 2.3 and 2.4** confirm that combining bimetallic phosphates with conductive carbon scaffolds further enhances redox kinetics, conductivity, and cycling stability. Aqueous KOH electrolytes (up to 6 M) remain widely used for Ni-Mn phosphate electrodes due to high ionic conductivity and favorable OH^- - coupled redox reactions, although the operating voltage is limited to ~1.2 V. PVA-KOH gels offer a flexible, leak-free solid-state alternative with slightly lower conductivity. Recent Ni-Mn phosphate heterostructures show that careful electrode-electrolyte optimization sustains strong areal capacitance and long-term durability, advancing the development of high-performance flexible hybrid supercapacitors [85,86].

Table 2.3. Recent reports on the electrochemical performance of nickel-manganese phosphate electrode materials.

Electrode materials	**Morphology**	**Electrolyte**	**Potential window**	**Specific capacity**	**Cycles (Stability)**	**Ref.**
$NiMn(PO_4)_2$ @VGNHs-CC	nanosphere-like	1 M KOH	0.0 - 0.8 V/Hg/HgO	1068 C/g at 3.0 A/g	5000 (97%) at 20mV/s	[96]
$NiMn(PO_4)_2$ @PANI/MWCNTs	flake-like	1 M KOH	0.0 - 0.7 V/Hg/HgO	912.2 C/g at 1 A/g	-	[97]
$NiMn(PO_4)_2$/GF	cubic rods	1 M KOH	0.0 to 0.45 V/Ag/AgCl	349.2 C/g at 0.5 A/g	-	[98]
$Ni_2Mn(PO_4)_2{\cdot}8H_2O$	Crystalline /amorphous	3 M KOH	0.0 - 0.6 V/Hg/HgO	2351.6 F/g at 1 A/g	3000 (67.3%) at 10A/g	[63]
Mn-$Ni_2P_2O_7$	Microspheres /sheets	2 M KOH	-0.4 to 0.2 V/Hg/HgO	603 F/g at 1 A/g	4000 (97.02%) at 10A/g	[70]
CNT@ $NiCo_2O_4$@MnCoP	nanosheets	2 M KOH	0.0 - 0.55 V/Hg/HgO	4787.3 mF/cm^2 at 1 mA/cm^2	5000 (80%)	[91]
Ni-Co-Mn phosphate	Irregularly shaped nanoparticles	1 M KOH	0.0 - 0.55 V/Hg/HgO	935 C/g at 5.0 A/g	-	[71]
Ni-Co-Mn phosphate @MXene nanocomposite	Nanoparticles /nanosheets	1 M KOH	0.0 - 0.55 V/Hg/HgO	1230 C/g at 5.0 A/g	5000 (98.8%) at 8.0 A/g	[71]
$NiMn(PO_4)_2$	microplate-like	1 M KOH	0.0 to 0.8 V/Hg/HgO	545 C/g at 3.0 A/g	6000 (127%) at 20 mV/s	[92]

Table 2.4. Recent advances in nickel-manganese phosphate-based hybrid supercapacitor devices

Positive electrode	Negative electrode	Electrolyte	Potential window (V)	Specific capacity/ capacitance	Energy density (Wh/kg)	Power density (kW/kg)	Cycles (Stability)	Ref.
$NiMn(PO_4)_2$@ VGNHs-CC	$NiMn(PO_4)_2$@ VGNHs-CC	PVA-KOH solid gel	0.0 - 1.5	512 C/g at 1 A/g	106.8	0.751	5000 (94%) at 2.5A/g	[96]
$NiMn(PO_4)_2$ @PANI/MWCNTs	AC	1 M KOH	0.0 - 1.6	139.3 C/g at 1 A/g	58	0.918	5000 (105.3%) at 2A/g	[97]
$NiMn(PO_4)_2$/GF	pepper seed (pp)AC	1 M KOH	0.0 - 1.5	128.7 C/g at 0.5 A/g	35.42	0.538	10000 (97.8%) at 6A/g	[98]
$Ni_2Mn(PO_4)_2 \cdot 8H_2O$	AC	3 M KOH	0.0 - 1.6	163.1 F/g at 1 A/g	66.22	0.40	15000 (81.03%) at 60 mA/cm^2	[63]
CNT@ $NiCo_2O_4$@MnCoP	AC	3 M KOH	0.0 - 1.65	1030.90 mF/cm^2 at 1 mA/cm^2	0.390 mWh/cm^2	0.825 mW/cm^2	20000 (85.7%) at 10 mA/cm^2	[91]
Ni-Co-Mn phosphate @MXene nanocomposite	rGO	PVA-KOH solid gel	0.0 - 1.6	99 C/g at 1 A/g	22	0.80	10000 (95.4%) at 3.0A/g	[71]
$NiMn(PO_4)_2$	rGO	PVA-KOH solid gel	0.0 - 1.8	192 C/g at 0.6 A/g	48.2	0.575	5000 (108%)	[92]

Overall, the integration of carbonaceous frameworks such as graphene scaffolds, CNT networks, and porous foams substantially enhances the conductivity, ion transport, and mechanical durability of phosphate-based electrodes. When combined with the synergistic electrochemical interactions of bimetallic systems, these hybrid designs yield materials with high energy and power densities as well as excellent cycling stability. Notably, Ni-Mn phosphate/carbon composites have achieved specific capacitances exceeding 1100 F g^{-1} at moderate current densities, demonstrating strong potential for practical energy storage applications. Moving forward, bridging the gap between laboratory-scale synthesis and scalable production remains a crucial step toward realizing the commercial potential of these advanced hybrid electrode systems.

2.6 Current Research Gaps in Nickel-Manganese Phosphate-Based Electrodes

The continued advancement and eventual commercialization of nickel-manganese phosphate-based hybrid supercapacitors depend on addressing several key challenges and research opportunities. Enhancing electrical conductivity remains a primary focus, as phosphate frameworks are inherently poor conductors. Compositing Ni-Mn phosphates with highly conductive carbon materials such as graphene, MXenes, or carbon nanotubes can significantly improve charge transport, mechanical integrity, and cycling durability. Equally important is advanced morphology engineering developing nanosheets, nanorods, and three-dimensional (3D) hierarchical structures to facilitate ion and electron diffusion while maximizing active surface area. Beyond morphological design, exploring bimetallic and ternary phosphate systems such as Ni-Mn-Co or Ni-Mn-Fe can yield synergistic effects that enhance redox activity and conductivity. To better understand the underlying electrochemical mechanisms, in-situ and operando characterization techniques including Raman spectroscopy, X-ray diffraction, and X-ray photoelectron spectroscopy should be employed to monitor real-time structural evolution and electrode-electrolyte interactions. Moreover, the development of innovative electrolytes, including ionic liquids, deep eutectic solvents, and redox-active systems, offers a means to expand the potential window and improve energy density, provided compatibility with Ni-Mn phosphate electrodes is maintained. Standardized performance evaluation protocols are also crucial to ensure realistic benchmarking, as laboratory results often overestimate practical device performance. Transitioning toward scalable and sustainable synthesis routes, such as microwave-assisted, aqueous-phase, and additive manufacturing techniques, will further enhance industrial feasibility while reducing environmental impact. Finally, the integration of Ni-Mn phosphate/carbon composites into flexible and wearable devices represents an emerging frontier, enabling applications in soft robotics, portable electronics, and biomedical energy systems. Collectively, these research directions will be instrumental in translating nickel-manganese phosphate nanocomposites from laboratory-scale materials into high-performance, commercially viable hybrid supercapacitors.

2.7 Conclusion

This chapter reviewed the scientific progress and research trends surrounding nickel-manganese phosphate ($NiMn(PO_4)_2$) and carbon-based nanocomposites for hybrid supercapacitors. The literature emphasizes that the electrochemical behavior of supercapacitors is governed by charge storage mechanisms, electrode-electrolyte interactions, and material structure. Ni-Mn phosphates have emerged as promising pseudocapacitive materials due to their multiple redox states, robust phosphate frameworks, and compositional tunability. However, their low intrinsic conductivity and limited ion transport present key challenges.

Various synthesis strategies including hydrothermal, solvothermal, chemical precipitation, and microwave-assisted methods enable controlled morphology and crystallinity, which are vital for optimizing electrochemical performance. Structural engineering through doping and phase control further improves conductivity and cycling stability. Integrating Ni-Mn phosphates with conductive carbons such as graphene, CNTs, or MXenes significantly enhances charge transfer, ion diffusion, and mechanical integrity, while bimetallic and ternary systems (e.g., Ni-Mn-Co) exploit synergistic redox effects for improved capacitance and rate performance.

Electrolyte selection remains a critical determinant of energy and power density. Aqueous systems, particularly KOH, offer high ionic conductivity and compatibility with faradaic reactions, whereas neutral and non-aqueous electrolytes extend voltage stability and durability. Reported Ni-Mn phosphate/carbon composites demonstrate specific capacities exceeding 1000 C g^{-1}, energy densities above 100 Wh kg^{-1}, and long-term stability beyond 5000 cycles, underscoring their potential for high-performance hybrid supercapacitors.

Despite these advancements, challenges persist in achieving scalable, cost-effective synthesis, optimizing electrode-electrolyte compatibility, and ensuring long-term durability. Future research should focus on green fabrication routes, mechanistic understanding through in-situ studies, electrolyte innovation, and integration into flexible and wearable energy storage systems.

References

[1] S. Rudra, H.W. Seo, S. Sarker, D.M. Kim, Supercapatteries as Hybrid Electrochemical Energy Storage Devices: Current Status and Future Prospects, Molecules 29 (2024) 243. https://doi.org/10.3390/molecules29010243.

[2] D. Majumdar, Recent progress in copper sulfide-based nanomaterials for high energy supercapacitor applications, Journal of Electroanalytical Chemistry 880 (2021). https://doi.org/10.1016/j.jelechem.2020.114825.

[3] M.R. Lukatskaya, B. Dunn, Y. Gogotsi, Multidimensional materials and device architectures for future hybrid energy storage, Nat Commun 7 (2016). https://doi.org/10.1038/ncomms12647.

[4] N.R. Chodankar, H.D. Pham, A.K. Nanjundan, J.F.S. Fernando, K. Jayaramulu, D. Golberg, Y.K. Han, D.P. Dubal, True Meaning of Pseudocapacitors and Their Performance Metrics: Asymmetric versus Hybrid Supercapacitors, Small 16 (2020). https://doi.org/10.1002/smll.202002806.

[5] M. Sarno, Nanotechnology in energy storage: The supercapacitors, Stud Surf Sci Catal 179 (2019) 431–458. https://doi.org/10.1016/B978-0-444-64337-7.00022-7.

[6] H. Wang, M. Liang, D. Duan, W. Shi, Y. Song, Z. Sun, Rose-like Ni3S4 as battery-type electrode for hybrid supercapacitor with excellent charge storage performance, Chemical Engineering Journal 350 (2018) 523–533. https://doi.org/10.1016/j.cej.2018.05.004.

[7] B. Zhao, D. Chen, X. Xiong, B. Song, R. Hu, Q. Zhang, B.H. Rainwater, G.H. Waller, D. Zhen, Y. Ding, Y. Chen, C. Qu, D. Dang, C.P. Wong, M. Liu, A high-energy, long

cycle-life hybrid supercapacitor based on graphene composite electrodes, Energy Storage Mater 7 (2017) 32–39. https://doi.org/10.1016/j.ensm.2016.11.010.

[8] N. Devi, S.S. Ray, Performance of bismuth-based materials for supercapacitor applications: A review, Mater Today Commun 25 (2020). https://doi.org/10.1016/j.mtcomm.2020.101691.

[9] P. Simon, Y. Gogotsi, Materials for electrochemical capacitors, Nat Mater 7 (2008) 845–854.

[10] V. Augustyn, P. Simon, B. Dunn, Pseudocapacitive oxide materials for high-rate electrochemical energy storage, Energy Environ Sci 7 (2014). https://doi.org/10.1039/c3ee44164d.

[11] L. Cao, J. Zhu, Y. Li, P. Xiao, Y. Zhang, S. Zhang, S. Yang, Ultrathin single-crystalline vanadium pentoxide nanoribbon constructed 3D networks for superior energy storage, J Mater Chem A Mater 2 (2014). https://doi.org/10.1039/c4ta02229g.

[12] C. Choi, J.H. Kim, H.J. Sim, J. Di, R.H. Baughman, S.J. Kim, Supercapacitors: Microscopically Buckled and Macroscopically Coiled Fibers for Ultra-Stretchable Supercapacitors (Adv. Energy Mater. 6/2017), Adv Energy Mater 7 (2017). https://doi.org/10.1002/aenm.201770029.

[13] C. Choi, J.H. Kim, H.J. Sim, J. Di, R.H. Baughman, S.J. Kim, Microscopically Buckled and Macroscopically Coiled Fibers for Ultra-Stretchable Supercapacitors, Adv Energy Mater 7 (2017). https://doi.org/10.1002/aenm.201602021.

[14] V. Augustyn, P. Simon, B. Dunn, Pseudocapacitive oxide materials for high-rate electrochemical energy storage, Energy Environ Sci 7 (2014) 1597–1614. https://doi.org/10.1039/c3ee44164d.

[15] Y. Liu, S.P. Jiang, Z. Shao, Intercalation pseudocapacitance in electrochemical energy storage: recent advances in fundamental understanding and materials development, Mater Today Adv 7 (2020). https://doi.org/10.1016/j.mtadv.2020.100072.

[16] Z. Yang, J. Tian, Z. Yin, C. Cui, W. Qian, F. Wei, Carbon nanotube- and graphene-based nanomaterials and applications in high-voltage supercapacitor: A review, Carbon N Y 141 (2019) 467–480. https://doi.org/10.1016/j.carbon.2018.10.010.

[17] V. Aravindan, M. V. Reddy, S. Madhavi, S.G. Mhaisalkar, G. V. Subba Rao, B.V.R. Chowdari, Hybrid supercapacitor with nano-TiP2O7 as intercalation electrode, J Power Sources 196 (2011) 8850–8854. https://doi.org/10.1016/j.jpowsour.2011.05.074.

[18] S. Uppugalla, U. Male, P. Srinivasan, Design and synthesis of heteroatoms doped carbon/polyaniline hybrid material for high performance electrode in supercapacitor application, Electrochim Acta 146 (2014) 242–248. https://doi.org/10.1016/j.electacta.2014.09.047.

[19] I. Hadjipaschalis, A. Poullikkas, V. Efthimiou, Overview of current and future energy storage technologies for electric power applications, Renewable and Sustainable Energy Reviews 13 (2009) 1513–1522. https://doi.org/10.1016/j.rser.2008.09.028.

[20] K. Naoi, Evolution of energy storage on the platform of supercapacitors, Electrochemistry 81 (2013). https://doi.org/10.5796/electrochemistry.81.775.

[21] K. Naoi, S. Ishimoto, J.I. Miyamoto, W. Naoi, Second generation “nanohybrid supercapacitor”: Evolution of capacitive energy storage devices, Energy Environ Sci 5 (2012). https://doi.org/10.1039/c2ee21675b.

[22] T. Brousse, D. Bélanger, J.W. Long, To Be or Not To Be Pseudocapacitive?, J Electrochem Soc 162 (2015). https://doi.org/10.1149/2.0201505jes.

[23] L. Feng, H. Xue, Advances in transition-metal phosphide applications in electrochemical energy storage and catalysis, ChemElectroChem 4 (2017) 20–34. https://doi.org/10.1002/celc.201600563.

[24] M.R. Lukatskaya, B. Dunn, Y. Gogotsi, Multidimensional materials and device architectures for future hybrid energy storage, Nat Commun 7 (2016) 12647. https://doi.org/10.1038/ncomms12647.

[25] S. Zhang, N. Pan, Supercapacitors Performance Evaluation, Adv Energy Mater 5 (2015) 1401401. https://doi.org/10.1002/AENM.201401401.

[26] M. Toupin, T. Brousse, D. Bélanger, Charge storage mechanism of MnO2 electrode used in aqueous electrochemical capacitor, Chemistry of Materials 16 (2004) 3184–3190. https://doi.org/10.1021/CM049649J/SUPPL_FILE/CM049649JSI20040602_020207.PDF.

[27] T. Liu, W.G. Pell, B.E. Conway, Self-discharge and potential recovery phenomena at thermally and electrochemically prepared RuO2 supercapacitor electrodes, Electrochim Acta 42 (1997). https://doi.org/10.1016/S0013-4686(97)81190-5.

[28] A. Burke, M. Miller, Testing of electrochemical capacitors: Capacitance, resistance, energy density, and power capability, Electrochim Acta 55 (2010) 7538–7548. https://doi.org/10.1016/J.ELECTACTA.2010.04.074.

[29] Y. Gogotsi, R.M. Penner, Energy Storage in Nanomaterials – Capacitive, Pseudocapacitive, or Battery-like?, ACS Nano 12 (2018) 2081–2083. https://doi.org/10.1021/acsnano.8b01914.

[30] K.O. Oyedotun, M.J. Madito, A. Bello, D.Y. Momodu, A.A. Mirghni, N. Manyala, Investigation of graphene oxide nanogel and carbon nanorods as electrode for electrochemical supercapacitor, Electrochim Acta (2017). https://doi.org/10.1016/j.electacta.2017.05.150.

[31] B. Akinwolemiwa, C. Peng, G.Z. Chen, Redox electrolytes in supercapacitors, J Electrochem Soc 162 (2015) A5054–A5059. https://doi.org/10.1149/2.0111505jes.

[32] G. Godillot, L. Guerlou-Demourgues, P.-L. Taberna, P. Simon, C. Delmas, Original Conductive Nano-Co3O4 Investigated as Electrode Material for Hybrid Supercapacitors, Electrochemical and Solid-State Letters 14 (2011) A139. https://doi.org/10.1149/1.3609259.

[33] P. Simon, Y. Gogotsi, Materials for electrochemical capacitors, 7 (2008) 845–854. https://doi.org/10.1038/nmat2297.

[34] A. Laheäär, P. Przygocki, Q. Abbas, F. Béguin, Appropriate methods for evaluating the efficiency and capacitive behavior of different types of supercapacitors, 2015. https://doi.org/10.1016/j.elecom.2015.07.022.

[35] A. Laheaar, P. Przygocki, Q. Abbas, F. B??guin, A. Laheäär, P. Przygocki, Q. Abbas, F. Béguin, Appropriate methods for evaluating the efficiency and capacitive behavior of different types of supercapacitors, Electrochem Commun 60 (2015) 21–25. https://doi.org/10.1016/j.elecom.2015.07.022.

[36] C. Du, N. Pan, Supercapacitors using carbon nanotubes films by electrophoretic deposition, J Power Sources 160 (2006) 1487–1494. https://doi.org/10.1016/J.JPOWSOUR.2006.02.092.

[37] J.R. Miller, R.A. Outlaw, B.C. Holloway, Graphene double-layer capacitor with ac line-filtering performance, Science (1979) 329 (2010) 1637–1639. https://doi.org/10.1126/SCIENCE.1194372.

[38] P.L. Taberna, P. Simon, J.-F.F. Fauvarque, Electrochemical Characteristics and Impedance Spectroscopy Studies of Carbon-Carbon Supercapacitors, J Electrochem Soc 150 (2003) A292-300. https://doi.org/10.1149/1.1543948.

[39] M.F. Dupont, A.F. Hollenkamp, S.W. Donne, Large Amplitude Electrochemical Impedance Spectroscopy for Characterizing the Performance of Electrochemical Capacitors, J Electrochem Soc 161 (2014) A648–A656. https://doi.org/10.1149/2.098404JES/XML.

[40] A. Burke, M. Miller, The power capability of ultracapacitors and lithium batteries for electric and hybrid vehicle applications, J Power Sources 196 (2011) 514–522. https://doi.org/10.1016/J.JPOWSOUR.2010.06.092.

[41] M.Z. Iqbal, S. Zakar, S.S. Haider, Role of aqueous electrolytes on the performance of electrochemical energy storage device, Journal of Electroanalytical Chemistry 858 (2020). https://doi.org/10.1016/j.jelechem.2019.113793.

[42] N.L. Wulan Septiani, Y.V. Kaneti, K.B. Fathoni, J. Wang, Y. Ide, B. Yuliarto, Nugraha, H.K. Dipojono, A.K. Nanjundan, D. Golberg, Y. Bando, Y. Yamauchi, Self-assembly of nickel phosphate-based nanotubes into two-dimensional crumpled sheet-like architectures for high-performance asymmetric supercapacitors, Nano Energy 67 (2020) 104270. https://doi.org/10.1016/j.nanoen.2019.104270.

[43] Raissa, N.L.W. Septiani, S. Wustoni, F. Failamani, M. Iqbal, Nugraha, V. Suendo, B. Yuliarto, Improving capacity of nickel phosphate Versailles Santa Barbara-5 with calcination for high-performance asymmetric supercapacitors, J Energy Storage 56 (2022) 106109. https://doi.org/10.1016/j.est.2022.106109.

[44] F.S. Omar, A. Numan, N. Duraisamy, S. Bashir, K. Ramesh, S. Ramesh, Ultrahigh capacitance of amorphous nickel phosphate for asymmetric supercapacitor applications, RSC Adv 6 (2016) 76298–76306. https://doi.org/10.1039/C6RA15111F.

[45] Y.-H. Dai, L.-B. Kong, K. Yan, M. Shi, Y.-C. Luo, L. Kang, Facile fabrication of manganese phosphate nanosheets for supercapacitor applications, Ionics (Kiel) 22 (2016) 1461–1469. https://doi.org/10.1007/s11581-016-1652-y.

[46] S.J. Marje, P.R. Deshmukh, J.L. Gunjakar, C.D. Lokhande, U.M. Patil, Strategically Tuned Ultrathin Nickel Phosphate Nanosheet Thin-Film Electrode as Cathode for High-Power Hybrid Supercapacitor Device, Energy and Fuels 35 (2021) 14110–14121. https://doi.org/10.1021/acs.energyfuels.1c01641.

[47] M.J. Madito, Correlation of the Graphene Fermi-Level Shift and the Enhanced Electrochemical Performance of Graphene-Manganese Phosphate for Hybrid Supercapacitors: Raman Spectroscopy Analysis, ACS Appl Mater Interfaces 13 (2021) 37014–37026. https://doi.org/10.1021/acsami.1c07104.

[48] A.A. Mirghni, M.J. Madito, T.M. Masikhwa, K.O. Oyedotun, A. Bello, N. Manyala, Hydrothermal synthesis of manganese phosphate/graphene foam composite for electrochemical supercapacitor applications, J Colloid Interface Sci 494 (2017) 325–337. https://doi.org/10.1016/J.JCIS.2017.01.098.

[49] X.-J. Ma, W.-B. Zhang, L.-B. Kong, Y.-C. Luo, L. Kang, Electrochemical performance in alkaline and neutral electrolytes of a manganese phosphate material

possessing a broad potential window, RSC Adv. 6 (2016) 40077–40085. https://doi.org/10.1039/C6RA02217K.

[50] M. Minakshi, D. Mitchell, R. Jones, F. Alenazey, T. Watcharatharapong, S. Chakraborty, R. Ahuja, Synthesis, structural and electrochemical properties of sodium nickel phosphate for energy storage devices, Nanoscale 8 (2016) 11291–11305. https://doi.org/10.1039/C6NR01179A.

[51] H. Pang, Z. Yan, Y. Wei, X. Li, J. Li, L. Zhang, J. Chen, The Morphology Evolution of Nickel Phosphite Hexagonal Polyhedrons and Their Primary Electrochemical Capacitor Applications, (2013) 287–295. https://doi.org/10.1002/ppsc.201200147.

[52] A.A. Mirghni, M.J. Madito, K.O. Oyedotun, T.M. Masikhwa, N.M. Ndiaye, S.J. Ray, N. Manyala, A high energy density asymmetric supercapacitor utilizing a nickel phosphate/graphene foam composite as the cathode and carbonized iron cations adsorbed onto polyaniline as the anode, RSC Adv 8 (2018) 11608–11621. https://doi.org/10.1039/c7ra12028a.

[53] A. Samal, C. Mohanty, N. Das, R. Das, M.F. Kühnel, A review on metal phosphate based graphene hybrids: Emerging composite materials for vast applications, Mater Today Chem 38 (2024) 102096. https://doi.org/10.1016/j.mtchem.2024.102096.

[54] L. Soserov, D. Marinova, V. Koleva, A. Stoyanova, R. Stoyanova, Comparison of the Properties of Ni–Mn Hydroxides/Oxides with Ni–Mn Phosphates for the Purpose of Hybrid Supercapacitors, Batteries 8 (2022) 51. https://doi.org/10.3390/batteries8060051.

[55] H. Zhao, Z. Yuan, Design strategies of transition-metal phosphate and phosphonate electrocatalysts for energy-related reactions, ChemSusChem 14 (2021) 130–149. https://doi.org/10.1002/cssc.202002103.

[56] H. Liu, M. Li, M. Xiang, J. Guo, H. Bai, W. Bai, X. Liu, Effects of crystal structure and plane orientation on lithium and nickel co-doped spinel lithium manganese oxide for long cycle life lithium-ion batteries, J Colloid Interface Sci 585 (2021) 729–739. https://doi.org/10.1016/j.jcis.2020.10.052.

[57] A. Samal, C. Mohanty, N. Das, R. Das, M.F. Kühnel, A review on metal phosphate based graphene hybrids: Emerging composite materials for vast applications, Mater Today Chem 38 (2024) 102096. https://doi.org/10.1016/j.mtchem.2024.102096.

[58] X. Li, A.M. Elshahawy, C. Guan, J. Wang, Metal phosphides and phosphates-based electrodes for electrochemical supercapacitors, Small 13 (2017). https://doi.org/10.1002/smll.201701530.

[59] A.A. Mirghni, K.O. Oyedotun, O. Fasakin, B.A. Mahmoud, D.J. Tarimo, N. Manyala, High-performance bimetallic Ni-Mn phosphate hybridized with 3-D graphene foam for novel hybrid supercapacitors, J Energy Storage 31 (2020) 101584. https://doi.org/10.1016/j.est.2020.101584.

[60] N. Chen, J. Zhou, Q. Kang, H. Ji, G. Zhu, Y. Zhang, S. Chen, J. Chen, X. Feng, W. Hou, Amorphous vanadyl phosphate/graphene composites for high performance supercapacitor electrode, J Power Sources 344 (2017) 185–194. https://doi.org/10.1016/j.jpowsour.2017.01.119.

[61] A.A. Mirghni, K.O. Oyedotun, O. Fasakin, B.A. Mahmoud, D.J. Tarimo, N. Manyala, High-performance bimetallic Ni-Mn phosphate hybridized with 3-D graphene foam for novel hybrid supercapacitors, J Energy Storage 31 (2020) 101584. https://doi.org/10.1016/j.est.2020.101584.

[62] C. Chu, L. Chang, D. Yin, D. Zhang, Y. Cheng, L. Wang, Large-Sized Nickel–Cobalt–Manganese Composite Oxide Agglomerate Anode Material for Long-Life-Span

Lithium-Ion Batteries, ACS Appl Energy Mater 4 (2021) 13811–13818. https://doi.org/10.1021/acsaem.1c02565.

[63] M. Li, M. Zhao, B. Wu, S. Mourdikoudis, S. Wei, F.M. Oliveira, J. He, L. Děkanovský, J. Luxa, S. Yang, Z. Sofer, Rational design of crystalline/amorphous nickel manganese phosphate octahydrate heterostructure for high-performance aqueous and all-solid-state asymmetric supercapacitors, Chemical Engineering Journal 482 (2024). https://doi.org/10.1016/j.cej.2024.148895.

[64] C. Xiang, M. Li, M. Zhi, A. Manivannan, N. Wu, A reduced graphene oxide/Co3O4 composite for supercapacitor electrode, J Power Sources 226 (2013) 65–70. https://doi.org/10.1016/j.jpowsour.2012.10.064.

[65] N.M. Ndiaye, B.D. Ngom, N.F. Sylla, T.M. Masikhwa, M.J. Madito, D. Momodu, T. Ntsoane, N. Manyala, Three dimensional vanadium pentoxide/graphene foam composite as positive electrode for high performance asymmetric electrochemical supercapacitor, J Colloid Interface Sci 532 (2018) 395–406. https://doi.org/10.1016/j.jcis.2018.08.010.

[66] T.M. Masikhwa, M.J. Madito, A. Bello, J.K. Dangbegnon, N. Manyala, High performance asymmetric supercapacitor based on molybdenum disulphide/graphene foam and activated carbon from expanded graphite, J Colloid Interface Sci 488 (2017) 155–165. https://doi.org/10.1016/j.jcis.2016.10.095.

[67] Y. Xi, B. Dong, Y. Dong, N. Mao, L. Ding, L. Shi, R. Gao, W. Liu, G. Su, L. Cao, Well-Defined, Nanostructured, Amorphous Metal Phosphate as Electrochemical Pseudocapacitor Materials with High Capacitance, Chemistry of Materials 28 (2016) 1355–1362. https://doi.org/10.1021/acs.chemmater.5b04343.

[68] H. Shao, N. Padmanathan, D. McNulty, C. O′Dwyer, K.M. Razeeb, Supercapattery Based on Binder-Free Co 3 (PO 4) 2 ·8H 2 O Multilayer Nano/Microflakes on Nickel Foam, ACS Appl Mater Interfaces 8 (2016) 28592–28598. https://doi.org/10.1021/acsami.6b08354.

[69] P.K. Katkar, S.J. Marje, V.G. Parale, C.D. Lokhande, J.L. Gunjakar, H.-H. Park, U.M. Patil, Fabrication of a High-Performance Hybrid Supercapacitor Based on Hydrothermally Synthesized Highly Stable Cobalt Manganese Phosphate Thin Films, Langmuir 37 (2021) 5260–5274. https://doi.org/10.1021/acs.langmuir.1c00243.

[70] S. Nivetha, S. Prabahar, R.T. Karunakaran, M.N. Ganth, T. Boobalan, S. Dhinesh, Improved Electrochemical Performance of Ni2P2O7 and Mn-doped Ni2P2O7 Electrode Materials for Supercapacitor Applications, ChemistrySelect 8 (2023). https://doi.org/10.1002/slct.202300535.

[71] P.K. Katkar, Z.A. Sheikh, V.D. Chavan, S.W. Lee, In-situ growth of 3D amorphous Ni-Co-Mn phosphate on 2D Ti3C2Tx nanocomposite for commercial-level hybrid energy storage application, J Mater Sci Technol 206 (2025) 282–296. https://doi.org/10.1016/j.jmst.2024.03.044.

[72] P.K. Katkar, A.N. Kadam, S.K. Jerng, S.H. Chun, S.W. Lee, Rational design of redox active amorphous Ni-Mn phosphate anchored on vertical graphene nanohills (VGNHs) for solid-state energy storage device, J Alloys Compd 968 (2023) 171935. https://doi.org/10.1016/j.jallcom.2023.171935.

[73] A.A. Kulkarni, N.K. Gaikwad, A.P. Salunkhe, R.M. Dahotre, T.S. Bhat, Transition metal phosphates: A paradigm for electrochemical supercapacitors, Journal of Electroanalytical Chemistry 948 (2023) 117795. https://doi.org/10.1016/j.jelechem.2023.117795.

[74] Q. Cheng, X. Zhao, G. Yang, L. Mao, F. Liao, L. Chen, P. He, D. Pan, S. Chen, Recent advances of metal phosphates-based electrodes for high-performance metal ion batteries, Energy Storage Mater 41 (2021) 842–882. https://doi.org/10.1016/j.ensm.2021.07.017.

[75] F. Li, Y.-L. Liu, G.-G. Wang, H.-Y. Zhang, B. Zhang, G.-Z. Li, Z.-P. Wu, L.-Y. Dang, J.-C. Han, Few-layered Ti 3 C 2 T x MXenes coupled with Fe 2 O 3 nanorod arrays grown on carbon cloth as anodes for flexible asymmetric supercapacitors, J Mater Chem A Mater 7 (2019) 22631–22641. https://doi.org/10.1039/C9TA08144E.

[76] R. Rajalakshmi, K.P. Remya, C. Viswanathan, N. Ponpandian, Enhanced electrochemical activities of morphologically tuned MnFe 2 O 4 nanoneedles and nanoparticles integrated on reduced graphene oxide for highly efficient supercapacitor electrodes, Nanoscale Adv 3 (2021) 2887–2901. https://doi.org/10.1039/D1NA00144B.

[77] M. Alzaid, M.Z. Iqbal, S. Siddique, N.M.A. Hadia, Exploring the electrochemical performance of copper-doped cobalt–manganese phosphates for potential supercapattery applications, RSC Adv 11 (2021) 28042–28051. https://doi.org/10.1039/D0RA09952J.

[78] M.Z. Iqbal, J. Khan, H.T.A. Awan, M. Alzaid, A.M. Afzal, S. Aftab, Cobalt–manganese-zinc ternary phosphate for high performance supercapattery devices, Dalton Transactions 49 (2020) 16715–16727. https://doi.org/10.1039/D0DT03313H.

[79] S.K. Meher, P. Justin, G. Ranga Rao, Microwave-Mediated Synthesis for Improved Morphology and Pseudocapacitance Performance of Nickel Oxide, ACS Appl Mater Interfaces 3 (2011) 2063–2073. https://doi.org/10.1021/am200294k.

[80] J. Cherusseri, S.A. Thomas, A.K. Pandey, M. Zaed, N.K. Farhana, R. Saidur, Rapid synthesis of cobalt manganese phosphate by microwave-assisted hydrothermal method and application as positrode material in supercapatteries, Sci Rep 14 (2024) 26550. https://doi.org/10.1038/s41598-024-77278-w.

[81] Y. Zhou, C. Liu, X. Li, L. Sun, D. Wu, J. Li, P. Huo, H. Wang, Chemical precipitation synthesis of porous Ni2P2O7 nanowires for supercapacitor, J Alloys Compd 790 (2019) 36–41. https://doi.org/10.1016/j.jallcom.2019.03.192.

[82] J. Theerthagiri, K. Thiagarajan, B. Senthilkumar, Z. Khan, R.A. Senthil, P. Arunachalam, J. Madhavan, M. Ashokkumar, Synthesis of Hierarchical Cobalt Phosphate Nanoflakes and Their Enhanced Electrochemical Performances for Supercapacitor Applications, ChemistrySelect 2 (2017) 201–210. https://doi.org/10.1002/slct.201601628.

[83] H. Petersen, N. Stegmann, M. Fischer, B. Zibrowius, I. Radev, W. Philippi, W. Schmidt, C. Weidenthaler, Crystal Structures of Two Titanium Phosphate-Based Proton Conductors: Ab Initio Structure Solution and Materials Properties, Inorg Chem 61 (2022) 2379–2390. https://doi.org/10.1021/acs.inorgchem.1c02613.

[84] M. Li, M. Li, M. Zhao, B. Wu, S. Mourdikoudis, S. Wei, F.M. Oliveira, J. He, L. Děkanovský, J. Luxa, S. Yang, Z. Sofer, Rational design of crystalline/amorphous nickel manganese phosphate octahydrate heterostructure for high-performance aqueous and all-solid-state asymmetric supercapacitors, Chemical Engineering Journal 482 (2024) 148895. https://doi.org/10.1016/j.cej.2024.148895.

[85] A.A. Mirghni, K.O. Oyedotun, O. Fasakin, B.A. Mahmoud, D.J. Tarimo, N. Manyala, High-performance bimetallic Ni-Mn phosphate hybridized with 3-D graphene foam

for novel hybrid supercapacitors, J Energy Storage 31 (2020) 101584. https://doi.org/10.1016/j.est.2020.101584.

[86] V. Sharmila, R. Packiaraj, N. Nallamuthu, M. Parthibavarman, Fabrication of MWCNTs wrapped nickel manganese phosphate asymmetric capacitor as a supercapattery electrode for energy storage applications, Inorg Chem Commun 121 (2020) 108194. https://doi.org/10.1016/j.inoche.2020.108194.

[87] A.A. Mirghni, K.O. Oyedotun, B.A. Mahmoud, A. Bello, S.C. Ray, N. Manyala, Nickel-cobalt phosphate/graphene foam as enhanced electrode for hybrid supercapacitor, Compos B Eng 174 (2019) 106953. https://doi.org/10.1016/j.compositesb.2019.106953.

[88] P.K. Katkar, S.J. Marje, S.S. Pujari, S.A. Khalate, A.C. Lokhande, U.M. Patil, Enhanced Energy Density of All-Solid-State Asymmetric Supercapacitors Based on Morphologically Tuned Hydrous Cobalt Phosphate Electrode as Cathode Material, ACS Sustain Chem Eng 7 (2019) 11205–11218. https://doi.org/10.1021/acssuschemeng.9b00504.

[89] S.J. Marje, P.K. Katkar, S.S. Pujari, S.A. Khalate, A.C. Lokhande, U.M. Patil, Regulated micro-leaf like nickel pyrophosphate as a cathode electrode for asymmetric supercapacitor, Synth Met 259 (2020) 116224. https://doi.org/10.1016/J.SYNTHMET.2019.116224.

[90] P.K. Katkar, S.J. Marje, S.S. Pujari, S.A. Khalate, P.R. Deshmukh, U.M. Patil, Single-pot hydrothermal synthesis of manganese phosphate microrods as a cathode material for highly stable flexible solid-state symmetric supercapacitors, Synth Met 267 (2020) 116446. https://doi.org/10.1016/J.SYNTHMET.2020.116446.

[91] Y. Dong, Y. Li, S. Shen, Y. Chen, D. Li, J. Hu, Y. Fu, H. Ma, D. He, J. Li, High-performance aqueous asymmetric supercapacitors based on a cathode of carbon nanotube/NiCo2O4 nanograss-supported MnCoP nanosheets on Ni foam, J Energy Storage 74 (2023) 109424. https://doi.org/10.1016/j.est.2023.109424.

[92] P.K. Katkar, S.A. Patil, J.H. Jeon, H.R. Na, N.S. Padalkar, S.K. Jerng, S. Lee, S.H. Chun, Urea-Assisted Nickel-Manganese Phosphate Composite Microarchitectures with Ultralong Lifecycle for Flexible Asymmetric Solid-State Supercapacitors: A Binder-Free Approach, Energy and Fuels 36 (2022) 13356–13369. https://doi.org/10.1021/acs.energyfuels.2c02875.

[93] X. Li, A.M. Elshahawy, C. Guan, J. Wang, Metal Phosphides and Phosphates-based Electrodes for Electrochemical Supercapacitors, Small 13 (2017). https://doi.org/10.1002/smll.201701530.

[94] Z. Xiao, Y. Bao, Z. Li, X. Huai, M. Wang, P. Liu, L. Wang, Construction of Hollow Cobalt–Nickel Phosphate Nanocages through a Controllable Etching Strategy for High Supercapacitor Performances, ACS Appl Energy Mater 2 (2019) 1086–1092. https://doi.org/10.1021/acsaem.8b01627.

[95] Y.H. Li, Q.Y. Li, H.Q. Wang, Y.G. Huang, X.H. Zhang, Q. Wu, H.Q. Gao, J.H. Yang, Synthesis and electrochemical properties of nickel–manganese oxide on MWCNTs/CFP substrate as a supercapacitor electrode, Appl Energy 153 (2015) 78–86. https://doi.org/10.1016/J.APENERGY.2014.09.055.

[96] A. Agarwal, S. Majumder, B.R. Sankapal, Carbon Nanotube-Functionalized Surface-Assisted Growth of Cobalt Phosphate Nanodots: A Highly Stable and Bendable All-Solid-State Symmetric Supercapacitor, Energy and Fuels 36 (2022) 5953–5964. https://doi.org/10.1021/acs.energyfuels.2c00600.

[97] Z. Abbas, M.R.A. Karim, W. Shehzad, N.A. Shama, J. Kumar, Sirajuddin, S. Karakuş, R.A. Soomro, A. Nafady, Exploring the electrochemical utilization of PANI/CNT-integrated Ni-Mn phosphates for advanced supercapacitor applications, Electrochim Acta 471 (2023). https://doi.org/10.1016/j.electacta.2023.143350.

[98] A.A. Mirghni, K.O. Oyedotun, O. Fasakin, B.A. Mahmoud, D.J. Tarimo, N. Manyala, High-performance bimetallic Ni-Mn phosphate hybridized with 3-D graphene foam for novel hybrid supercapacitors, J Energy Storage 31 (2020) 101584. https://doi.org/10.1016/j.est.2020.101584.

CHAPTER 3

CHARACTERISATION TECHNIQUES

3.1 Introduction

In this study, the characteristics of the synthesised materials were systematically examined through a combination of physicochemical and electrochemical analyses. The techniques employed included Scanning Electron Microscopy (SEM), Energy Dispersive X-ray Spectroscopy (EDS), High-Resolution Transmission Electron Microscopy (HR-TEM), Fourier Transform Infrared Spectroscopy (FTIR), X-ray Diffraction (XRD), X-ray Photoelectron Spectroscopy (XPS), Raman Spectroscopy, Cyclic Voltammetry (CV), Galvanostatic Charge-Discharge (GCD), and Electrochemical Impedance Spectroscopy (EIS). SEM, EDS, HR-TEM, FTIR, Raman, and XPS analyses were utilised to investigate the morphology, elemental composition, phase structure, surface chemistry, and bonding characteristics of EEG, $NiMn(PO_4)_2$, and $NiMn(PO_4)_2$/EEG nanomaterials. These methods provided valuable insights into the structural evolution and compositional changes occurring throughout synthesis, which directly affect the electrochemical behaviour of the resulting materials. Electrochemical techniques, including CV, GCD, and EIS, were subsequently applied to evaluate the redox activity, charge-discharge characteristics, reaction kinetics, capacitive and diffusion-controlled processes, cycling stability, coulombic efficiency, and impedance behaviour as a function of frequency. This chapter, therefore, presents an overview of these complementary techniques, each of which contributes to a comprehensive understanding of the physicochemical and electrochemical properties of the synthesised materials.

3.2 Scanning Electron Microscopy

The Scanning Electron Microscope was developed in the early twentieth century by researchers at the Technical University of Berlin, who employed a stream of electrons to produce high-resolution images of sample surfaces [3,4]. SEM functions by accelerating a beam of electrons to high energies, resulting in an exceptionally short wavelength. The diameter of the electron beam typically ranges from around 15 to 20 µm; however, to obtain a smaller beam diameter of approximately 0.5-5 nm, a field emission electron gun is used [5]. This short wavelength allows the SEM to generate diffraction effects at extremely small physical dimensions, enabling the resolution of atomic-scale features in the nanometre-to-micrometre range [5] . Consequently, the high-energy, short-wavelength electrons enable visualisation of very fine surface features at near-atomic resolution.

Every SEM system consists of four key components: an electron column, a sample chamber, a range of detectors, and a display or viewing system. The electron column houses the electron gun typically tungsten, LaB_6, or field emission together with magnetic lenses, beam-defining apertures, and scanning coils (see **Figure 3.1**). The electron gun produces a primary electron beam, which is focused and converged by electromagnetic lenses into a fine spot that scans the specimen surface in a raster pattern [3,4][6][5]. The microscope operates under high-vacuum conditions to prevent interference from gas molecules that could scatter the electrons and degrade image resolution [6].

As the electron beam interacts with the specimen, various signals such as secondary and backscattered electrons are produced and detected. These signals are amplified, digitised, and synchronised with the scanned region to form a high-resolution, real-time image on the display screen, which can be saved for subsequent analysis [5]. When the primary electrons strike the sample surface, they interact with the constituent atoms, leading to the emission of several types of signals. The incident electrons lose kinetic energy as they penetrate the material through both elastic and inelastic scattering processes [5,6].

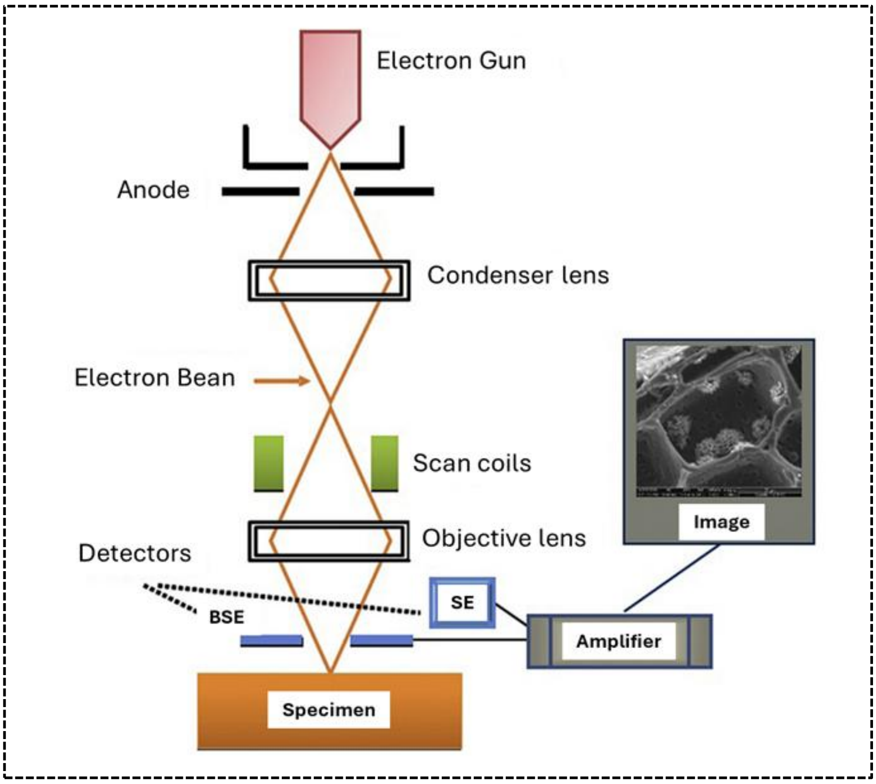

Figure 3.1 Schematic drawing of a scanning electron microscope. Reprinted from Ref. [7]. Copyrights 2019, Elsevier.

As depicted in **Figure 3.2**, these interactions give rise to multiple emissions, including secondary electrons, backscattered electrons, Auger electrons, characteristic X-rays, and visible light (cathodoluminescence). The extent of these electron sample interactions depends on parameters such as the atomic number of the material, atomic concentration, and the energy of the incident electron beam, which is controlled by the accelerating voltage. Increasing the accelerating voltage generally enlarges the scattering process and the interaction volume within the specimen. Conversely, materials with higher atomic numbers and electron densities tend to produce stronger scattering effects, which enhance contrast but reduce interaction volume and image resolution [5].

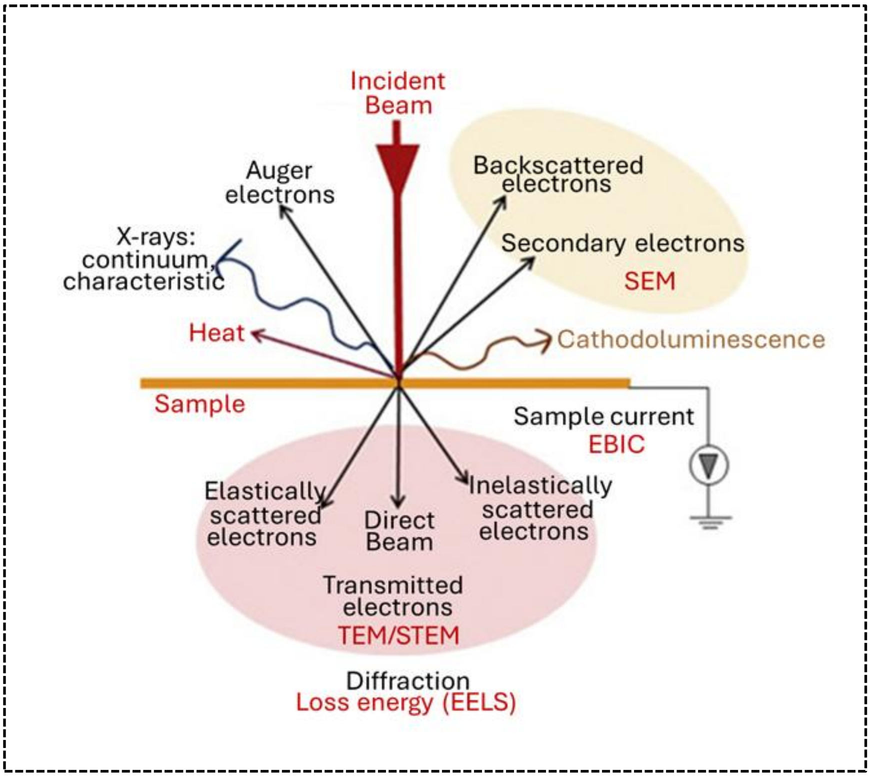

Figure 3.2 The association between the primary electron beam and the emitted signals from the sample. Reprinted from Ref. [7]. Copyrights 2019, Elsevier.

The incident angle of the electron beam relative to the sample surface also influences the interaction volume. Materials with high atomic numbers absorb more electrons, resulting in smaller interaction regions [5]. At higher accelerating voltages, the electrons possess greater energy and penetrate deeper into the sample, thereby increasing the interaction volume [5]. In contrast, increasing the angle of incidence (away from the normal) reduces the interaction depth [5]. All emitted electrons and secondary signals are collected by detectors that convert them into electrical outputs, which are then processed to produce a detailed image of the surface morphology.

Overall, SEM provides comprehensive insights into surface topography, morphology, particle size and shape, elemental distribution, phase composition, and microstructural arrangement. It is particularly valuable for imaging materials that require precise surface detail, including microelectronic components, nanomaterials, and biological specimens.

3.3 Energy Dispersive X-Ray Spectroscopy

In this study, particular attention was given to the use of Energy Dispersive X-ray Spectroscopy in conjunction with SEM. EDS is an analytical method employed in electron microscopy to determine the elemental composition of a sample [8]. The technique operates by detecting and analysing the characteristic X-rays emitted when a specimen is bombarded with a high-energy electron beam [8].

The principle underlying EDS is that when a focused primary electron beam, typically with energies up to 30 keV, interacts with the atoms of a specimen, energy is transferred through inelastic collisions. This process results in the ejection of inner-shell electrons and the formation of vacancies within the atomic structure (see **Figure 3.3**) [9]. As shown in **Figure 3.3(a)**, ionisation occurs most efficiently when the energy of the incident electrons is approximately two to three times greater than the binding energy of the electron shell being examined [9,10]. Beyond this range, the probability of ionisation gradually decreases, while if the primary electron energy is only slightly higher than the binding energy of the target shell, the likelihood of ionisation falls significantly [9,10].

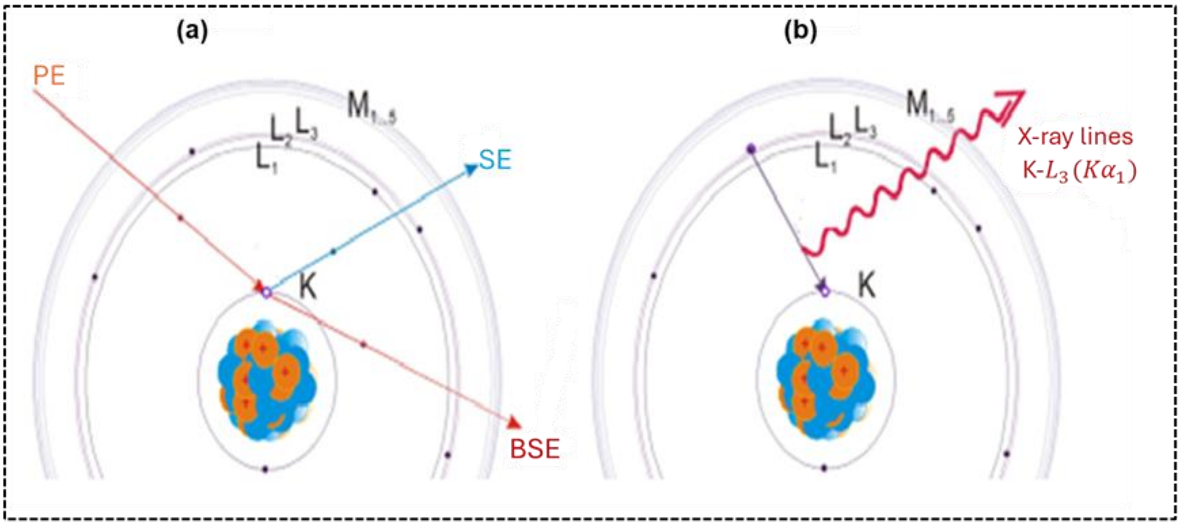

Figure 3.3. Schematic representation of the characteristic X-ray emission mechanism: (a) Interaction of a primary electron with a sample atom producing a K-shell vacancy and (b) subsequent relaxation by an L_3 -K transition emitting a characteristic X-ray photon. Reprinted with permission from ref [9]. Copyright 2018 Springer Nature.

Once ionisation takes place, the atom becomes unstable and enters an excited state. As illustrated in **Figure 3.3(b)**, an electron from an outer shell subsequently transitions to fill the inner-shell vacancy, releasing energy in the form of an X-ray photon that is characteristic of that particular element [8]. These emitted X-rays are then detected by an energy-dispersive detector situated close to the specimen. The detector measures the energy of each photon and identifies the corresponding characteristic peaks, which are unique to each element present within the sample [10].

The resulting EDS spectrum plots the characteristic X-ray energies on the horizontal axis and their relative intensities on the vertical axis, providing a representation of the abundance of each detected element. As the energy of the emitted X-rays is directly proportional to the atomic number of the element, the EDS spectrum provides both qualitative and semi-quantitative information regarding the elemental composition and relative concentrations within the analysed region of the specimen [9].

Overall, EDS is an indispensable technique for compositional characterisation. It offers valuable insights into the elemental makeup of a broad range of materials, including metals, ceramics, semiconductors, biological tissues, and geological samples. When combined with SEM imaging, EDS enables spatially resolved elemental mapping, allowing researchers to correlate morphological features with compositional variations at micro- and nanoscale levels.

3.4 Transmission Electron Microscopy

Transmission Electron Microscopy is a highly powerful imaging technique used to examine the internal structure, morphology, and composition of materials at micro- to nanoscale resolution [11]. Unlike optical microscopes, which utilise visible light, TEM employs a focused beam of high-energy electrons transmitted through an ultrathin sample to generate highly detailed images [7]. Because electrons possess much shorter de Broglie wavelengths than visible light, TEM can achieve spatial resolutions of around 0.05 nm and magnifications of up to nearly 10,000,000× [7].

TEM operates on the principle that an electron source, commonly a tungsten filament, lanthanum hexaboride (LaB_6), or a field emission gun, emits a beam of electrons that is then accelerated, narrowed, and focused onto the specimen using a series of electromagnetic lenses composed of precision wire coils [12,13]. As illustrated in **Figure 3.2**, when the high-energy electron beam interacts with a thin sample, various signals are produced due to electron matter interactions. These interactions are broadly categorised as elastic or inelastic scattering.

In elastic interactions, the electrons are deflected by the Coulombic forces of the atomic nuclei without any significant energy loss [13]. In contrast, inelastic interactions involve an exchange of energy between the incident electrons and the atoms in the sample, leading to a reduction in the kinetic energy of the transmitted electrons [13]. Inelastic scattering gives rise to several detectable signals, such as characteristic X-rays, Auger electrons, secondary electrons, backscattered electrons, cathodoluminescence, and inelastically scattered transmitted electrons [13]. The electrons that pass through the specimen contain valuable information regarding the internal structure and composition of the material. These transmitted electrons are focused by the objective lens onto a detector, forming an image that reflects the internal morphology and crystallography of the sample. Common detection systems include fluorescent screens, photographic films, and, in modern instruments, high-sensitivity digital cameras capable of real-time imaging and electron diffraction pattern acquisition [7].

Electron diffraction patterns are produced when the incident electron beam interacts with the periodic atomic arrangement of crystalline materials, allowing the determination of lattice parameters and crystallographic structures [14]. TEM thus provides not only high-resolution imaging but also diffraction data for structural analysis. To ensure optimal imaging conditions, TEM operates under ultrahigh vacuum to prevent unwanted scattering of electrons by gas molecules and to minimise contamination of both the sample surface and the electron source [6]. The specimens must be extremely thin, typically less than 100 nm, to allow electrons to transmit through the material [15]. Several methods are available for specimen preparation, including ultramicrotomy, ion milling, and focused ion beam (FIB) milling [12,15].

In summary, TEM provides exceptional capability for visualising and analysing materials at the nanoscale. By transmitting and manipulating high-energy electrons through a thin specimen, TEM enables the acquisition of both high-resolution images and diffraction data, revealing the structural, morphological, and compositional properties of materials with near-atomic precision.

3.5 X-Ray Photoelectron Spectroscopy

X-ray Photoelectron Spectroscopy is a surface-sensitive analytical technique widely used to determine the elemental composition and to investigate the chemical and electronic states of materials. In XPS, the absorption of X-ray photons by a sample leads to the ejection of core (inner-shell) electrons from the atoms on its surface, as illustrated in **Figure 3.4** [16]. The incident X-rays are monochromatic and possess a well-defined energy that excites the surface atoms, causing them to emit photoelectrons [16].

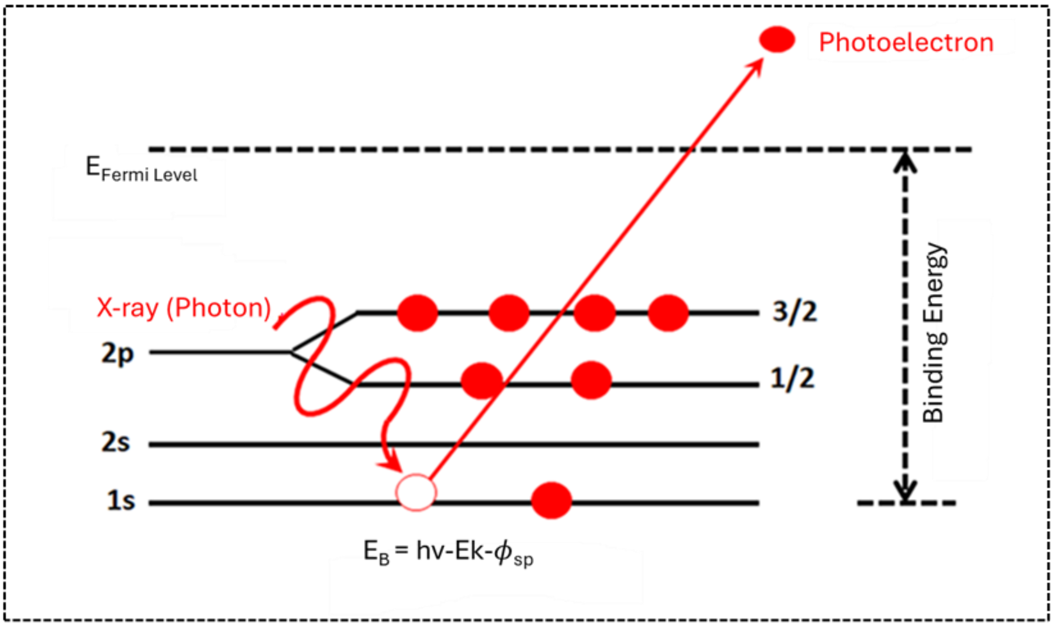

Figure 3.4. Schematic illustration of the photoelectric effect. Reprinted from Ref. [16].

The kinetic energies of the emitted photoelectrons generally fall within the range of 300-1500 keV [17]. Their kinetic energy is governed by the law of energy conservation, which relates the incident photon energy to the electron binding energy and the spectrometer's work function. Electrons located near the material's surface are able to escape without significant energy loss, as they experience minimal inelastic scattering. These unscattered electrons appear as sharp photoelectron peaks in the spectrum, each corresponding to the specific binding energy of a core-level electron [17]. In contrast, electrons that undergo inelastic energy losses contribute to the continuous background signal in the spectrum. The emitted photoelectrons are collected and analysed by an electron energy analyser, which measures their kinetic energies. The resulting XPS spectrum records the number of detected photoelectrons as a function of their binding energy (E_B). The binding energy is determined using the known photon energy (hν) and the measured kinetic energy (E_K), according to the energy conservation equation presented at the bottom of **Figure 3.4** [16].

Each element exhibits a unique set of binding energies corresponding to its electronic configuration. As a result, the observed peaks can be used to identify the elements present within the sample, while the intensity of these peaks is directly proportional to their concentration [16]. Following background subtraction, the integrated peak areas corrected using empirical sensitivity factors enable quantitative elemental analysis [16]. Therefore, detailed interpretation of the XPS spectrum provides information not only about the elemental composition but also about the chemical and oxidation states of atoms on the material's surface. XPS data can be acquired in two distinct modes: wide-scan (survey scan) and narrow-scan (high-resolution scan). The wide-scan mode offers an overview of the surface composition across a broad energy range, typically up to 1200 eV, whereas the narrow-scan mode focuses on selected core-level regions with higher resolution, allowing the identification of oxidation states and bonding environments [17].

Overall, XPS is a vital characterisation technique that provides in-depth insights into surface chemistry, electronic structure, and bonding environments. It is particularly valuable for the analysis of thin films, coatings, and interfaces, where surface composition and electronic behaviour critically influence material performance.

3.6 Fourier Transform Infrared Spectroscopy

Fourier Transform Infrared Spectroscopy is an analytical technique employed to determine the chemical composition and molecular structure of materials by measuring the absorption or transmission of infrared (IR) radiation [18]. It operates within the infrared spectral range of approximately 2 to 30 μm [17]. Within this wavelength region, the photon energies are too low to excite the electronic states of atoms; instead, they induce transitions in the vibrational and rotational energy levels of molecules [19]. Because every molecule exhibits vibrational and rotational motions at characteristic frequencies, FTIR can be used to identify specific molecular groups and chemical bonds, provided that these transitions satisfy the dipole selection rule [17]. The technique is therefore particularly useful for identifying functional groups and for studying the molecular interactions and bonding environments in both organic and inorganic materials.

A typical FTIR spectrometer comprises a Michelson interferometer, movable mirrors, a broadband infrared radiation source, a beam splitter, and a detector **(Figure 3.5)** [17]. During measurement, an infrared beam is directed through the sample. As the radiation interacts with the sample molecules, certain wavelengths are absorbed, corresponding to the vibrational modes of specific molecular bonds, while the remaining radiation passes through the sample and is detected. The detector produces a signal proportional to the intensity of the transmitted radiation as a function of time. This raw signal known as an interferogram is then mathematically converted from the time domain to the frequency domain using a Fourier Transform, producing an IR spectrum that displays absorption intensity as a function of wavelength or wavenumber [18]. The resulting spectrum contains distinct absorption peaks that correspond to the vibrational frequencies of specific chemical bonds and functional groups present in the material. Because each type of bond absorbs infrared light at a characteristic frequency, FTIR spectra act as molecular fingerprints, allowing for precise identification of compounds and verification of chemical structures [21].

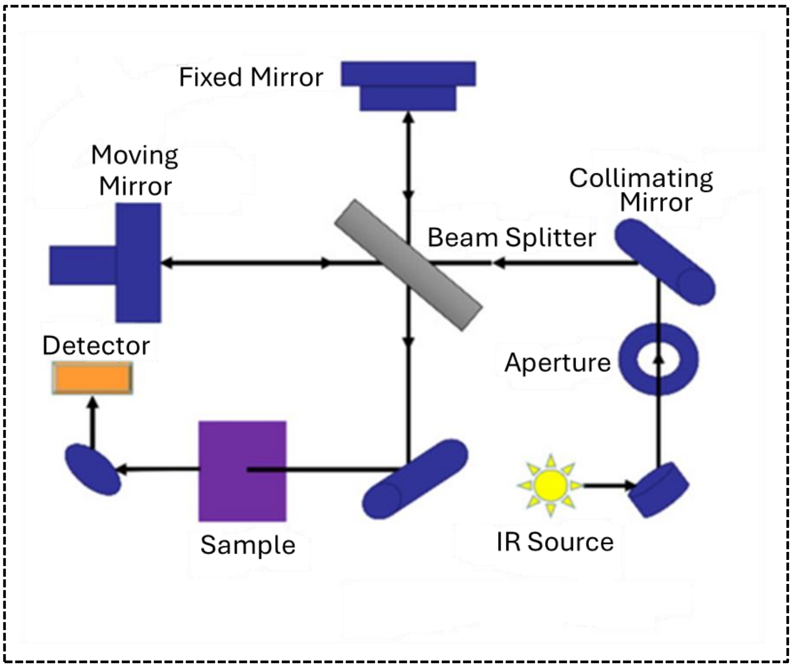

Figure 3.5. Schematic representation of the functional components of an FTIR spectrometer. Reprinted with permission from Ref.[20], Copyright 2022, CC BY 4.0.

FTIR is an essential tool for both qualitative and quantitative analysis of molecular composition, bonding, and functional groups in solids, liquids, and gases. Owing to its accuracy, rapid data acquisition, and non-destructive nature, it is widely used across disciplines, including materials science, chemistry, biology, pharmaceuticals, forensics, and environmental analysis.

3.7 Raman Spectroscopy

Raman spectroscopy is an analytical technique used to examine the molecular composition of materials by probing their rotational, vibrational, and other low-frequency characteristics [22]. The method is based on the Raman scattering phenomenon, which occurs when monochromatic light, typically from a laser source, interacts with the molecular vibrations of a material [22]. As a non-destructive technique, Raman spectroscopy provides detailed information about molecular structure, crystallinity, and intermolecular interactions through the analysis of light-matter interactions [23]. When a sample is illuminated by a laser beam, the incident photons interact with the molecules, causing a temporary distortion of the electron cloud and the formation of a short-lived, high-energy virtual state. Most scattered photons do not exchange energy with the sample molecules but only change their direction of propagation. This elastic scattering process, known as Rayleigh scattering, leaves the frequency of the scattered photons identical to that of the incident light [24,25]. A small fraction of the scattered photons, however, do undergo energy exchange with the molecules, resulting in changes in both frequency and propagation direction. This inelastic scattering process is referred to as Raman scattering and is illustrated in **Figure 3.6(a)**.

Raman scattering is further classified into Stokes and anti-Stokes processes. In Stokes scattering, the incident photon transfers part of its energy to the molecule, causing the scattered photon to emerge with a lower frequency (and hence lower energy) [26]. Conversely, in anti-Stokes scattering, some molecules are already in excited vibrational states; upon interaction, they transfer energy to the incident photon, producing a scattered photon of higher frequency **(Figure 3.6(b))**. The difference in frequency between the incident and scattered photons is known as the Raman shift (Δv, in cm^{-1}) [23]. The scattered light is collected and directed into a spectrometer, which separates the photons by wavelength and measures their intensities to generate a Raman spectrum. This spectrum reveals the vibrational and rotational modes of the sample's molecules, thereby providing crucial information about chemical bonds and molecular structures. Typically, metal ligand vibrations appear in the low-frequency region (<600 cm^{-1}), whereas higher-frequency regions correspond to functional group vibrations within the material.

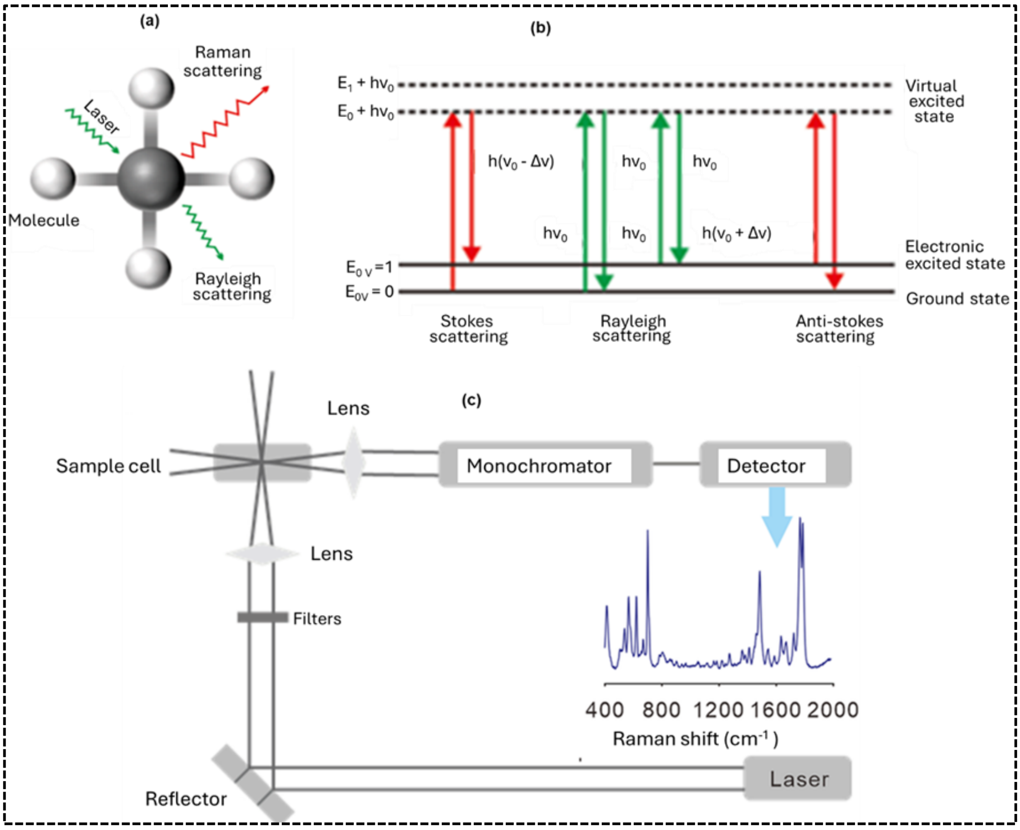

Figure 3.6 Schematic diagram of Raman spectroscopy principles. (a) Light scattering patterns of molecules. (b) Energy level transition diagram involved in Raman spectroscopy, (c) Diagram of a typical Raman spectrometer. Reprinted with permission from Ref. [27]. Copyrights 2024 John Wiley & Sons.

A standard Raman spectrometer **(Figure 3.6(c))** comprises a laser source, sample cell, optical filters, monochromator, and detector. The laser plays a critical role, providing monochromatic light that is directed to the sample via optical fibres before being collected for analysis. The performance of the Raman system depends primarily on three parameters: the laser type, wavelength, and spot size. Commonly used laser sources include argon (488.8 nm), krypton (568 nm), helium-neon (He-Ne, 632.8 nm), and neodymium-doped yttrium aluminium garnet (Nd:YAG, 532 nm) lasers for visible light applications, as well as diode (785 nm) and Nd:YAG (1064 nm) lasers for near-infrared excitation [27]. Because Raman scattering is inherently much weaker than Rayleigh scattering, spectrometers employ optical filters to suppress the intense Rayleigh signal, ensuring only Raman-scattered photons reach the detector. Detectors are equally crucial in capturing these weak optical signals. Depending on analytical requirements, commercial Raman instruments typically use photomultiplier tubes (PMTs), charge-coupled device (CCD) detectors, or indium gallium arsenide (InGaAs) detectors [27].

In summary, Raman spectroscopy serves as a highly versatile and non-invasive technique for analysing molecular vibrations, crystal structures, and chemical bonding. Its ability to deliver precise, non-destructive analysis makes it indispensable in materials science, chemistry, nanotechnology, and life sciences research.

3.8 X-Ray Diffraction

X-ray diffraction is a powerful analytical method used to investigate the atomic and molecular structures of both crystalline and non-crystalline (amorphous) materials [28]. The technique is based on the principle of constructive interference of X-rays scattered by the regularly arranged atoms in a crystal lattice [28].

A typical XRD instrument comprises an X-ray tube, an X-ray source, a sample holder, and a detector **(Figure 3.7)** [28]. When X-rays are directed onto a crystalline sample, they interact with the atoms in the lattice, resulting in the scattering of X-rays in various directions [28]. As illustrated in **Figure 3.8(a)**, the characteristic radiation lines produced by the X-ray source include several emissions, of which only the Kα radiation is typically used; other wavelengths are filtered out using monochromators to improve precision. When the incident X-rays strike the sample surface, the scattered radiation may occur either elastically or inelastically. Elastic scattering takes place when the outgoing photon energy equals that of the incoming photon, whereas inelastic scattering involves a change in energy, producing constructive or destructive interference. Only the diffraction peaks arising from constructive interference are analysed, as they satisfy Bragg’s law; peaks resulting from destructive interference are not considered [29].

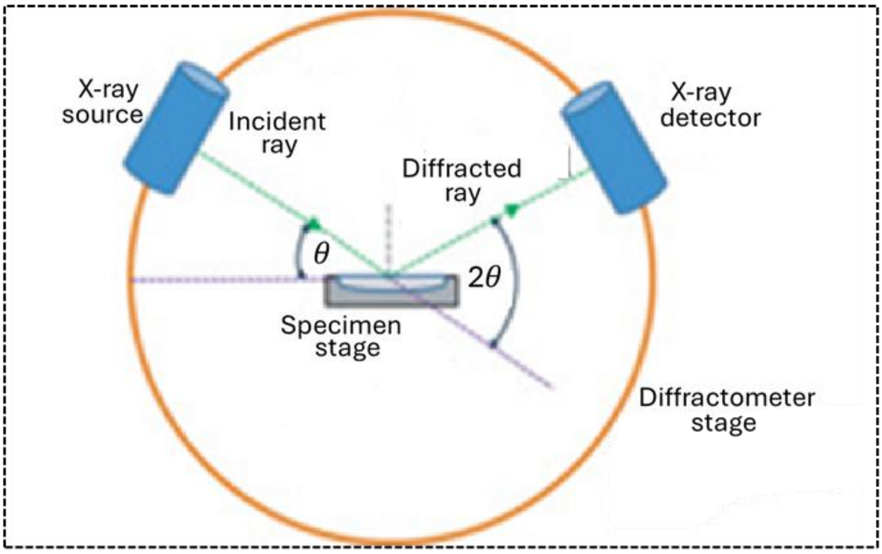

Figure 3.7 Schematic illustration of the XRD Components. Reprinted from Ref. [29] Copyright 2016, Elsevier Ltd.

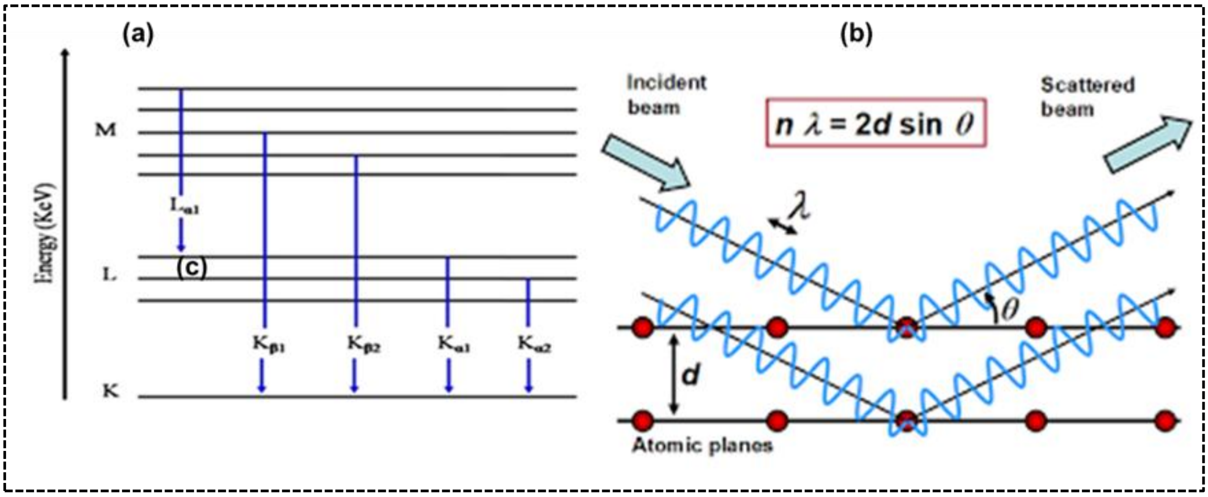

Figure 3.8. (a) Emission of characteristic X-rays. Reprinted with permission from Ref. [28], Copyright 2017, Elsevier Inc. (b) Diffraction from lattice planes. Reprinted from Ref. [29] Copyright 2016, Elsevier Ltd.

The condition for diffraction is described mathematically by Bragg's law **(Figure 3.8(b)):**

$$2d \sin\theta = n\lambda; n = 1,2,3 \tag{3.1}$$

where d represents the interplanar spacing between atomic layers, θ is the incident (Bragg) angle, λ is the wavelength of the X-rays, and n is an integer representing the order of reflection.

During an XRD measurement, the detector records the intensity of the diffracted X-rays at different angles, producing a diffraction pattern characteristic of the material. In crystalline materials, the resulting pattern displays sharp, well-defined peaks at specific diffraction angles corresponding to lattice planes [28]. By contrast, amorphous materials exhibit broad, diffuse humps in their diffraction patterns, reflecting the lack of long-range atomic order [28]. Crystallographic planes are identified using Miller indices (*hkl*), which represent the reciprocal intercepts of the planes with the unit cell axes. These indices provide information about the orientation and arrangement of atoms within the lattice [28]. When a single crystal is irradiated, its XRD pattern consists of discrete diffraction spots at specific angular positions corresponding to individual planes. In polycrystalline materials, however, these spots merge into concentric rings due to the random orientation of numerous crystallites.

Each XRD pattern contains a unique set of peaks characteristic of the atomic arrangement within the crystal structure. By analysing the position, intensity, and shape of these peaks, information can be obtained regarding the crystal structure, lattice parameters, degree of crystallinity, and preferred orientation (texture) of the material.

3.9 Cyclic Voltammetry

Cyclic Voltammetry is a fundamental electrochemical technique widely employed to investigate the redox behaviour, electrochemical reactions, and stability of materials or species in solution. It provides valuable insights into charge-transfer mechanisms and the electrochemical properties of electrode materials. In the context of energy storage systems, CV is often the initial characterisation method used to evaluate the thermodynamics of redox processes and to determine the potential window of electroactive species [31,32].

The relationship between the applied potential and the resulting current reveals key information about the phenomena occurring at the electrode electrolyte interface. This correlation enables the analysis of charge separation, ion diffusion, and electron-transfer kinetics parameters that are essential for understanding the reaction mechanisms governing energy storage behaviour [32].

A standard CV experiment typically employs a three-electrode electrochemical cell configuration comprising a working electrode, a counter (or auxiliary) electrode, and a reference electrode, as shown in **Figure 3.9(b).** The working electrode is fabricated from the material under investigation, while the reference electrode possesses a stable and well-known potential against which the working electrode's potential is measured. The counter electrode completes the circuit, facilitating current flow and maintaining charge neutrality within the system. Alternatively, a two-electrode configuration may be used, consisting of a positive and a negative electrode between which a potential difference is applied. This setup is commonly adopted for full-cell measurements to simulate practical device operation, such as in supercapacitors and batteries.

In a typical CV test, a linearly varying potential is applied to the working electrode over a defined potential range, sweeping from a lower to a higher potential limit and then back again to generate a cyclic potential waveform [33]. The resulting current response is recorded as a function of potential. The magnitude of this current is directly related to the rate of electrochemical reactions occurring at the electrode-electrolyte interface [33]. By plotting current versus potential, a cyclic voltammogram is obtained, which exhibits characteristic peaks or shapes reflecting the system's redox activity, reversibility, and kinetics.

The shape of the cyclic voltammogram provides critical information about the underlying charge storage mechanism. Electric double-layer capacitors (EDLCs) and pseudocapacitors typically display near-rectangular CV curves indicative of capacitive charge storage **(Figure 3.9(a,d))**. In contrast, battery-type and hybrid systems exhibit non-linear CV profiles with distinct redox peaks or potential plateaus, characteristic of Faradaic charge storage processes **(Figure 3.9(c,e))** [31,32,34]. Accordingly, the electrochemical behaviour of materials can generally be classified into three categories:

i. Capacitive Faradaic charge storage
ii. Capacitive non-Faradaic charge storage
iii. Non-capacitive Faradaic charge storage [32].

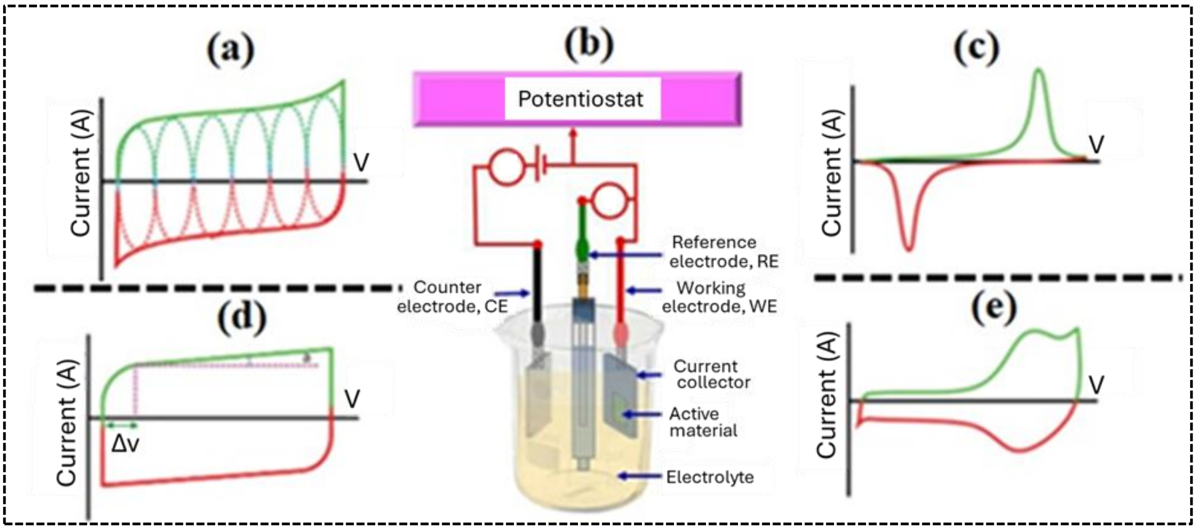

Figure 3.9. (a) Characteristic CV curve for a pseudocapacitor [32], (b) Illustration of a three-electrode setup. (c) Characteristic CV curve for battery [32], (d) Characteristic CV curve for an electric double layer capacitor [32], (e) Characteristic CV curve for a hybrid supercapacitor [32]. (a-e) Reprinted with permission from Ref. [32], Copyright 2019, Royal Society of Chemistry.

An important parameter in CV analysis is the operating potential window (OPW) of the electrode material, as it directly influences both energy storage performance and long-term stability. The OPW defines the maximum potential range within which the electrode operates without decomposition or electrolyte degradation. In a two-electrode system, the positive and negative electrodes are assigned distinct potential limits: the positive electrode between E_{P1} and E_{P2}, and the negative electrode between E_{N1} and E_{N2}, as shown in **Figure 3.10** [32,35]. The overall potential difference between the lower and upper limits corresponds to the device's operating potential window.

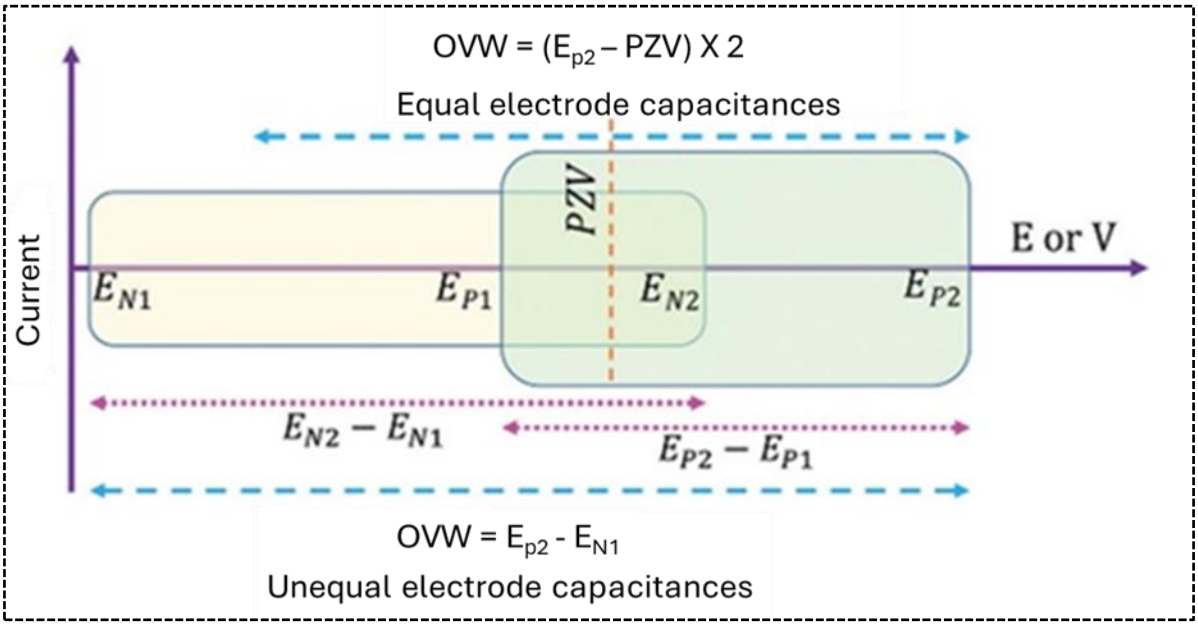

Figure 3.10. Depiction of the OPW of the positive and negative electrodes and the OVW of a characteristic asymmetric device [45]. Reprinted with permission from Ref [45]. Copyright 2019, Royal Society of Chemistry.

When the OPWs of the positive and negative electrodes overlap ($E_{N2} > E_{P1}$), the device's operating voltage window (OVW) becomes smaller than the sum of the individual OPWs [32]. If one electrode's OPW entirely encompasses the other, the overall voltage window is limited by the electrode with the smaller OPW. Conversely, when the OPWs of both electrodes do not intersect, the device exhibits a minimum discharge voltage [32].

The OVW is also influenced by the potential of zero voltage (PZV), defined as the potential across the device terminals when it is fully discharged and both electrodes possess equal potentials. For electrodes with equal capacitances, the OVW can be expressed as [32,35]:

$$\mathrm{OVW} = 2 \times (E_{P2} - \mathrm{PZV}); \mathrm{if PZV} - E_{N2} > E_{P1} - \mathrm{PZV} \qquad (3.2)$$

$$\mathrm{OVW} = 2 \times (\mathrm{PZV} - E_{N2}); \mathrm{if}\ (E_{P1} - \mathrm{PZV}) > (\mathrm{PZV} - E_{N2}) \qquad (3.3)$$

For electrodes with unequal capacitances, the OVW is defined by the potential difference between the upper and lower limits of the positive and negative electrodes, respectively [32]:

$$OVW = E_{P2} - E_{N1} \qquad (3.4)$$

The specific capacitance C_S of an individual electrode can be determined from CV data using:

$$C_S = \frac{q}{mV} (F\ g^{-1}) \qquad (3.5)$$

where q is the total charge (C), m is the mass of the active material (g), and V is the OPW (V). The total charge $q_{(+/-)}$ can be expressed as:

$$q_{(+/-)} = I \times t \qquad (3.6)$$

Substituting Equation (3.6) into Equation (3.5) gives:

$$C_{S(+/-)} = \frac{I\times t}{mV_{\left(\frac{+}{-}\right)}} \tag{3.7}$$

$$C_{S(+/-)} = \frac{I}{mv} \tag{3.8}$$

$$C_{S-/+}mv = I \tag{3.9}$$

where $v = \frac{V_{(+/-)}}{t}$is the potential sweep rate (V s^{-1}). Since current varies with potential during a CV scan, the integral form is:

$$\int_{V1}^{V2} C_{S+/-}mv\, dV = \int_{V1}^{V2} I(V)dV \tag{3.10}$$

Simplifying, the specific capacitance becomes:

$$C_{S-/+} = \frac{\int_{V1}^{V2} I(V)dV}{vm_{+\backslash-}\Delta V_{+/-}}(F\, g^{-1}) \tag{3.11}$$

where $\int_{V1}^{V2} I(V)dV$represents the enclosed CV area (A·V), v is the scan rate (V s^{-1}), and ΔV is the potential window (V). The simplified form is:

$$C_{S(+/-)} = \frac{\text{Area}}{2\times vm_{(+/-)}\Delta V_{(+/-)}} \tag{3.12}$$

Thus, CV provides critical insights into the electrochemical performance of electrode materials under both three-electrode (individual) and two-electrode (full-cell) configurations.

3.10 Galvanostatic Charge-Discharge

The Galvanostatic Charge-Discharge technique is a fundamental electrochemical method used to evaluate the performance and behaviour of energy storage devices such as supercapacitors, batteries, and fuel cells. It involves applying a constant current (CC) during both charging and discharging processes.

During the charging phase, a constant current is applied, leading to the accumulation of electrical energy within the electrode materials [36]. Charging proceeds until a specified cut-off voltage or capacity is reached, after which the current is reversed or set to zero, initiating the discharge phase. The voltage then decreases with time as the stored energy is released through a reverse current flow until a pre-defined lower voltage limit is attained [32].

The voltage-time (or current-time) responses obtained during charging and discharging reveal key performance parameters such as specific capacity, voltage efficiency, energy efficiency, and power capability. The shapes of GCD curves differ according to the charge storage mechanism. EDLCs and pseudocapacitors typically exhibit linear or quasi-triangular profiles **(Figure 3.11(a))**, while hybrid and battery-type materials display nonlinear profiles due to Faradaic redox reactions **(Figure 3.11(b,c))** [37–39]. Two main distinctions exist between batteries and pseudocapacitors:

i. Phase Transformations: Battery electrodes undergo phase transformations during cycling, resulting in distinct redox plateaus in GCD curves. In contrast, pseudocapacitive materials exhibit near-rectangular CVs and linear GCD responses.

ii. Kinetic Behaviour: In batteries, the redox reactions are diffusion-controlled ($I \propto v^{0.5}$), whereas in pseudocapacitive systems, surface-controlled kinetics dominate ($I \propto v$ signifying rapid and reversible Faradaic reactions.

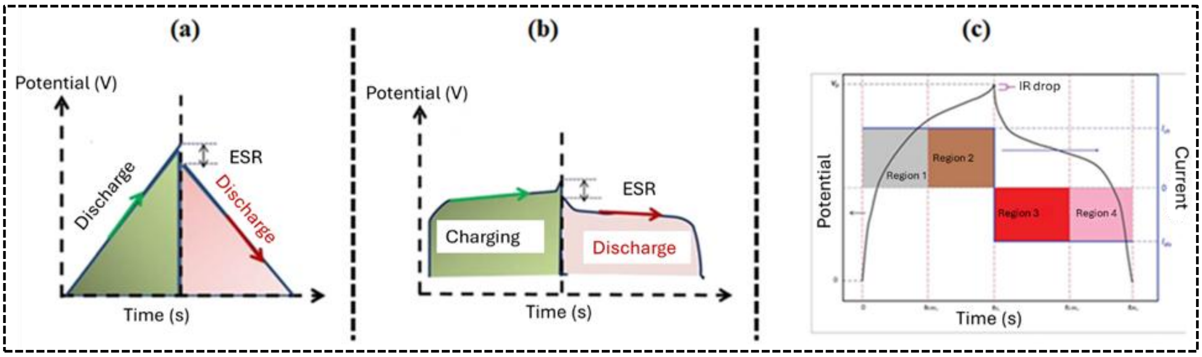

Figure 3.11. GCD profiles with the electrochemical characteristics of a typical (a) pseudocapacitor or EDLC, (b) battery, and (c) hybrid supercapacitor. (a-b) Reprinted with permission from Ref. [34], Copyright 2022, Walter De Gruyter GmbH. (c) Reprinted with permission from Ref. [36], Copyright 2014, John Wiley and Sons.

Hybrid systems combine both mechanisms, displaying mixed features of capacitive and battery-type behaviour [47]. Although distinguishing these mechanisms solely from voltammogram shapes is challenging, quantitative methods exist to separate and analyse diffusion- and surface-controlled contributions [32,40–46].

The specific capacitance (C_S) for capacitive electrodes with linear GCD profiles can be calculated as:

$$C_S = \frac{I \times t}{mV} \tag{3.13}$$

For a single electrode in a three-electrode setup:

$$C_S = \frac{I_{\text{discharge}} \times t_{\text{discharge}}}{mV} \; (F\, g^{-1}) \tag{3.14}$$

For nonlinear discharge profiles, the capacitance is obtained by integrating the discharge area [47–49]:

$$C_S = \frac{2I}{mV^2} \int V(t)\, dt \; (F\, g^{-1}) \tag{3.15}$$

For battery-type electrodes, the specific capacity (Q_S) is expressed as [37,39,47–49]

$$Q_S = \frac{I \times t}{3.6m} \; (mA\, h\, g^{-1}) \tag{3.16}$$

where V is the potential window (V), I is the discharge current (A), m is the active mass (g), and t is the discharge time (s).

3.11 Electrochemical Impedance Spectroscopy

Electrochemical Impedance Spectroscopy is a versatile technique used to study the electrochemical and electrical behaviour of systems such as supercapacitors, batteries, corrosion cells, and sensors. It provides insights into charge transfer, ion diffusion, reaction kinetics, and surface phenomena [2]. In EIS, a small sinusoidal AC voltage is superimposed on a DC bias, and the resulting current response is measured over a wide frequency range (typically 1 mHz - 100 kHz) [53]. The impedance, expressed as:

$$Z(\omega) = \frac{E(t)}{I(t)} \tag{3.16}$$

is a complex quantity comprising real (resistive) and imaginary (reactive) components, where ω is the angular frequency (s^{-1}). The applied potential is given by:

$$E(t) = E_{\text{app}} + \mid E_0 \mid \sin(\omega t) \tag{3.17}$$

$$I(t) = \mid I_0 \mid \sin(\omega t + \phi) \tag{3.18}$$

where $\mid E_0 \mid$ is the AC amplitude (5-10 mV) and φ is the phase angle between voltage and current.

Impedance data are commonly represented in Nyquist and Bode plots [54]. In the Nyquist plot **(Figure 3.13(a))**, the imaginary component ($-Z''$) is plotted against the real component (Z′), as defined by:

$$Z(\omega) = \mid Z \mid (\cos\,\phi - j\sin\,\phi) = Z' - jZ' \tag{3.19}$$

The x-intercept corresponds to the solution resistance (R_S), and the semicircle diameter represents the charge-transfer resistance (R_{CT}) [55,56]. The high-frequency region reflects charge-transfer processes, while the low-frequency region corresponds to ion diffusion, described by the Warburg impedance (Z_W). The characteristic reaction time constant is given by:

$$\frac{f_{\max}}{2\pi} = \frac{1}{R_{CT}C_{dl}} = \frac{1}{\tau_{\mathrm{rxn}}} \tag{3.20}$$

where C_{dl} is the double-layer capacitance.

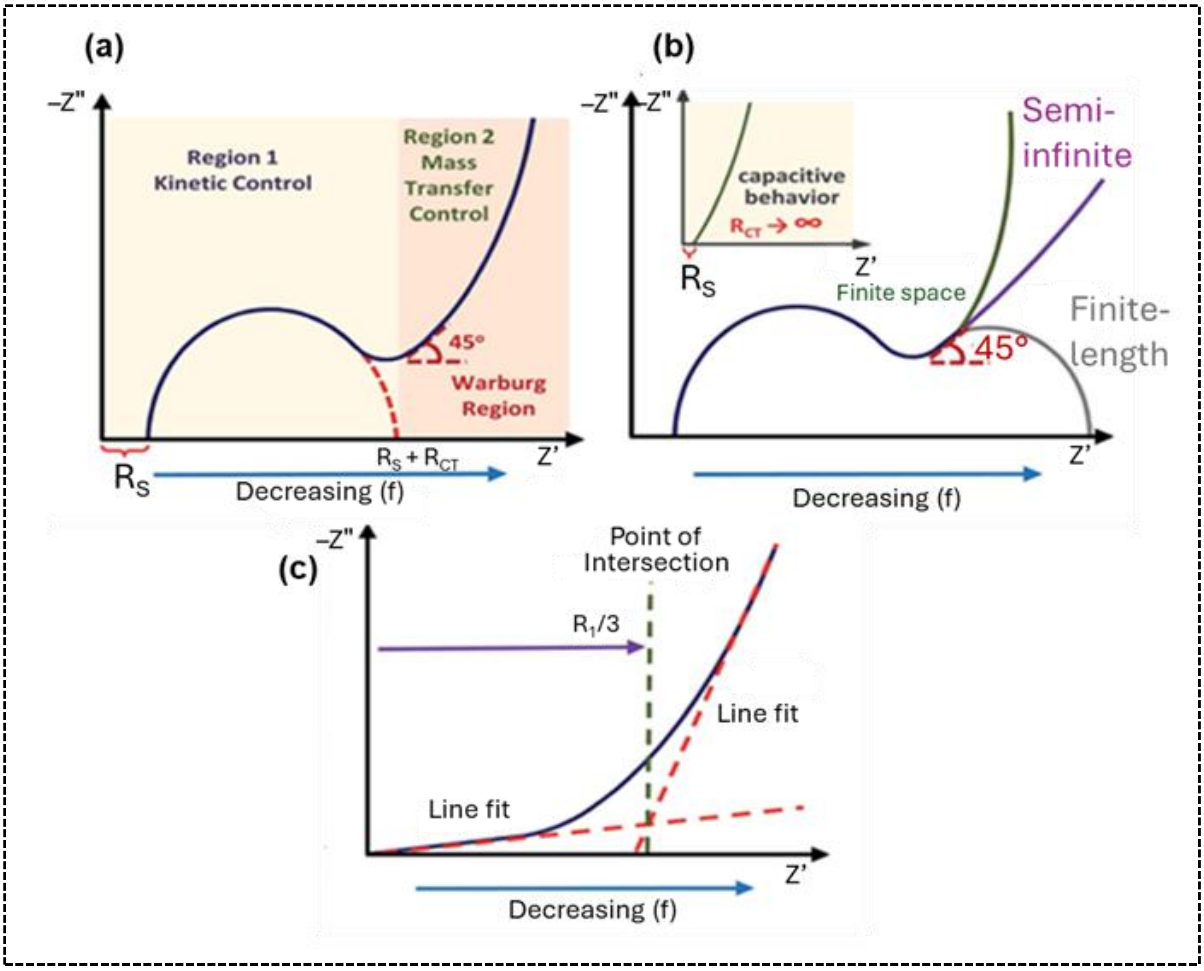

Figure 3.12. (a) Nyquist plot displaying the fundamental regions within the plot [2]. (b) The expanded Nyquist plot region 2, showing the characteristic Warburg impedances associated with various electrode materials [2]. The inset in (b) typical capacitive behaviour for capacitive materials. (c) Determination of R_Σ utilising linear fitting of the Warburg region [2]. (a-c) Reprinted with permission from Ref. [2], Copyright 2021, Royal Society of Chemistry.

At mid-frequencies, a semicircle generally appears, while at low frequencies, a 45° slope (the Warburg region) indicates semi-infinite diffusion [2][57,58]. In highly capacitive systems, the Nyquist plot becomes nearly vertical, indicative of ideal capacitive behaviour [59][60].

The total internal resistance (R_Σ) is derived from the low-frequency region (**Figure 3.12(c))** and represents the combined ionic (R_{ion}) and electronic (R_{ele}) resistances:

$$R_\Sigma = R_{\text{ion}} + R_{\text{ele}} \tag{3.21}$$

Equivalent circuit modelling enables quantitative analysis of parameters such as R_S, R_{CT}, C_{dl} (or constant phase element, CPE), and Z_W 59–63]. The inclusion of a CPE accounts for surface inhomogeneity and roughness, while inductive elements (L) may appear due to metallic leads or connectors [63,64] [65].

In Bode plots, the logarithm of impedance magnitude (|Z|) and phase angle (φ) are plotted against log frequency [54]. A phase angle near 90° indicates ideal capacitive behaviour, while values around 45° suggest pseudocapacitive processes [59]. In the magnitude plot, a slope of 1 denotes capacitive behaviour, and a slope of 0 reflects resistive behaviour [64–68].

By combining Nyquist and Bode analyses **(Figure 3.12(a-c))**, EIS provides comprehensive understanding of charge transfer, interfacial resistance, and ion diffusion dynamics, making it indispensable for the optimisation of electrochemical energy storage devices.

References

[1] L. Yan, A. Liu, R. Ma, C. Guo, X. Ding, P. Feng, D. Jia, M. Xu, L. Ai, N. Guo, L. Wang, Regulating the specific surface area and porous structure of carbon for high performance supercapacitors, Appl Surf Sci 615 (2023) 156267. https://doi.org/10.1016/j.apsusc.2022.156267.

[2] N.O. Laschuk, E.B. Easton, O. V. Zenkina, Reducing the resistance for the use of electrochemical impedance spectroscopy analysis in materials chemistry, RSC Adv 11 (2021) 27925–27936. https://doi.org/10.1039/d1ra03785d.

[3] A. Alyamani, O. Lemine, FE-SEM characterization of some nanomaterial, INTECH Open Access Publisher, Intech (2012) 463–472.

[4] G. McMahon, Analytical instrumentation: A guide to laboratory portable and miniaturized instruments, 1st ed., Wiley, Chichester, 2007.

[5] K. Akhtar, S.A. Khan, S.B. Khan, A.M. Asiri, Scanning electron microscopy: Principle and applications in nanomaterials characterization, 2018. https://doi.org/10.1007/978-3-319-92955-2_4.

[6] J.I. Goldstein, D.E. Newbury, P. Echlin, D.C. Joy, Scanning electron microscopy and x-ray microanalysis, 2nd ed., Plenum Press, New York, 1992.

[7] B. Kwiecińska, S. Pusz, B.J. Valentine, Application of electron microscopy TEM and SEM for analysis of coals, organic-rich shales and carbonaceous matter, Int J Coal Geol 211 (2019) 103203. https://doi.org/10.1016/j.coal.2019.05.010.

[8] N. Raval, R. Maheshwari, D. Kalyane, S.R. Youngren-Ortiz, M.B. Chougule, R.K. Tekade, Importance of physicochemical characterization of nanoparticles in

pharmaceutical product development, Elsevier Inc., 2018. https://doi.org/10.1016/B978-0-12-817909-3.00010-8.

[9] V.D. Hodoroaba, Energy-dispersive X-ray spectroscopy (EDS), Elsevier Inc., 2019. https://doi.org/10.1016/B978-0-12-814182-3.00021-3.

[10] M. Abd Mutalib, M.A. Rahman, M.H.D. Othman, A.F. Ismail, J. Jaafar, Scanning Electron Microscopy (SEM) and Energy-Dispersive X-Ray (EDX) Spectroscopy, Elsevier B.V., 2017. https://doi.org/10.1016/B978-0-444-63776-5.00009-7.

[11] A. (Alain) Claverie, Transmission electron microscopy in micro-nanoelectronics, (2013). http://www.123library.org/book_details/?id=62810.

[12] J.I. Goldstein, D.E. Newbury, J.R. Michael, N.W.M. Ritchie, J.H.J. Scott, D.C. Joy, Scanning electron microscopy and X-ray microanalysis, springer, 2017.

[13] Z. Luo, A practical guide to transmission electron microscopy. Volume II : Advanced microscopy, (2016). https://doi.org/10.5643/9781606509180 LK - https://UnivofPretoria.on.worldcat.org/oclc/936210021.

[14] J. Kacher, Y. Xie, S.P. Voigt, S. Zhu, H. Yuchi, J. Key, S.R. Kalidindi, In Situ Transmission Electron Microscopy: Signal processing challenges and examples, IEEE Signal Process Mag 39 (2022) 89–103. https://doi.org/10.1109/MSP.2021.3119284.

[15] Y. Jiang, Z. Zhang, W. Yuan, X. Zhang, Y. Wang, Z. Zhang, Recent advances in gas-involved in situ studies via transmission electron microscopy, Nano Res 11 (2018) 42–67. https://doi.org/10.1007/s12274-017-1645-9.

[16] M.H. Engelhard, T.C. Droubay, Y. Du, X-ray photoelectron spectroscopy applications, Encyclopedia of Spectroscopy and Spectrometry (2016) 716–724. https://doi.org/10.1016/B978-0-12-409547-2.12102-X.

[17] D.R. Baer, S. Thevuthasan, Characterization of Thin Films and Coatings, Third Edit, Elsevier Ltd., 2009. https://doi.org/10.1016/B978-0-8155-2031-3.00016-8.

[18] S. Petit, J. Madejova, Fourier Transform Infrared Spectroscopy, 2nd ed., Elsevier Ltd., 2013. https://doi.org/10.1016/B978-0-08-098259-5.00009-3.

[19] A.A. Ismail, F.R. van de Voort, J. Sedman, Chapter 4 Fourier transform infrared spectroscopy: Principles and applications, Techniques and Instrumentation in Analytical Chemistry 18 (1997) 93–139. https://doi.org/10.1016/S0167-9244(97)80013-3.

[20] W. Qi, Y. Tian, D. Lu, B. Chen, Research Progress of Applying Infrared Spectroscopy Technology for Detection of Toxic and Harmful Substances in Food, Foods 11 (2022) 930. https://doi.org/10.3390/foods11070930.

[21] A. Dutta, Fourier Transform Infrared Spectroscopy, Elsevier Inc., 2017. https://doi.org/10.1016/B978-0-323-46140-5.00004-2.

[22] M. Zhang, R. Wang, X. Wu, J. Wang, Principle, system, and applications of tip-enhanced Raman spectroscopy, Sci China Phys Mech Astron 55 (2012) 1335–1344. https://doi.org/10.1007/s11433-012-4769-7.

[23] E. Smith, G. Dent, Modern Raman spectroscopy—a practical approach, Wiley, Hoboken, 2005.

[24] R.J.H. Clark, Rayleigh, Ramsay, Rutherford and Raman-their connections with, and contributions to, the discovery of the Raman effect, Analyst 138 (2013) 729–734. https://doi.org/10.1039/c2an90124b.

[25] W. ting Wang, H. Zhang, Y. Yuan, Y. Guo, S. xin He, Research Progress of Raman Spectroscopy in Drug Analysis, AAPS PharmSciTech 19 (2018) 2921–2928. https://doi.org/10.1208/s12249-018-1135-8.

[26] W. Zhang, J. Ma, D.W. Sun, Raman spectroscopic techniques for detecting structure and quality of frozen foods: principles and applications, Crit Rev Food Sci Nutr 61 (2021) 2623–2639. https://doi.org/10.1080/10408398.2020.1828814.

[27] N. Li, N. Hussain, Z. Ding, C. Qu, Y. Li, L. Chu, H. Liu, Guidelines for Raman spectroscopy and imaging techniques in food safety analysis, Food Safety and Health 2 (2024) 221–237. https://doi.org/10.1002/fsh3.12040.

[28] A. Bishnoi, S. Kumar, N. Joshi, Wide-Angle X-ray Diffraction (WXRD), Elsevier Inc., 2017. https://doi.org/10.1016/B978-0-323-46141-2.00009-2.

[29] J. Epp, X-Ray Diffraction (XRD) Techniques for Materials Characterization, Elsevier Ltd, 2016. https://doi.org/10.1016/B978-0-08-100040-3.00004-3.

[30] Y. Shao, M.F. El-Kady, J. Sun, Y. Li, Q. Zhang, M. Zhu, H. Wang, B. Dunn, R.B. Kaner, Design and Mechanisms of Asymmetric Supercapacitors, Chem Rev 118 (2018) 9233–9280. https://doi.org/10.1021/acs.chemrev.8b00252.

[31] A. Noori, M.F. El-Kady, M.S. Rahmanifar, R.B. Kaner, M.F. Mousavi, Towards establishing standard performance metrics for batteries, supercapacitors and beyond, Chem Soc Rev 48 (2019) 1272–1341. https://doi.org/10.1039/c8cs00581h.

[32] N. Elgrishi, K.J. Rountree, B.D. McCarthy, E.S. Rountree, T.T. Eisenhart, J.L. Dempsey, A Practical Beginner’s Guide to Cyclic Voltammetry, J Chem Educ 95 (2018) 197–206. https://doi.org/10.1021/acs.jchemed.7b00361.

[33] S.Y. Attia, S.G. Mohamed, Y.F. Barakat, H.H. Hassan, W. Al Zoubi, Supercapacitor electrode materials: Addressing challenges in mechanism and charge storage, Reviews in Inorganic Chemistry 42 (2022) 53–88. https://doi.org/10.1515/revic-2020-0022.

[34] Z. Dai, C. Peng, J.H. Chae, K.C. Ng, G.Z. Chen, Cell voltage versus electrode potential range in aqueous supercapacitors, Sci Rep 5 (2015). https://doi.org/10.1038/srep09854.

[35] S. Zhang, N. Pan, Supercapacitors performance evaluation, Adv Energy Mater 5 (2015) 1–19. https://doi.org/10.1002/aenm.201401401.

[36] T. Brousse, D. Bélanger, J.W. Long, To Be or Not To Be Pseudocapacitive?, J Electrochem Soc 162 (2015) A5185–A5189. https://doi.org/10.1149/2.0201505jes.

[37] M.R. Lukatskaya, B. Dunn, Y. Gogotsi, Multidimensional materials and device architectures for future hybrid energy storage, Nat Commun 7 (2016). https://doi.org/10.1038/ncomms12647.

[38] P. Simon, Y. Gogotsi, B. Dunn, Where Do Batteries End and Supercapacitors Begin?, Science (1979) 343 (2014) 1210–1211. https://doi.org/10.1126/science.1249625.

[39] K.B. Hatzell, M. Beidaghi, J.W. Campos, C.R. Dennison, E.C. Kumbur, Y. Gogotsi, A high performance pseudocapacitive suspension electrode for the electrochemical flow capacitor, Electrochim Acta 111 (2013) 888–897. https://doi.org/10.1016/j.electacta.2013.08.095.

[40] J.B. Cook, H.S. Kim, Y. Yan, J.S. Ko, S. Robbennolt, B. Dunn, S.H. Tolbert, Mesoporous MoS2 as a Transition Metal Dichalcogenide Exhibiting Pseudocapacitive Li and Na-Ion Charge Storage, Adv Energy Mater 6 (2016) 1–12. https://doi.org/10.1002/aenm.201501937.

[41] V. Augustyn, P. Simon, B. Dunn, Pseudocapacitive oxide materials for high-rate electrochemical energy storage, Energy Environ Sci 7 (2014) 1597–1614. https://doi.org/10.1039/c3ee44164d.

[42] S. Ardizzone, G. Fregonara, S. Trasatti, “Inner” and “outer” active surface of RuO2 electrodes, Electrochim Acta 35 (1990) 263–267. https://doi.org/10.1016/0013-4686(90)85068-X.

[43] H. Yu, X. Dong, Y. Pang, Y. Wang, Y. Xia, High Power Lithium-ion Battery based on Spinel Cathode and Hard Carbon Anode, Electrochim Acta 228 (2017) 251–258. https://doi.org/10.1016/j.electacta.2017.01.096.

[44] W. Yan, J.Y. Kim, W. Xing, K.C. Donavan, T. Ayvazian, R.M. Penner, Lithographically patterned gold/manganese dioxide core/shell nanowires for high capacity, high rate, and high cyclability hybrid electrical energy storage, Chemistry of Materials 24 (2012) 2382–2390. https://doi.org/10.1021/cm3011474.

[45] H.S. Kim, J.B. Cook, H. Lin, J.S. Ko, S.H. Tolbert, V. Ozolins, B. Dunn, Oxygen vacancies enhance pseudocapacitive charge storage properties of MoO3-x, Nat Mater 16 (2017) 454–462. https://doi.org/10.1038/NMAT4810.

[46] A. Laheäär, P. Przygocki, Q. Abbas, F. Béguin, Appropriate methods for evaluating the efficiency and capacitive behavior of different types of supercapacitors, 2015. https://doi.org/10.1016/j.elecom.2015.07.022.

[47] M. Jana, J.S. Kumar, P. Khanra, P. Samanta, H. Koo, N.C. Murmu, T. Kuila, Superior performance of asymmetric supercapacitor based on reduced graphene oxide--manganese carbonate as positive and sono-chemically reduced graphene oxide as negative electrode materials, J Power Sources 303 (2016) 222–233.

[48] B. Akinwolemiwa, C. Peng, G.Z. Chen, Redox Electrolytes in Supercapacitors, J Electrochem Soc 162 (2015) A5054–A5059. https://doi.org/10.1149/2.0111505jes.

[49] K.O. Oyedotun, M.J. Madito, A. Bello, D.Y. Momodu, A.A. Mirghni, N. Manyala, Investigation of graphene oxide nanogel and carbon nanorods as electrode for electrochemical supercapacitor, Electrochim Acta (2017). https://doi.org/10.1016/j.electacta.2017.05.150.

[50] G. Godillot, L. Guerlou-Demourgues, P.-L. Taberna, P. Simon, C. Delmas, Original Conductive Nano-Co3O4 Investigated as Electrode Material for Hybrid Supercapacitors, Electrochemical and Solid-State Letters 14 (2011) A139. https://doi.org/10.1149/1.3609259.

[51] P. Simon, Y. Gogotsi, Materials for electrochemical capacitors, 7 (2008) 845–854. https://doi.org/10.1038/nmat2297.

[52] M. ITAGAKI, S. SUZUKI, I. SHITANDA, K. WATANABE, Electrochemical Impedance and Complex Capacitance to Interpret Electrochemical Capacitor, Electrochemistry 75 (2007) 649–655. https://doi.org/10.5796/electrochemistry.75.649.

[53] R. Negroiu, P. Svasta, C. Ionescu, A. Vasile, Investigation of Supercapacitor's Impedance Based on Spectroscopic Measurements, 1st PCNS Passive Components Networking Days 1 (2017) 56–62.

[54] L. Yuan, X. Lu, X. Xiao, T. Zhai, J. Dai, F. Zhang, B. Hu, X. Wang, L. Gong, J. Chen, C. Hu, Y. Tong, J. Zhou, Z.L. Wang, Flexible Solid-State Supercapacitors Based on Carbon Nanoparticles/MnO 2 Nanorods Hybrid Structure, ACS Nano 6 (2012) 656–661. https://doi.org/10.1021/nn2041279.

[55] T. Ye, Y. Sun, X. Zhao, B. Lin, H. Yang, X. Zhang, L. Guo, Long-term-stable, solution-processable, electrochromic carbon nanotubes/polymer composite for smart supercapacitor with wide working potential window, J Mater Chem A Mater 6 (2018) 18994–19003. https://doi.org/10.1039/C8TA04465A.

[56] T. Dhandayuthapani, R. Sivakumar, R. Ilangovan, C. Gopalakrishnan, C. Sanjeeviraja, A. Sivanantharaja, R. Hari Krishna, Efficient electrochromic performance of anatase TiO2 thin films prepared by nebulized spray deposition method, Journal of Solid State Electrochemistry 22 (2018) 1825–1838. https://doi.org/10.1007/s10008-018-3888-0.

[57] R. Giannuzzi, M. Manca, L. De Marco, M.R. Belviso, A. Cannavale, T. Sibillano, C. Giannini, P.D. Cozzoli, G. Gigli, Ultrathin TiO 2 (B) Nanorods with Superior Lithium-Ion Storage Performance, ACS Appl Mater Interfaces 6 (2014) 1933–1943. https://doi.org/10.1021/am4049833.

[58] V. Kumar, K. Krishnamoorthy, P. Pazhamalai, Electrochimica Acta Electrodeposited molybdenum selenide sheets on nickel foam as a binder-free electrode for supercapacitor application, Electrochim Acta 265 (2018) 514–522. https://doi.org/10.1016/j.electacta.2018.01.075.

[59] R. Acheampong, R. Alipour Moghadam Esfahani, R.B. Moghaddam, E.B. Easton, Communication—An Organosilane-Based Fuel Cell Ionomer that Mitigates Carbon Corrosion, J Electrochem Soc 167 (2020) 044516. https://doi.org/10.1149/1945-7111/ab7a0a.

[60] G. Piłatowicz, A. Marongiu, J. Drillkens, P. Sinhuber, D.U. Sauer, A critical overview of definitions and determination techniques of the internal resistance using lithium-ion, lead-acid, nickel metal-hydride batteries and electrochemical double-layer

capacitors as examples, J Power Sources 296 (2015) 365–376. https://doi.org/10.1016/j.jpowsour.2015.07.073.

[61] A.R.C. Bredar, A.L. Chown, A.R. Burton, B.H. Farnum, Electrochemical Impedance Spectroscopy of Metal Oxide Electrodes for Energy Applications, (2020). https://doi.org/10.1021/acsaem.9b01965.

[62] S. Holm, T. Holm, Ø.G. Martinsen, Simple circuit equivalents for the constant phase element, PLoS One 16 (2021) 1–12. https://doi.org/10.1371/journal.pone.0248786.

[63] A. Lasia, The Origin of the Constant Phase Element, Journal of Physical Chemistry Letters 13 (2022) 580–589. https://doi.org/10.1021/acs.jpclett.1c03782.

[64] J.K. Bhattarai, Y.H. Tan, B. Pandey, K. Fujikawa, A. V Demchenko, K.J. Stine, Electrochemical impedance spectroscopy study of Concanavalin A binding to self-assembled monolayers of mannosides on gold wire electrodes, Journal of Electroanalytical Chemistry 780 (2016) 311–320. https://doi.org/10.1016/j.jelechem.2016.09.045.

[65] D.A. Links, Electrochemical investigations on stability and protonation behavior of pyridine-terminated aromatic self-assembled monolayers, (2011) 15530–15538. https://doi.org/10.1039/c1cp21469a.

[66] L. Manjakkal, E. Djurdjic, K. Cvejin, J. Kulawik, K. Zaraska, D. Szwagierczak, Electrochimica Acta Electrochemical Impedance Spectroscopic Analysis of RuO 2 Based Thick Film pH Sensors, Electrochim Acta 168 (2015) 246–255. https://doi.org/10.1016/j.electacta.2015.04.048.

[67] A.R.C. Bredar, A.L. Chown, A.R. Burton, B.H. Farnum, Electrochemical Impedance Spectroscopy of Metal Oxide Electrodes for Energy Applications, ACS Appl Energy Mater 3 (2020) 66–98. https://doi.org/10.1021/acsaem.9b01965.

[68] B.P.G. Silva, D.Z. de Florio, S. Brochsztain, Characterization of a Perylenediimide Self-Assembled Monolayer on Indium Tin Oxide Electrodes Using Electrochemical Impedance Spectroscopy, The Journal of Physical Chemistry C 118 (2014) 4103–4112. https://doi.org/10.1021/jp409416b.

[69] D. Nkosi, J. Pillay, K.I. Ozoemena, K. Nouneh, M. Oyama, Heterogeneous electron transfer kinetics and electrocatalytic behaviour of mixed self-assembled ferrocenes and SWCNT layers, Phys. Chem. Chem. Phys. 12 (2010) 604–613. https://doi.org/10.1039/B918754E.

[70] J. Zhang, H. Feng, Q. Qin, G. Zhang, Y. Cui, Z. Chai, W. Zheng, Interior design of three-dimensional CuO ordered architectures with enhanced performance for supercapacitors, J Mater Chem A Mater 4 (2016) 6357–6367. https://doi.org/10.1039/C6TA00397D.

CHAPTER 4

EXPERIMENTAL METHODS

4.1 Introduction

This chapter outlines the experimental methods used to synthesize, characterize, and evaluate the as-synthesized material for supercapacitor applications. It begins with a description of the materials and reagents used, followed by the preparation of electrochemically exfoliated graphene (EEG) in powder and thin films, the synthesis of pristine nickel-manganese phosphate ($NiMn(PO_4)_2$), and the fabrication of the nickel-manganese phosphate/electrochemically exfoliated graphene ($NiMn(PO_4)_2$/EEG) nanocomposite. The chapter then details the microscopic and spectroscopic techniques employed to analyse the structural and compositional properties of the materials. Procedures for electrode preparation and the electrochemical setup for performance testing are also presented. This chapter provides a concise framework of the experimental approach underlying the results discussed in this study.

4.2 Materials and Reagents

All chemicals used in this study were of analytical grade and obtained from Merck (South Africa). The reagents included ethanol, carbon back, N-methyl-2-pyrrolidone (NMP), polyvinylidene fluoride (PVDF), and potassium hydroxide (KOH). Sulfuric acid (98 wt%H_2SO_4) and phosphoric acid (85 wt% H_3PO_4) served as electrolyte and phosphate sources, respectively. Manganese (II) sulphate monohydrate ($MnSO_4$ H_2O, 98%) and nitrate hexahydrate [$Ni(NO_3)_2$ $6H_2O$, 98%] were employed as metal precursors for the synthesis of Ni-Mn phosphate. Disodium hydrogen phosphate (Na_2HPO_4 98%) was used as the anionic phosphate source. All reagents were used as received without any further purification

4.3 Preparation of Electrochemically Exfoliated Graphene (EEG)

The electrochemical exfoliation of graphite into electrochemically exfoliated graphene (EEG) was carried out using a two-step intercalation-exfoliation process, as illustrated in **Figure 4.1**. In this procedure, a graphite foil (10 cm^2, 0.5 mm thick, Alfa Aesar) served as the working electrode, while a stainless-steel plate was used as the counter electrode. Both electrodes were connected to a direct current (DC) power supply (0 - 30 V, 3 A). During the intercalation stage, the graphite foil was immersed in 100 mL of a mixed acid electrolyte comprising concentrated sulfuric acid (98 wt% H_2SO_4) and phosphoric acid (85 wt% H_3PO_4) and subjected to a constant current density of 20 mA cm-2 for 800 s. Acid mixtures with different volumetric ratios of H_2SO_4:H_3PO_4 (100:0, 95:5, and 90:10) were prepared to optimize the intercalation conditions. In the subsequent exfoliation step, the intercalated graphite was transferred into an aqueous electrolyte containing 0.1 M ammonium sulfate ($(NH_4)_2SO_4$) and exfoliated under a constant voltage of 10 V, corresponding to an average current density of approximately 34 mA cm^{-2} for 800 s. The exfoliated product was filtered through a 0.45 μm cellulose membrane and repeatedly washed with deionized water until a neutral pH was achieved. The resulting dispersion was ultrasonicated for 15 minutes and allowed to stand overnight. The suspension was then centrifuged at 3000 rpm for 10 minutes to separate the few-layer graphene from residual graphite. The supernatant was vacuum-filtered, washed with deionized water, and subsequently freeze-dried to yield the final EEG powder. A free-standing EEG film (~20 μm thick) was fabricated by redispersing the EEG powder in deionized water, ultrasonically treating for 5 minutes, and vacuum-filtering through a 0.45 μm cellulose membrane.

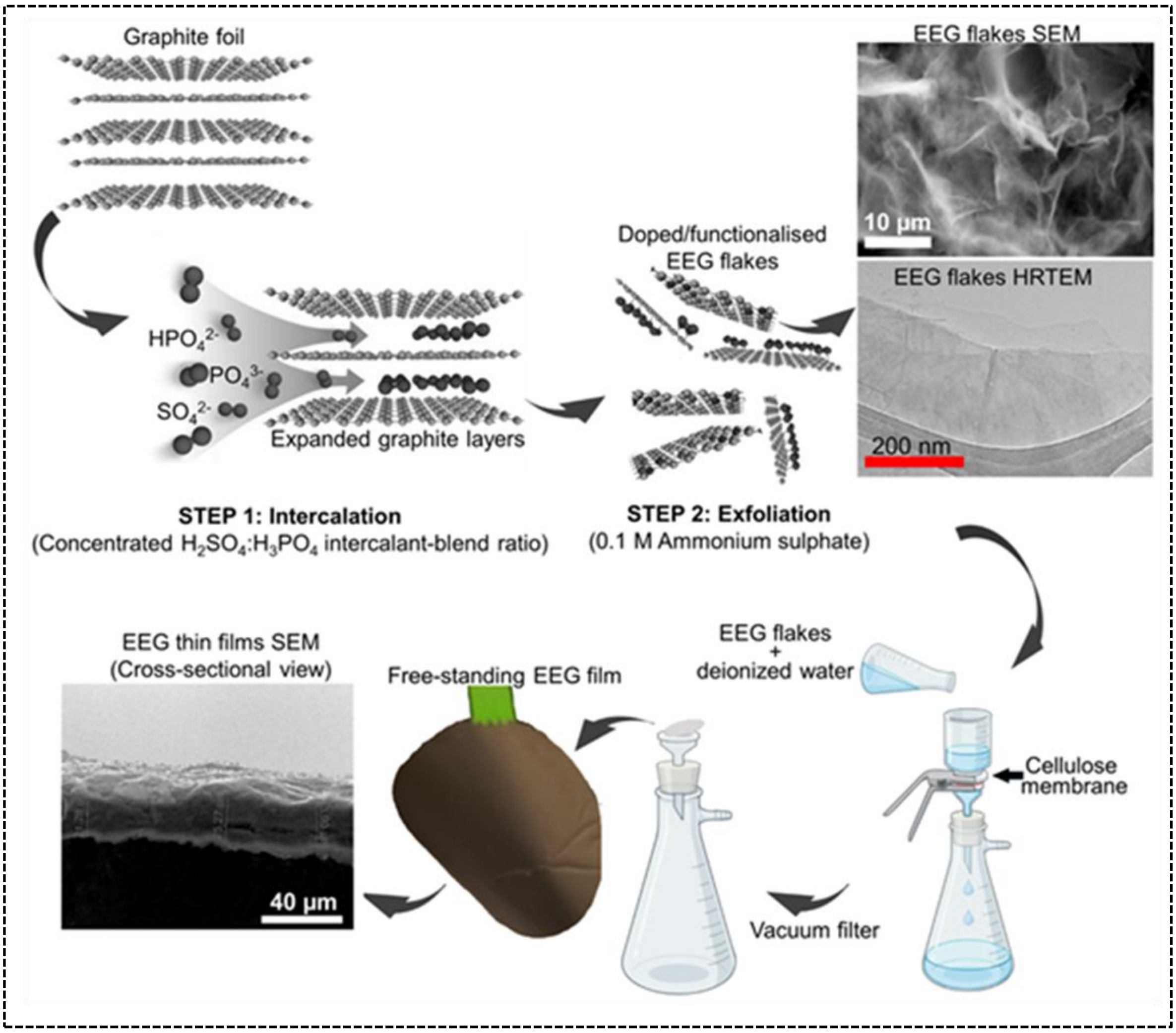

Figure 4.1: Schematic diagram illustrating the synthesis of EEG film through a two-step intercalation-exfoliation process using H_2SO_4/H_3PO_4 acid blends with ratios of 100:0, 95:5, and 90:10, and an intercalation duration of 800 s.

4.4 Preparation of $NiMn(PO_4)_2$/EEG Nanocomposite

The nickel-manganese phosphate/electrochemically exfoliated graphene ($NiMn(PO_4)_2$/EEG) composite was synthesized via a two-step hydrothermal procedure, as illustrated in **Figure 4.2**. In the first step, 0.60 g of nickel (II) nitrate hexahydrate [$Ni(NO_3)_2 \cdot 6H_2O$] and 0.50 g of manganese (II) sulfate monohydrate ($MnSO_4 \cdot H_2O$) were dissolved in 50 mL of deionized (DI) water under continuous stirring to form a homogeneous metal precursor solution. This solution was then added dropwise to 20 mL of DI water containing 0.30 g of disodium hydrogen phosphate (Na_2HPO_4) and stirred for 1 hour to ensure complete reaction and nucleation of phosphate species. In the second step, 50 mg of electrochemically exfoliated graphene (EEG) was dispersed in 30 mL of DI water by ultrasonication to achieve a uniform suspension. The EEG dispersion was subsequently mixed with 70 mL of the previously prepared metal-phosphate precursor solution (in a 70:30 v/v ratio) and stirred for an additional hour to promote homogeneous interaction between the graphene sheets and phosphate precursors. The resulting mixture was transferred into a 100 mL Teflon-lined stainless-steel autoclave and subjected to hydrothermal treatment at 200 °C for 24 hours. After naturally cooling to room temperature, the obtained product was filtered, washed repeatedly with deionized water and methanol to remove residual impurities, and dried at 60 °C overnight to yield the $NiMn(PO_4)_2$/EEG composite. The pristine $NiMn(PO_4)_2$ was prepared following the same synthesis procedure as the composite, with the exclusion of the EEG component.

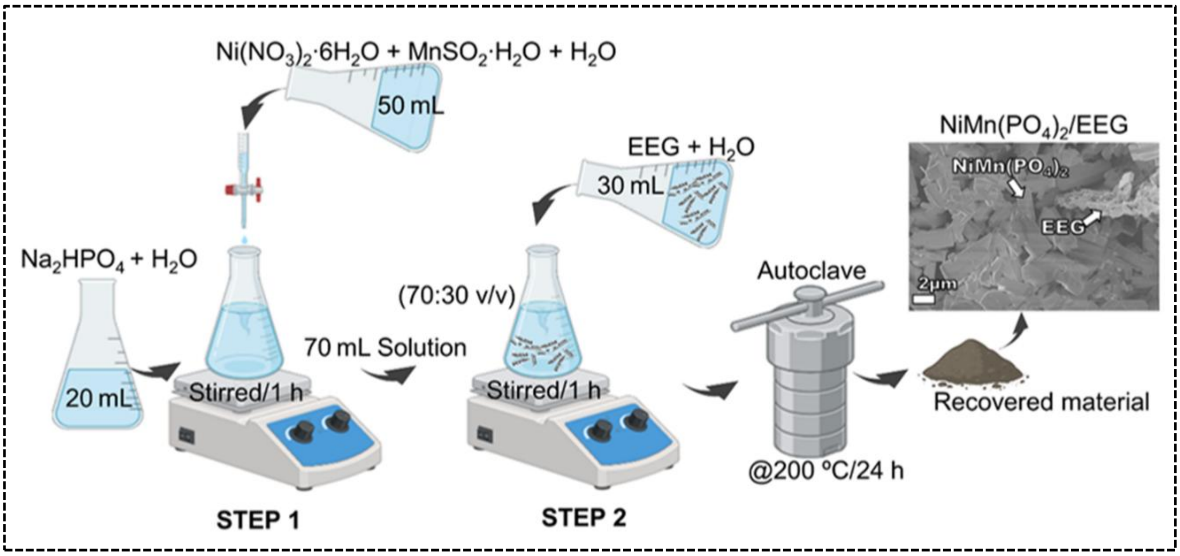

Figure 4.2: Schematic representation of the hydrothermal synthesis route for the $NiMn(PO_4)_2$/EEG composite.

4.5 Microscopic and Spectroscopic Characteristics

4.5.1 Scanning Electron Microscopy-Energy Dispersive Characterisation

The morphological and structural features of the synthesized material were examined using a JEOL IT300 Scanning Electron Microscope (SEM) equipped with an Energy Dispersive Spectrometer (EDS). Data acquisition and analysis were performed using Aztec software. For imaging, the samples were mounted on aluminum stubs using carbon tape and coated with a thin gold layer (~5 nm) to enhance surface conductivity and image resolution.

4.5.2 High-Resolution Transmission Electron Microscopy

The morphological and structural properties of the nanocomposites were examined using a JEOL JEM-2100 Transmission Electron Microscope (TEM) operated at an accelerating voltage of 200 kV. For sample preparation, the as-prepared material was dispersed in ethanol and ultrasonicated for 20 minutes to achieve a uniform suspension. A drop of the dispersion was then deposited onto a carbon-coated copper grid and dried prior to analysis.

4.5.3 X-ray Diffraction

The crystallographic structure of the synthesized nanocomposites was analysed using a Rigaku Smart-Lab X-ray Diffractometer. The measurements were carried out using Cu Kα radiation ($\lambda = 1.54060$ Å) generated from a 3 kW sealed X-ray tube. Diffraction patterns were recorded over a 2θ range of 20 - 70°, and the obtained phases were identified and matched against standard reference patterns from the Inorganic Crystal Structure Database (ICSD).

4.5.4 Fourier Transform Infrared Spectroscopy

In this study, FTIR was used to identify the functional groups and confirm chemical bonding in $NiMn(PO_4)_2$, EEG, and $NiMn(PO_4)_2$/EEG composites. Spectra were recorded using Perkin Elmer Frontier FTIR spectrometer within the 4000 - 400 cm^{-1} wavenumber range, with samples prepared using the KBr pellet method.

4.5.5 Raman Spectroscopy

Raman spectroscopy was employed to analyse the structural characteristics, defect nature, and overall quality of the synthesized nanocomposites. The measurements were carried out using a WiTec Alpha 300RA confocal Raman microscope with an excitation wavelength of 532 nm at a low laser power of 4 mW to minimize sample heating. Each spectrum was recorded for 60 seconds and accumulated 50 times to ensure a high signal to noise and signal to background ratio. The scans were performed over a wavenumber range of 0 - 4000 cm^{-1}. The laser spot size was approximately 500 nm, with a spectral resolution of about 1 cm^{-1}. Raman mapping was performed over 100 × 100 μm^2 areas, consisting of 400 points per line and 400 lines per image, using an integration time of 0.25 s per point.

4.5.6 X-ray Photoelectron Spectroscopy

X-ray Photoelectron Spectroscopy is a highly sensitive surface analysis technique widely applied in chemistry and physics, including microelectronics, catalysis, and materials science. It can detect all elements except hydrogen and helium, with a detection limit of about 0.1% of a monolayer, providing detailed information on the elemental composition, oxidation states, and electronic structure of materials in a largely non-destructive manner.

In this study, XPS was employed to determine the surface elemental composition and chemical states of the EEG samples. The analyses were conducted using a Thermo-Scientific ESCALAB 250Xi spectrometer equipped with a monochromatic Al Kα X-ray source (1486.7 eV, 300 W) and an X-ray spot size of 900 μm. Survey and high-resolution scans were recorded at pass energies of 100 eV and 20 eV, respectively. Detailed scans were acquired at lower step-size intervals and reduced pulse energy to enhance spectral resolution and analytical precision.

4.6 Electrodes Preparation

The fabrication of electrodes was carried out as follows, Commercial nickel foam (1.0 cm × 0.5 cm) was first cleaned to remove surface oxides and impurities. It was immersed in 0.1 M HCl and ultrasonicated for 15 minutes to eliminate the nickel oxide layer, followed by ultrasonic cleaning in ethanol for another 15 minutes. Finally, the foam was rinsed in deionized water under ultrasonication for 15 minutes, then dried in an oven at 80 °C overnight.

The working electrode was prepared using a mixture comprising 80 wt% as-prepared material, 10 wt % polyvinylidene fluoride (PVDF) as a binder, and 10 wt% carbon black (CB) as a conductive additive, as illustrated in **Figure 4.3**. PVDF was chosen for its excellent electrochemical stability and mechanical resilience during charge-discharge cycling, while carbon black enhanced electrical conductivity within the electrode matrix.

The required amount of the active material was accurately weighed and ground with a mortar and pestle for approximately 45 minutes to ensure homogeneity. N-methyl-2-pyrrolidone (NMP) was then added gradually to form a uniform slurry, which was coated onto the pretreated nickel foam (geometric area: 1 cm^2). The coated electrodes were subsequently dried in an oven at 60 °C overnight to remove residual solvent and achieve proper adhesion of the active material. The mass loading of the active material on each electrode was maintained in the range of approximately 2-3 mg.

Moreover, for electrochemical performance analysis of free-standing EEG thin films, working electrodes were prepared by cutting EEG thin films, graphite foil, and membrane filters into 1×2 cm^2 pieces, with a 1×1 cm^2 area exposed to the electrolyte during testing. The corresponding active material masses were 0.5 mg for the EEG thin films, 43.6 mg for the graphite foil, and 8.0 mg for the membrane filter.

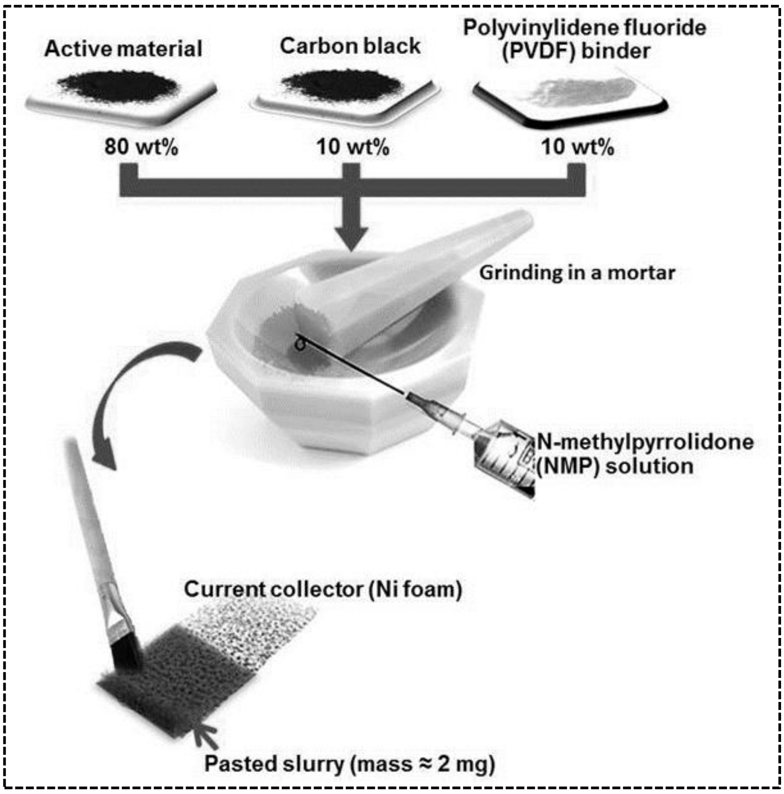

Figure 4.3. Schematic illustration of the coating process of the $NiMn(PO_4)_2$/EEG nanocomposite slurry onto the nickel foam substrate.

4.7 Electrochemical Characterisation

Electrochemical measurements were performed using a three-electrode configuration within a potential window of 0.0 - 0.45 V vs. Ag/AgCl. Cyclic voltammetry (CV) was conducted at scan rates ranging from 5 to 100 mVs^{-1}, while galvanostatic charge-discharge (GCD) tests were carried out at current densities between 0 and 10 $A\ g^{-1}$. Electrochemical impedance spectroscopy (EIS) measurements were recorded in the frequency range of 100 kHz to 0.01 Hz at open-circuit potential to evaluate charge transfer resistance and ion diffusion behavior.

To further assess device-level performance, the $NiMn(PO_4)_2$/50 mg EEG composite electrode was assembled into a two-electrode asymmetric configuration using a Swagelok-type cell with

1 M KOH aqueous electrolyte. In this setup, the NiMn$(PO_4)_2$/50 mg EEG served as the positive electrode, while activated carbon (AC) acted as the negative electrode, separated by a microfiber glass filter. EIS analysis for the assembled device was performed across a frequency range of 100 kHz to 10 mHz at open-circuit potential using a sinusoidal perturbation amplitude of 10 mV. The resulting spectra were analyzed using EC-Lab V11.43 software with Z-fit for impedance fitting and equivalent circuit modelling.

CHAPTER 5

ELECTROCHEMICALLY EXFOLIATED GRAPHENE THIN FILMS

5.1 Introduction

Carbon-based materials including graphene, reduced graphene oxide (rGO), carbon nanotubes (CNTs), activated carbon (AC), carbon fibres, and porous carbons are widely employed as electrode materials because of their high electrical conductivity, large specific surface area, and structural stability, all of which contribute to enhanced electrochemical performance and cycling durability [1]. Among these materials, graphene stands out due to its exceptional charge carrier mobility (~230 000 cm^2 V^{-1} s^{-1}), high thermal conductivity (3 000 - 5 000 W m^{-1} K^{-1}), and theoretical surface area of 2 630 m^2 g^{-1} ^{1} [1–3]. However, pristine graphene delivers limited capacitance, as its charge storage is dominated by electric double-layer (EDL) mechanisms, which constrain its energy density [4].

Heteroatom doping using elements such as nitrogen (N), phosphorus (P), and sulphur (S) is an effective strategy for enhancing graphene's electrochemical behaviour by introducing additional active sites and improving surface wettability and electron transfer [5]. For instance, N-doped graphene often exhibits improved conductivity and capacitive response due to the presence of graphitic and pyridinic nitrogen species [6].

Electrochemical exfoliation has emerged as a scalable, efficient, and environmentally benign route for producing electrochemically exfoliated graphene (EEG) and its doped derivatives [7]. This method yields few-layer graphene with high conductivity and good structural integrity using mild electrolyte conditions [7,8]. Structural and electronic features of the resulting

This chapter is published as: T. Kgwadibane et al., Diam. Relat. Mater. 160 (2025) 113058.

materials are commonly evaluated using Raman spectroscopy, which provides key insights into defect density, doping levels, and lattice disorder through characteristic D, G, 2D, and D′ bands [9] [10–12].

In this study, a simple and effective approach was developed to fabricate freestanding heteroatom-doped EEG thin films. The films were doped with N, P, and S to modulate their electronic structure, enhance charge carrier concentration, and improve electrical conductivity through controlled Fermi-level tuning. Their structural, electronic, and electrochemical properties were systematically examined using Raman spectroscopy and electrochemical analysis. The findings demonstrate how heteroatom doping influences Fermi-level position, charge transport, and mechanical behaviour, providing valuable insight into the rational design of carbon-based electrodes for high-performance energy storage, sensing, and catalytic applications.

5.2 Results and discussion

5.2.1 Structural and electronic properties

Figure 5.1 presents SEM images illustrating the nanosheet-like morphology characteristic of electrochemically exfoliated graphene (EEG). The surface evolution is clearly observed when comparing the pristine graphite foil **(Figure 5.1(a))**, which shows a flat and compact structure, with the EEG films **(Figure 5.1(b-d))**, which exhibit a porous network of interconnected nanosheets. This pronounced contrast between the dense graphite surface and the highly porous EEG architecture provides clear evidence of successful layer separation and effective exfoliation during the synthesis process.

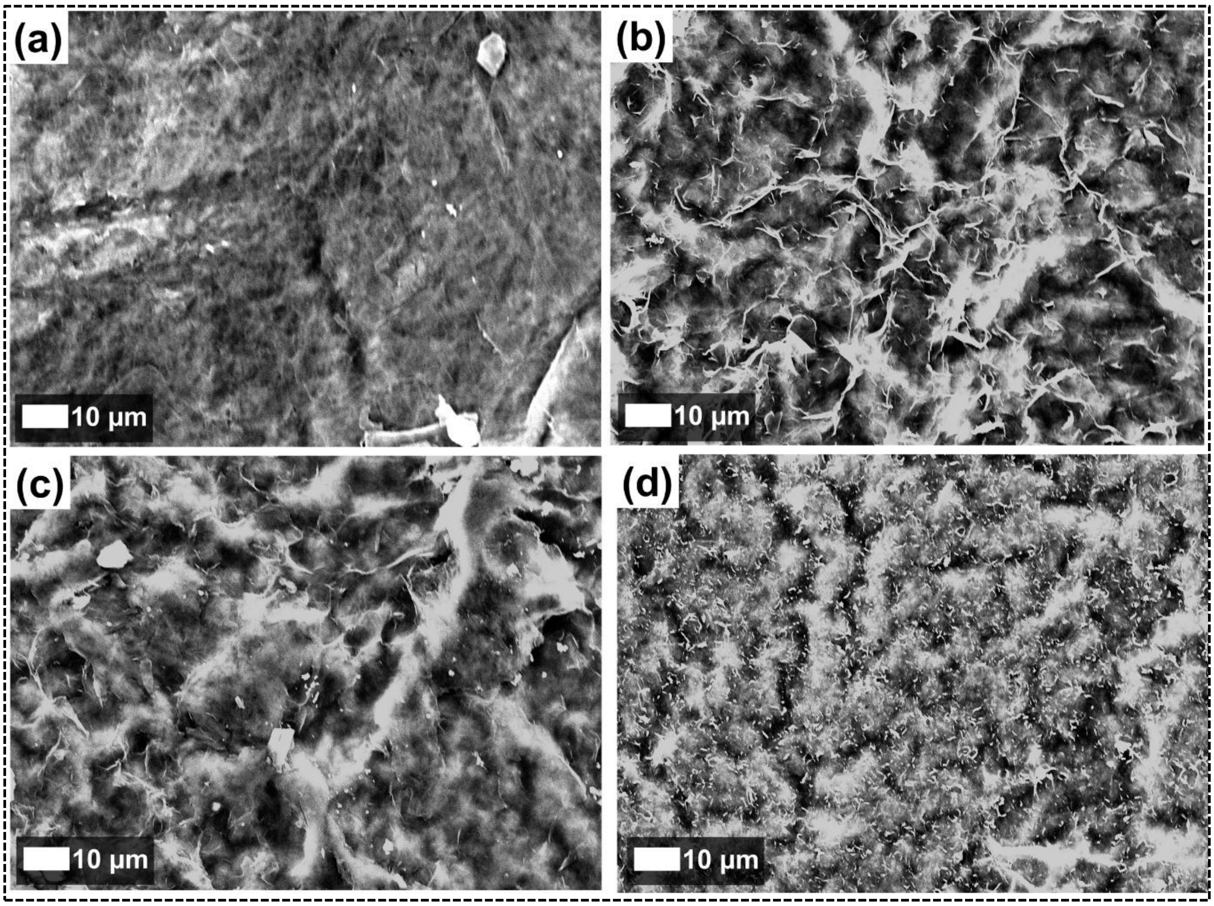

Figure 5.1 SEM images of (a) graphite foil, and EEG samples prepared using H_2SO_4:H_3PO_4 concentrated acid intercalant blends of (b) 100:0, (c) 95:5, and (d) 90:10, with an intercalation time of 800 s.

Complementary insights into the surface topography are provided by the AFM images in **Figure 5.2.** The unexfoliated graphite foil **(Figure 5.2(a))** shows an average surface roughness of 24.5 nm, substantially lower than that of the EEG films **(Figures 5.2(b-d))**, which display roughness values ranging from 60.4 to 78.8 nm depending on the acid composition used during synthesis. Specifically, the film synthesized with 100% H_2SO_4 exhibits a roughness of 78.8 nm **(Figure 5.2(b))**, while that prepared with 95% H_2SO_4 and 5% H_3PO_4 shows a similar value of 78.4 nm **(Figure 5.2(c))**. Increasing the H_3PO_4 content to 10% (90% H_2SO_4 and 10% H_3PO_4) results in a smoother surface with an average roughness of 60.4 nm **(Figure 5.2(d))**. This progressive decrease in surface roughness with higher phosphoric acid content reflects the influence of the mixed-acid intercalant system on exfoliation behaviour. The lower oxidative potential of the H_2SO_4/H_3PO_4 mixture enables more controlled intercalation and moderates the reactivity of sulphuric acid. As a result, excessive oxidation is suppressed, allowing for uniform layer expansion and less destructive exfoliation. Consequently, larger graphene flakes with fewer layers are produced [13], which in turn enhances film uniformity during deposition and reduces overall surface roughness.

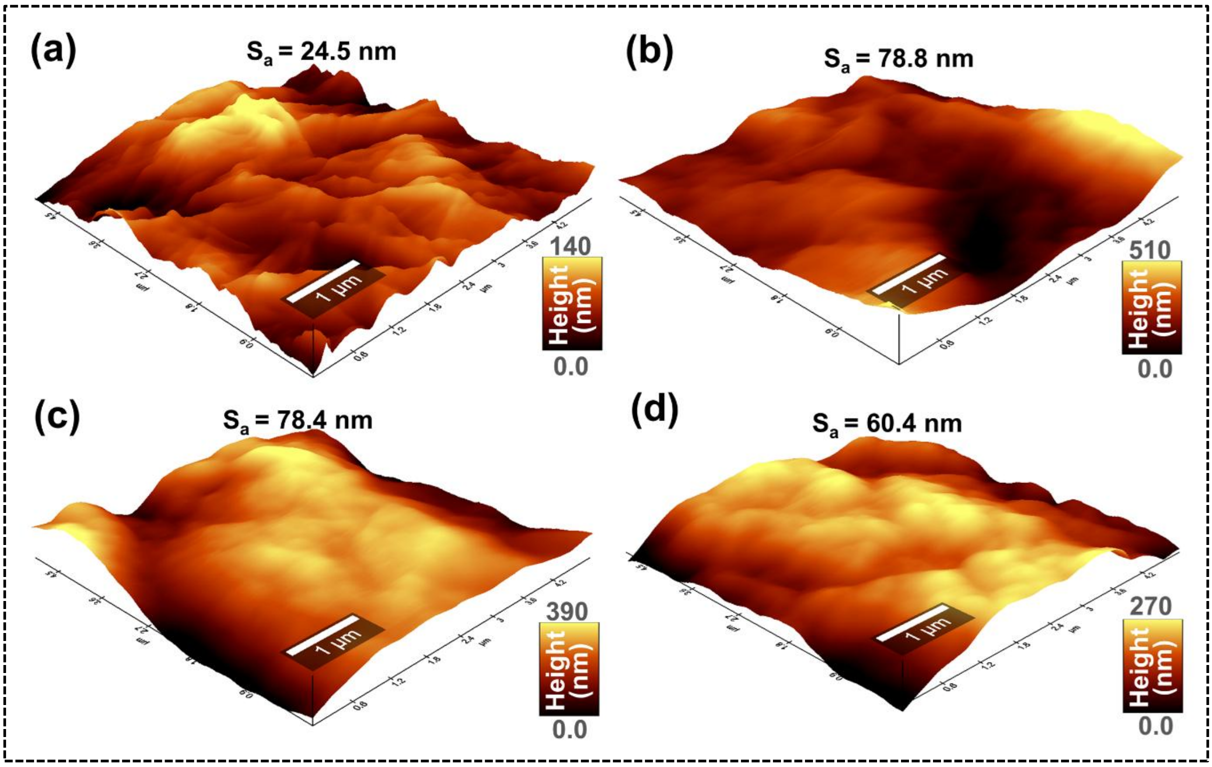

Figure 5.2 AFM images of (a) graphite foil, and EEG samples prepared using H_2SO_4:H_3PO_4 concentrated acid intercalant blends of (b) 100:0, (c) 95:5, and (d) 90:10, with an intercalation time of 800 s.

Building upon the morphological and topographical characterization, the elemental composition and doping behaviour of the EEG films were analysed using X-ray photoelectron spectroscopy (XPS), as shown in **Figure 5.3(a)**. The wide-scan XPS spectra, collected from multiple regions of each sample synthesized with H_2SO_4:H_3PO_4 ratios of 100:0, 95:5, and 90:10 (at an intercalation time of 800 s), confirm the presence of carbon, oxygen, nitrogen, sulphur, and phosphorus. The inset table in **Figure 5.3(a)** presents the average fractional elemental compositions calculated from several analysed regions per sample. Carbon and oxygen are the predominant elements, while nitrogen, sulphur, and phosphorus occur in lower concentrations corresponding to dopant levels. As the phosphoric acid content increases, the dopant concentrations of nitrogen, sulphur, and phosphorus rise, accompanied by a noticeable reduction in oxygen content. This compositional trend supports the morphological observations indicating that higher phosphoric acid content mitigates over-oxidation and promotes more uniform exfoliation, resulting in larger, less defective graphene flakes. Moreover, literature reports suggest that heteroatom incorporation into the EEG framework enhances electrical conductivity, largely due to the presence of quaternary nitrogen, and improves thermal stability through phosphorus-containing functional groups [13].

To further elucidate the surface chemical states, high-resolution XPS spectra were analysed. The deconvoluted C 1s spectrum reveals three distinct chemical states at binding energies of 284.6, 285.8, and 288.2 eV, corresponding to C=C (sp^2 graphitic carbon), C-O (epoxide/hydroxyl), and C=O (carbonyl) functional groups, respectively [14,15]. The asymmetric O 1s peak can be deconvoluted into two components at binding energies of 531.5 and 533.1 eV, attributed to C=O and C-O bonding environments, respectively, consistent with the presence of oxygen-containing functional groups on the carbon surface [15,16].

As shown in the **Figure 5.3(d)**, the S 2p spectrum displays two characteristic peaks at binding energies of approximately 163.9 eV and 162.7 eV, corresponding to S $2p_{1/2}$ and S $2p_{3/2}$ spin orbit components, respectively. The binding energy positions are characteristic of S^{2-} or low-valence sulfur species (S^{2+}) bonded to the carbon framework [17]. The spin orbit splitting of ~1.2 eV is consistent with the expected doublet separation for sulfur 2p components [17]. Collectively, these XPS results confirm the successful incorporation of sulfur and phosphorus onto the graphene flakes.

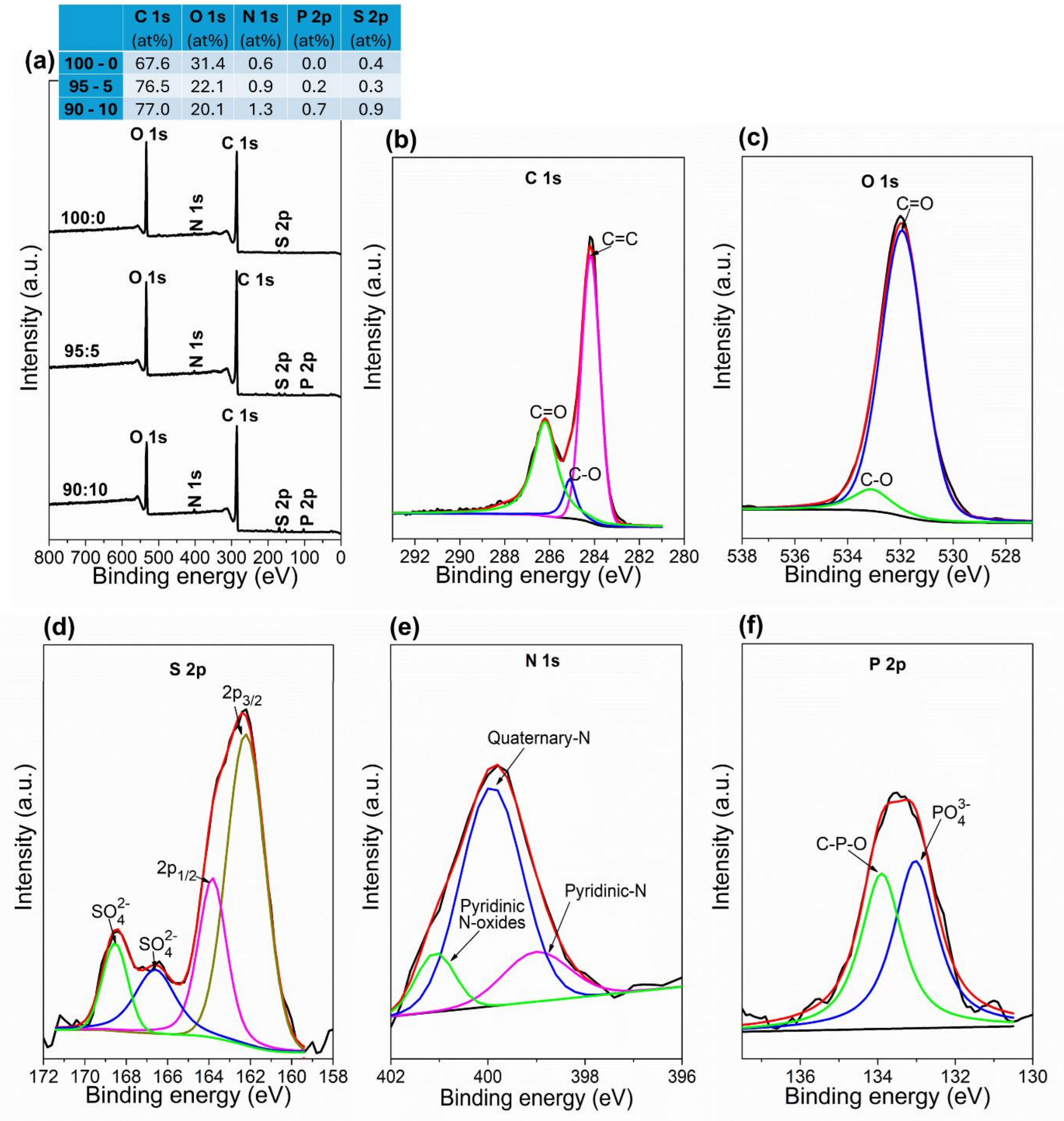

	C 1s (at%)	O 1s (at%)	N 1s (at%)	P 2p (at%)	S 2p (at%)
100 - 0	67.6	31.4	0.6	0.0	0.4
95 - 5	76.5	22.1	0.9	0.2	0.3
90 - 10	77.0	20.1	1.3	0.7	0.9

Figure 5.3 (a) Wide-scan XPS spectra of EEG samples prepared with H_2SO_4:H_3PO_4 intercalant ratios of 100:0, 95:5, and 90:10 at an intercalation time of 800 s, showing the presence of carbon, oxygen, nitrogen, sulfur, and phosphorus elements. The inset table summarizes the relative elemental (fractional) compositions of the samples. (b-f) High-resolution XPS core-level spectra of the EEG film prepared with a 90:10 H_2SO_4:H_3PO_4 ratio and an intercalation time of 800 s.

Raman spectroscopy and imaging were further employed to examine the structural order and defect characteristics of the EEG films. A total of 160,000 Raman spectra were collected from a 100 × 100 μm^2 area for both the unexfoliated graphite foil and EEG films. The averaged spectra, shown in **Figure 5.4**, display three distinct bands typical of graphitic materials: the D band at ~1350 cm^{-1}, the G band at ~1580 cm^{-1}, and the 2D band at ~2700 cm^{-1} [13]. The G band arises from the stretching of sp^2-hybridized C-C bonds in aromatic rings and corresponds to the longitudinal optical (LO) and transverse optical (TO) phonon modes with E_{2g} symmetry at the Γ point [14,15]. According to Raman selection rules, the G band originates from first-order Raman scattering, whereas the D and 2D bands are associated with double-resonance (DR) or triple-resonance (TR) processes involving one or two phonons [16–18]. The D band requires the presence of defects to activate one-phonon DR scattering, while the 2D band arises from a two-phonon DR process that does not require defects.

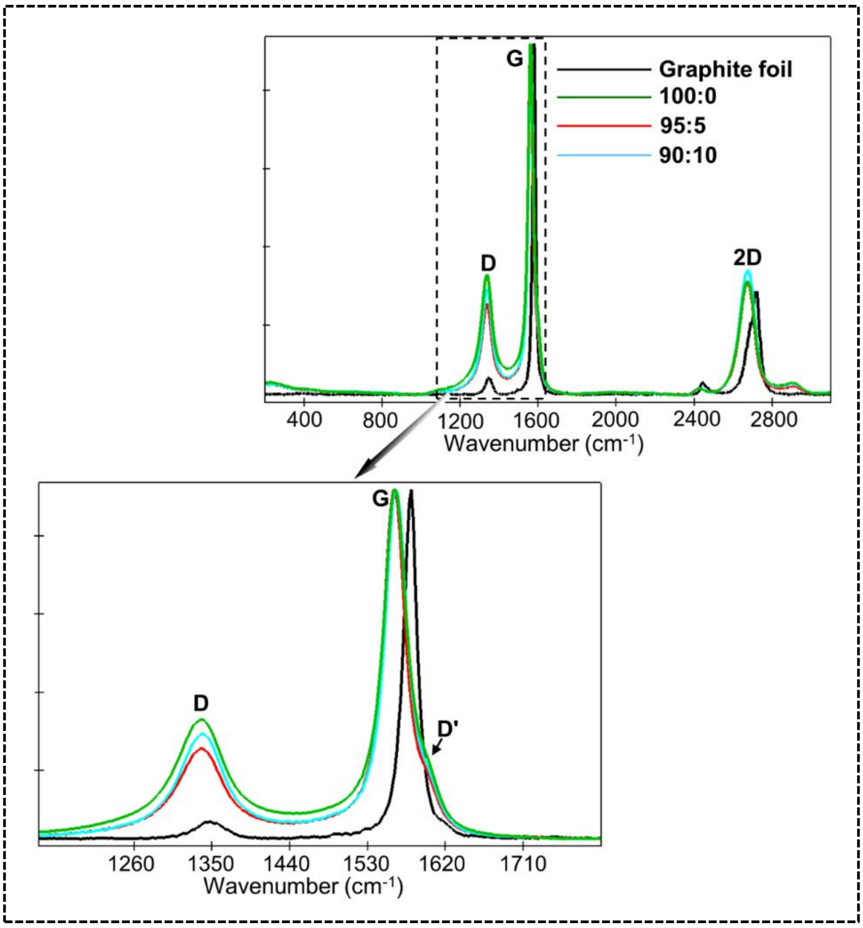

Figure 5.4 Average Raman spectra of EEG samples prepared with different H_2SO_4:H_3PO_4 concentrated acid intercalant-blend and 800 s intercalation time.

To further analyse the Raman features, the D and G band profiles in **Figure 5.4** were fitted using Lorentzian functions, as illustrated in **Figure 5.5(a)**. The extracted statistical parameters, including peak positions, widths, and integrated intensity ratios, are summarized in **Figures 5.5(b-f)**. The integrated intensity ratio of the D peak to the G peak (I_D/I_G) increases from 0.043 for the graphite foil to between 0.30 and 0.36 for EEG films synthesized with varying H_2SO_4:H_3PO_4 compositions (**Figure 5.5(b)**). Although a higher I_D/I_G ratio generally indicates increased disorder, it does not directly imply greater chemical doping, as the D-band intensity can also arise from multiple structural imperfections such as edges, strain, grain boundaries, amorphous carbon, and in-plane functionalization defects.

Similarly, the intensity ratio of the D′ peak to the G peak ($I_{D'}/I_G$) also increases, reaching values between 0.030 and 0.036. Notably, the EEG films exhibit D-G band profiles characterized by a prominent G peak and a relatively weak D peak, yielding an overall I_D/I_G ratio (~0.4) that is lower than typically reported for exfoliated graphene flakes (~1.5) [19]. This discrepancy likely arises from differences in morphological features, film stacking, or the level of wrinkling within the EEG films. As demonstrated by Nikolaievskyi et al. [20], crumpled or wrinkled few-layer graphene can exhibit significant G-band intensity enhancement by up to two orders of magnitude without a corresponding increase in D-band intensity. This enhancement occurs due to resonant scattering at specific laser excitation energies aligned with van Hove singularities (vHS) induced by stacking disorder or interlayer twist angles. Consequently, the I_D/I_G ratio may appear artificially low, leading to an underestimation of defect density.

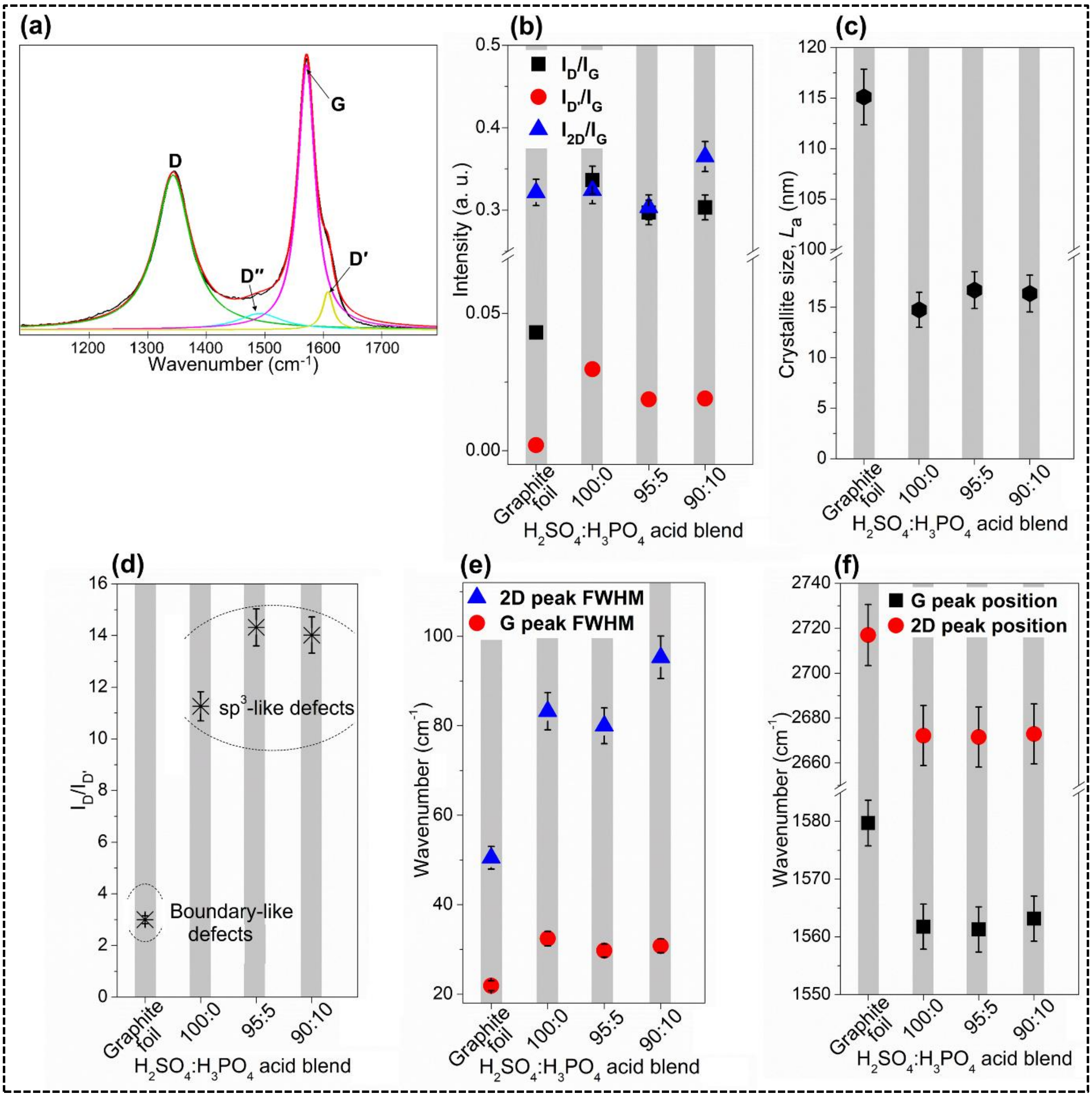

Figure 5.5 (a) Lorentzian fitting (solid lines) of the Raman spectra. Statistical analysis showing: (b) integrated intensity ratios of the D, D′, and 2D peaks relative to the G peak; (c) corresponding crystallite size estimated using the Knight formula; (d) $I_D/I_{D'}$ ratios of defect-activated modes; and (e,f) 2D and G peak widths and positions.

According to the Tuinstra and Koenig (TK) relation, the I_D/I_G ratio inversely correlates with crystallite size (L_a) [16]:

$$\frac{I_D}{I_G} = \frac{C(\lambda)}{L_a} \tag{5.1}$$

where, $C(\lambda) \approx C_0 + \lambda C_1$, for $400 \leq \lambda \geq 700$ nm, C(532 nm) = 4.96 nm, C_0 and C_1 are 12.6 and 0.033 nm, respectively [16].

In agreement with this model, **Figure 5.5(c)** shows that the crystallite size of graphite foil (115 nm) is an order of magnitude larger than that of EEG films (11 - 16 nm), confirming an increase in structural disorder after exfoliation. The defect nature can also be assessed from the ratio of the D′ to D band intensities, which provides insight into the dominant defect type [21]. The $I_D/I_{D'}$ ratio for graphite foil (~3.0) suggests boundary-type defects, while EEG films exhibit significantly higher values (11-14), characteristic of sp^3-type defects associated with heteroatom doping (**Figure 5.5(d)**).

For multilayer graphene, the ratio of the 2D to G band intensities (I_{2D}/I_G) is often used to estimate the number of layers and electronic band structure. However, in defective graphene, such as EEG, the pronounced D band broadening suppresses the 2D intensity, reducing the reliability of this method [21,22]. Nevertheless, **Figure 5.5(a)** shows a slight increase in I_{2D}/I_G with higher phosphoric acid content, suggesting subtle structural ordering. Additionally, the 2D band of EEG films appears more symmetrical than that of the graphite foil, which exhibits asymmetry due to Bernal (AB AB AB...) and rhombohedral (ABC ABC ABC...) stacking, as seen in **Figure 5.4** [18].

The full width at half maximum (FWHM) of the 2D band increases from 50.5 cm^{-1} for graphite foil to 83.3 cm^{-1} for the 100% H_2SO_4 -derived film, and further to ~100 cm^{-1} with increased phosphoric acid content (**Figure 5.5(e)**). This broadening is attributed to enhanced electron-phonon coupling and higher interfacial charge carrier density, implying an upward shift in the Fermi level [23,24]. Similarly, the G-band width increases from 21.9 cm^{-1} for graphite foil to ~32.4 cm^{-1} for EEG films, indicating increased bond-angle disorder and defect-induced charge carrier accumulation. The average 2D peak position downshifts from 2717 cm^{-1} in graphite foil to ~2672 cm^{-1} in EEG films (**Figure 5.5(f)**), consistent with n-type doping behaviour. The G peak also shifts from 1580 cm^{-1} to ~1562 cm^{-1}, further confirming the increase in carrier density.

From the same 100 × 100 μm^2 dataset shown in **Figure 5.4**, the Fermi level shift (ΔE_F) was determined from the G-band position relative to unexfoliated graphite. In doped graphene, the Fermi level moves away from the Dirac point the position corresponding to pristine graphene [25,26]. The shift is given by [27]:

$$\Delta E_F = \frac{\omega_G - 1500\ cm^{-1}}{42\ cm^{-1}/eV} \tag{5.2}$$

where $\Delta\omega_G$ is the G peak shift in EEG (or doped graphene) with respect to unexfoliated graphite foil (or pristine graphene) [27–29].

Raman mapping of the Fermi level shift is presented in **Figure 5.6**, showing an average shift of 0.4 - 0.5 eV across EEG films with varying H_2SO_4:H_3PO_4 ratios. This substantial upward shift confirms n-type doping induced by heteroatom incorporation. Interestingly, the Fermi level shift does not vary linearly with increasing phosphoric acid concentration, indicating a heterogeneous defect distribution that influences the local electronic environment beyond mere compositional effects. Such complexity highlights the interplay between defects, doping, and the electronic properties of EEG. Importantly, the upward Fermi level shift reduces the potential barrier (ΔE) between the film surface and the electrolyte's highest occupied molecular orbital (HOMO), thereby facilitating more efficient charge transfer during electrochemical processes [26,30].

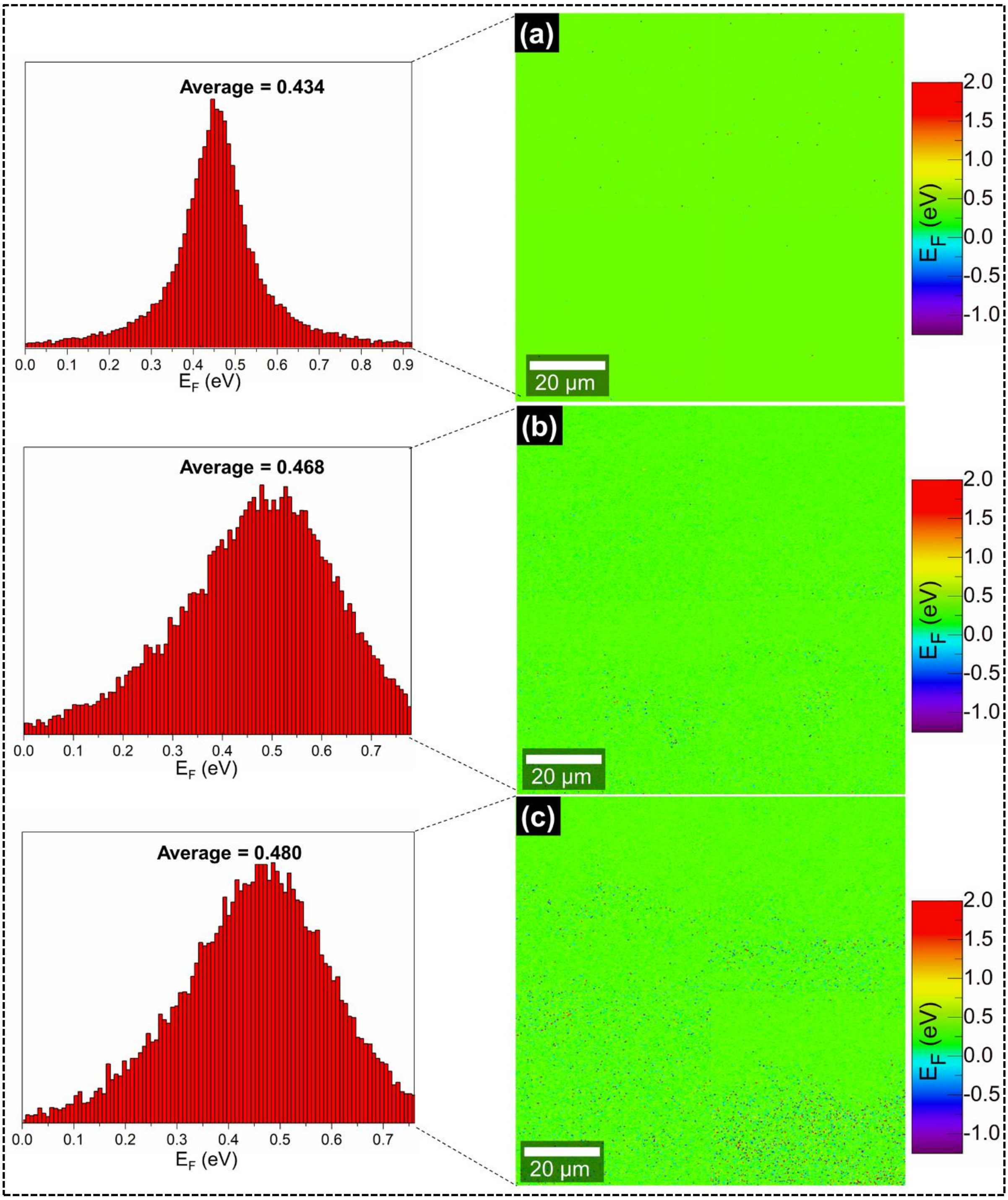

Figure 5.6. Raman mapping of Fermi level shift and corresponding histograms for EEG samples prepared with (a) 100:0, (b) 95:5, and (c) 90:10 H_2SO_4:H_3PO_4 intercalant blends and an intercalation time of 800 s.

The impact of this doping on charge transport is reflected in the electrical conductivity results shown in **Figure 5.7(a)**. The EEG film synthesized with 100% H_2SO_4 exhibited a relatively low conductivity (~500 S m^{-1}), comparable to that of the graphite foil. However, the incorporation of phosphoric acid significantly enhanced electrical conductivity, reaching ~10,000 S m-1 for the film prepared using the 90:10 H_2SO_4:H_3PO_4 mixture. This improvement can be attributed to the increased charge carrier density resulting from heteroatom doping, which promotes better electron transport pathways within the graphene framework. In addition to electrical performance, the mechanical behaviour of the films was evaluated using AFM force distance measurements, as illustrated in **Figure 5.7(b)**. The AFM cantilever used possessed a force constant of 0.2 N/m, a resonant frequency of 14 kHz, and a silicon tip radius of approximately 10 nm. The average adhesion force between the EEG films and the silicon substrate was measured at 5.2 nN, notably lower than that of unexfoliated graphite (8.4 nN). The reduced adhesion reflects the increased flexibility and decreased out-of-plane stiffness of the exfoliated graphene layers, enabling greater deformation under applied force.

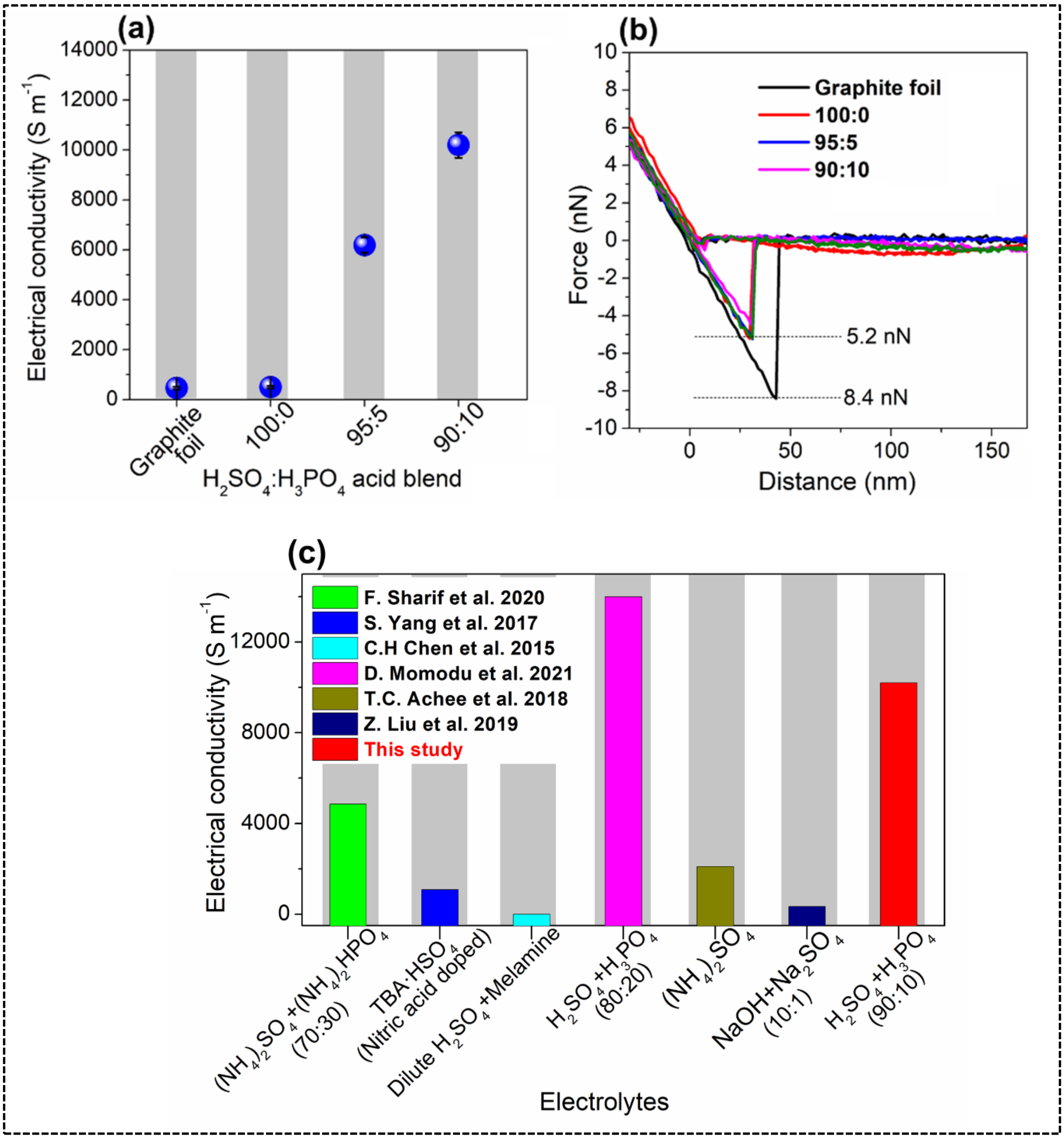

Figure 5.7 (a) Electrical conductivity and (b) adhesion force curves of EEG samples prepared using different H_2SO_4:H_3PO_4 concentrated acid intercalant blends and an intercalation time of 800 s. The solid green line represents a repeated measurement for the 100:0 H_2SO_4:H_3PO_4 sample. (c) Comparison of electrical conductivity obtained in this study with previously reported values using various electrolytes.

The electrical conductivity values obtained in this study are compared with those reported in previous works in **Figure 5.7(c)**. The measured conductivities surpass several earlier reports [3,31,32], indicating that the use of phosphate-containing acids effectively mitigates excessive oxidation during exfoliation. This reduction in oxidation limits the formation of oxygen-containing groups that disrupt the conjugated π-electron system, thereby preserving carrier mobility and conductivity. The EEG film synthesized under optimal conditions (90:10 H_2SO_4:H_3PO_4, 800 s intercalation) exhibited morphology, elemental composition, and conductivity consistent with those reported by Momodu et al. [3], confirming both the reproducibility and reliability of the synthesis process. Additional analyses of independently prepared samples demonstrated consistent structural and electronic characteristics, underscoring the robustness of the experimental approach.

5.2.2 Electrochemical characterization

Electrochemical measurements were conducted to establish a direct correlation between the observed Fermi level upshift in the EEG thin films and their enhanced electrochemical performance. A standard three-electrode configuration was employed using 1 M KOH as the electrolyte. The results are presented in **Figure 5.8**. **Figure 5.8(a, b)** displays the cyclic voltammetry (CV) curves for the cellulose membrane filter (0.45 µm, used during EEG filtration), graphite foil, and EEG films synthesized with H_2SO_4:H_3PO_4 intercalant ratios of 100:0 and 90:10. All measurements were recorded at a scan rate of 50 mV s^{-1} within a potential window of −0.4 to 0.0 V versus Ag/AgCl. The CV profiles for all electrodes exhibit quasi-rectangular shapes, characteristic of electric double-layer capacitive (EDLC) behaviour. However, the EEG electrodes display markedly higher current responses than graphite foil, confirming improved charge storage and conductivity. Notably, the film prepared with a 90:10

H_2SO_4:H_3PO_4 ratio shows the highest current response, suggesting that the incorporation of phosphoric acid enhances the electronic properties of the graphene network.

This improvement is attributed to the doping-induced Fermi level upshift, which raises the electronic energy of the EEG relative to the Dirac point. As a result, the potential barrier (ΔE) between the electrode Fermi level and the highest occupied molecular orbital (HOMO) of the electrolyte decreases, facilitating more efficient interfacial charge transfer, as schematically illustrated in **Figure 5.8(c)**. The magnitude of ΔE, defined by the energy difference between the electrode Fermi level and the HOMO-LUMO energy levels of the electrolyte, directly governs the kinetics of charge transfer at the interface [33].

Further insights into the capacitive behaviour are obtained from the galvanostatic charge-discharge (GCD) profiles shown in **Figure 5.8(d)**. The EEG electrode synthesized with a 90:10 H_2SO_4:H_3PO_4 ratio exhibits a notably longer discharge time than both graphite foil and the 100:0 EEG film, indicating superior energy storage capability. Based on the discharge slope, this electrode delivers a specific capacitance of 150.5 F g^{-1} at a current density of 1.0 A g^{-1}, demonstrating the beneficial effect of phosphoric acid doping on charge storage performance.

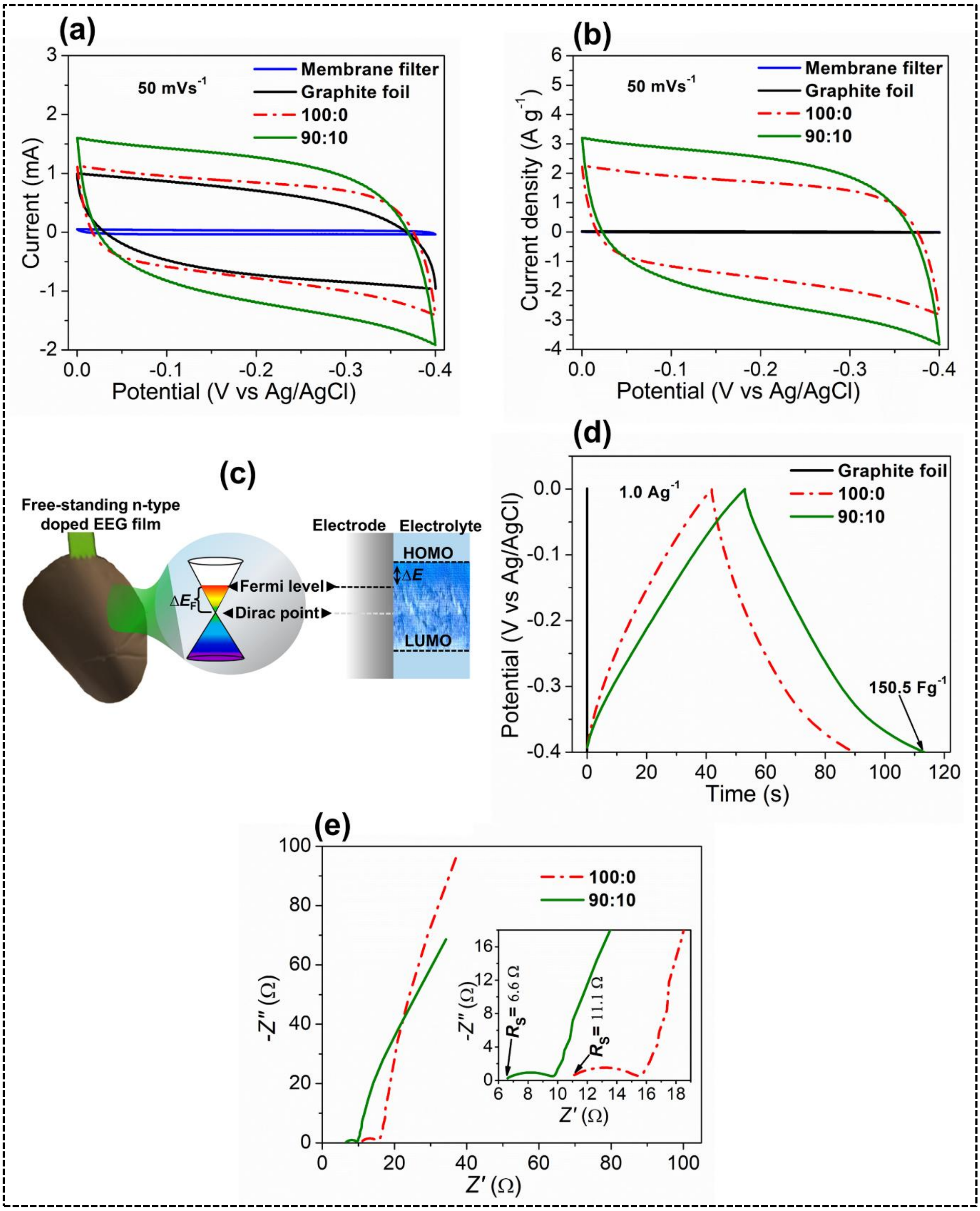

Figure 5.8 Electrochemical characterization: (a-b) CV curves of the membrane filter (0.45 μm cellulose membrane used for EEG filtration), graphite foil, and EEG films prepared with H_2SO_4:H_3PO_4 intercalant ratios of 100:0 and 90:10. (c) Schematic diagrams of the graphene cone energy band structure illustrating the Fermi level shift in doped EEG films and the

corresponding reduction in potential energy barrier (ΔE) for interfacial charge transfer between the electrode and electrolyte. (d) Galvanostatic charge-discharge curves of graphite foil and EEG electrodes recorded at a current density of 1.0 A g^{-1} within a potential window of −0.4 to 0.0 V vs. Ag/AgCl. (e) Nyquist plot showing the impedance behaviour.

To further elucidate the electrochemical behaviour, electrochemical impedance spectroscopy (EIS) was employed to evaluate both the electronic and ionic resistances, specifically the charge transfer resistance (R_{CT}) and the equivalent series resistance (R_S). The Nyquist plots presented in **Figure 5.8(e)** reveal that in the low-frequency region, EEG electrodes exhibit nearly vertical lines approaching the imaginary axis, confirming their capacitive nature. The 90:10 electrode displays a steeper slope and a shorter diffusion path compared to the 100:0 electrode, indicating faster ion transport and improved electrolyte accessibility at the electrode/electrolyte interface. In the high-frequency region, both electrodes exhibit semicircular arcs corresponding to charge transfer processes (see inset, **Figure 5.8(e)**). The 90:10 film shows a smaller semicircle with R_{CT} and R_S values of 3.1 Ω and 6.6 Ω, respectively significantly lower than those of the 100:0 film (R_{CT} = 4.4 Ω, R_S = 11.1 Ω). These findings clearly demonstrate that phosphoric acid incorporation reduces interfacial resistance and enhances electrical conductivity. This enhancement aligns with the Fermi level upshift discussed earlier, confirming that doping effectively minimizes interfacial potential barriers and accelerates charge transfer, leading to improved capacitive performance.

The specific capacitance obtained for the 90:10 EEG electrode (150.5 F g^{-1} at 1.0 A g^{-1} in 1 M KOH) compares favourably with values reported for similar graphene-based supercapacitors. For instance, Stoller et al. reported 135 F g^{-1} for chemically modified graphene in 1 M H_2SO_4 [34], while Chen et al. achieved 211.2 F g^{-1} at 0.2 A g^{-1} for a graphene/MnO_2 composite in 1 M

Na_2SO_4 [35]. Likewise, Wang et al. obtained 197 F g^{-1} at 0.5 A g^{-1} for nitrogen-doped graphene in 6 M KOH [36]. The performance of the 90:10 EEG electrode thus falls within the upper range of reported values [37], underscoring the effectiveness of phosphoric acid doping in enhancing electrical conductivity, charge carrier density, and interfacial charge transfer efficiency.

5.3 Conclusion

This study presents a simple and effective approach for producing freestanding, heteroatom-doped electrochemically exfoliated graphene (EEG) thin films, and provides a comprehensive investigation of their structural and electronic behaviour. Raman spectroscopy revealed pronounced Fermi level shifts (~0.5 eV), confirming substantial n-type doping and demonstrating strong agreement with theoretical predictions. The incorporation of nitrogen, phosphorus, and sulphur significantly enhanced electrical conductivity (reaching ~10 000 S m^{-1}), increased charge carrier density, and altered interfacial adhesion features highly favourable for flexible electronic and energy storage systems. Raman mapping further highlighted heterogeneous defect distributions and doping-induced electronic modifications across the films. Electrochemical analysis showed that the upward Fermi level shift promotes improved interfacial charge transfer, consistent with the enhanced conductivity introduced by multi-element doping. Overall, these findings establish a robust framework for tailoring the structural, electronic, and mechanical properties of doped EEG films, supporting their advancement toward scalable applications including flexible micro-supercapacitors, sensors, and catalytic devices.

References

[1] N.S. Mankge, M.J. Madito, N.W. Hlongwa, A.T. Kuvarega, Review of electrochemical production of doped graphene for energy storage applications, J. Energy Storage 46 (2022). https://doi.org/10.1016/j.est.2021.103527.

[2] A. Ambrosi, M. Pumera, Electrochemically Exfoliated Graphene and Graphene Oxide for Energy Storage and Electrochemistry Applications, Chemistry – A European Journal 22 (2016) 153–159. https://doi.org/10.1002/chem.201503110.

[3] D. Momodu, M.J. Madito, A. Singh, F. Sharif, K. Karan, M. Trifkovic, S. Bryant, E.P.L. Roberts, Mixed-acid intercalation for synthesis of a high conductivity electrochemically exfoliated graphene, Carbon N. Y. 171 (2021) 130–141. https://doi.org/10.1016/j.carbon.2020.08.066.

[4] P. Simon, Y. Gogotsi, Materials for electrochemical capacitors, Nat. Mater. 7 (2008) 845–854.

[5] D. Momodu, A.S. Zeraati, F.L. Pablos, U. Sundararaj, E.P. Roberts, Hybrid energy storage using nitrogen-doped graphene and layered-MXene (Ti3C2) for stable high-rate supercapacitors, Electrochim. Acta 388 (2021) 138664. https://doi.org/10.1016/j.electacta.2021.138664.

[6] L.L. Zhang, X. Zhao, H. Ji, M.D. Stoller, L. Lai, S. Murali, S. McDonnell, B. Cleveger, R.M. Wallace, R.S. Ruoff, Nitrogen doping of graphene and its effect on quantum capacitance, and a new insight on the enhanced capacitance of N-doped carbon, Energy Environ. Sci. 5 (2012) 9618–9625. https://doi.org/10.1039/c2ee23442d.

[7] N.S. Mankge, M.J. Madito, N.W. Hlongwa, A.T. Kuvarega, Review of electrochemical production of doped graphene for energy storage applications, J. Energy Storage 46 (2022). https://doi.org/10.1016/j.est.2021.103527.

[8] C.-Y. Su, A.-Y. Lu, Y. Xu, F.-R. Chen, A.N. Khlobystov, L.-J. Li, High-Quality Thin Graphene Films from Fast Electrochemical Exfoliation, ACS Nano 5 (2011) 2332–2339. https://doi.org/10.1021/nn200025p.

[9] M.J. Madito, Correlation of the Graphene Fermi-Level Shift and the Enhanced Electrochemical Performance of Graphene-Manganese Phosphate for Hybrid Supercapacitors : Raman Spectroscopy Analysis, ACS Appl. Mater. Interfaces 13 (2021) 37014–37026. https://doi.org/10.1021/acsami.1c07104.

[10] A.C. Ferrari, D.M. Basko, Raman spectroscopy as a versatile tool for studying the properties of graphene., Nat. Nanotechnol. 8 (2013) 235–46. https://doi.org/10.1038/nnano.2013.46.

[11] J. Bin Wu, M.L. Lin, X. Cong, H.N. Liu, P.H. Tan, Raman spectroscopy of graphene-based materials and its applications in related devices, Chem. Soc. Rev. 47 (2018) 1822–1873. https://doi.org/10.1039/c6cs00915h.

[12] M.J. Madito, Revisiting the Raman disorder band in graphene-based materials: A critical review, Vib. Spectrosc. 139 (2025). https://doi.org/10.1016/j.vibspec.2025.103814.

[13] D. Momodu, M.J. Madito, A. Singh, F. Sharif, K. Karan, M. Trifkovic, S. Bryant, E.P.L. Roberts, Mixed-acid intercalation for synthesis of a high conductivity electrochemically exfoliated graphene, Carbon N. Y. 171 (2021) 130–141. https://doi.org/10.1016/J.CARBON.2020.08.066.

[14] S. Stankovich, D.A. Dikin, R.D. Piner, K.A. Kohlhaas, A. Kleinhammes, Y. Jia, Y. Wu, S.T. Nguyen, R.S. Ruoff, Synthesis of graphene-based nanosheets via chemical reduction of exfoliated graphite oxide, Carbon N. Y. 45 (2007) 1558–1565. https://doi.org/10.1016/j.carbon.2007.02.034.

[15] D.R. Dreyer, S. Park, C.W. Bielawski, R.S. Ruoff, The chemistry of graphene oxide, Chem. Soc. Rev. 39 (2010) 228–240. https://doi.org/10.1039/B917103G.

[16] D. Yang, A. Velamakanni, G. Bozoklu, S. Park, M. Stoller, R.D. Piner, S. Stankovich, I. Jung, D.A. Field, C.A. Ventrice, R.S. Ruoff, Chemical analysis of graphene oxide films after heat and chemical treatments by X-ray photoelectron and Micro-Raman spectroscopy, Carbon N. Y. 47 (2009) 145–152. https://doi.org/10.1016/j.carbon.2008.09.045.

[17] J. Park, Y.J. Jang, Y.J. Kim, M. Song, S. Yoon, D.H. Kim, S.-J. Kim, Sulfur-doped graphene as a potential alternative metal-free electrocatalyst and Pt-catalyst supporting material for oxygen reduction reaction, Phys. Chem. Chem. Phys. 16 (2014) 103–109. https://doi.org/10.1039/C3CP54311K.

[18] A.C. Ferrari, J. Robertson, Interpretation of Raman spectra of disordered and amorphous carbon, Phys. Rev. B 61 (2000) 14095–14107. https://doi.org/10.1103/PhysRevB.61.14095.

[19] A.C. Ferrari, D.M. Basko, Raman spectroscopy as a versatile tool for studying the properties of graphene, Nat. Nanotechnol. 8 (2013) 235–246. https://doi.org/10.1038/nnano.2013.46.

[20] F. Tuinstra, J.L. Koenig, Raman Spectrum of Graphite, J. Chem. Phys. 53 (1970) 1126–1130. https://doi.org/10.1063/1.1674108.

[21] M.J. Madito, Correlation of the Graphene Fermi-Level Shift and the Enhanced Electrochemical Performance of Graphene-Manganese Phosphate for Hybrid Supercapacitors: Raman Spectroscopy Analysis, ACS Appl. Mater. Interfaces 13 (2021) 37014–37026. https://doi.org/10.1021/acsami.1c07104.

[22] J.-B. Wu, M.-L. Lin, X. Cong, H.-N. Liu, P.-H. Tan, Raman spectroscopy of graphene-based materials and its applications in related devices, Chem. Soc. Rev. 47 (2018) 1822–1873. https://doi.org/10.1039/C6CS00915H.

[23] D. Momodu, M.J. Madito, A. Singh, F. Sharif, K. Karan, M. Trifkovic, S. Bryant, E.P.L. Roberts, Mixed-acid intercalation for synthesis of a high conductivity electrochemically exfoliated graphene, Carbon N. Y. 171 (2021) 130–141. https://doi.org/10.1016/j.carbon.2020.08.066.

[24] D. Nikolaievskyi, M. Torregrosa, A. Merlen, S. Clair, O. Chuzel, J.-L. Parrain, T. Neisus, A. Campos, M. Cabie, C. Martin, C. Pardanaud, Wrinkling and crumpling in twisted few and multilayer CVD graphene: High density of edge modes influencing Raman spectra, Carbon N. Y. 203 (2023) 650–660. https://doi.org/10.1016/j.carbon.2022.12.010.

[25] A. Eckmann, A. Felten, A. Mishchenko, L. Britnell, R. Krupke, K.S. Novoselov, C. Casiraghi, Probing the Nature of Defects in Graphene by Raman Spectroscopy, Nano Lett. 12 (2012) 3925–3930. https://doi.org/10.1021/nl300901a.

[26] M.M. Lucchese, F. Stavale, E.H.M. Ferreira, C. Vilani, M.V.O. Moutinho, R.B. Capaz, C.A. Achete, A. Jorio, Quantifying ion-induced defects and Raman relaxation length in graphene, Carbon N. Y. 48 (2010) 1592–1597. https://doi.org/10.1016/j.carbon.2009.12.057.

[27] A. Das, S. Pisana, B. Chakraborty, S. Piscanec, S.K. Saha, U. V. Waghmare, K.S. Novoselov, H.R. Krishnamurthy, A.K. Geim, A.C. Ferrari, A.K. Sood, Monitoring dopants by Raman scattering in an electrochemically top-gated graphene transistor, Nat. Nanotechnol. 3 (2008) 210–215. https://doi.org/10.1038/nnano.2008.67.

[28] M.J. Madito, Correlation of the Graphene Fermi-Level Shift and the Enhanced Electrochemical Performance of Graphene-Manganese Phosphate for Hybrid Supercapacitors: Raman Spectroscopy Analysis, ACS Appl. Mater. Interfaces 13 (2021) 37014–37026. https://doi.org/10.1021/acsami.1c07104.

[29] H. Liu, Y. Liu, D. Zhu, Chemical doping of graphene, J. Mater. Chem. 21 (2011) 3335–3345. https://doi.org/10.1039/C0JM02922J.

[30] A.K. Singh, N. Yasri, K. Karan, E.P.L. Roberts, Electrocatalytic Activity of Functionalized Carbon Paper Electrodes and Their Correlation to the Fermi Level Derived from Raman Spectra, ACS Appl. Energy Mater. 2 (2019) 2324–2336. https://doi.org/10.1021/acsaem.9b00180.

[31] C.-F. Chen, C.-H. Park, B.W. Boudouris, J. Horng, B. Geng, C. Girit, A. Zettl, M.F. Crommie, R.A. Segalman, S.G. Louie, F. Wang, Controlling inelastic light scattering quantum pathways in graphene, Nature 471 (2011) 617–620. https://doi.org/10.1038/nature09866.

[32] G. Wu, X. Tang, M. Meyyappan, K.W.C. Lai, Doping effects of surface functionalization on graphene with aromatic molecule and organic solvents, Appl. Surf. Sci. 425 (2017) 713–721. https://doi.org/10.1016/j.apsusc.2017.07.048.

[33] H. Yan, F. Xia, W. Zhu, M. Freitag, C. Dimitrakopoulos, A.A. Bol, G. Tulevski, P. Avouris, Infrared Spectroscopy of Wafer-Scale Graphene, ACS Nano 5 (2011) 9854–9860. https://doi.org/10.1021/nn203506n.

[34] D. Zhao, S. Li, Regulating the Performance of Lithium-Ion Battery Focus on the Electrode-Electrolyte Interface, Front. Chem. 8 (2020). https://doi.org/10.3389/fchem.2020.00821.

[35] F. Sharif, A.S. Zeraati, P. Ganjeh-Anzabi, N. Yasri, M. Perez-Page, S.M. Holmes, U. Sundararaj, M. Trifkovic, E.P.L. Roberts, Synthesis of a high-temperature stable electrochemically exfoliated graphene, Carbon N. Y. 157 (2020) 681–692. https://doi.org/10.1016/j.carbon.2019.10.042.

[36] Z. Liu, H. Zhang, M. Eredia, H. Qiu, W. Baaziz, O. Ersen, A. Ciesielski, M. Bonn, H.I. Wang, P. Samorì, Water-Dispersed High-Quality Graphene: A Green Solution for Efficient Energy Storage Applications, ACS Nano 13 (2019) 9431–9441. https://doi.org/10.1021/acsnano.9b04232.

[37] D. Zhao, S. Li, Regulating the Performance of Lithium-Ion Battery Focus on the Electrode-Electrolyte Interface, Front. Chem. 8 (2020). https://doi.org/10.3389/fchem.2020.00821.

[38] M.D. Stoller, S. Park, Y. Zhu, J. An, R.S. Ruoff, Graphene-Based Ultracapacitors, Nano Lett. 8 (2008) 3498–3502. https://doi.org/10.1021/nl802558y.

[39] S. Chen, J. Zhu, X. Wu, Q. Han, X. Wang, Graphene Oxide−MnO_2 Nanocomposites for Supercapacitors, ACS Nano 4 (2010) 2822–2830. https://doi.org/10.1021/nn901311t.

[40] K. Wang, L. Li, T. Zhang, Z. Liu, Nitrogen-doped graphene for supercapacitor with long-term electrochemical stability, Energy 70 (2014) 612–617. https://doi.org/10.1016/j.energy.2014.04.034.

[41] Y. Zhu, S. Murali, W. Cai, X. Li, J.W. Suk, J.R. Potts, R.S. Ruoff, Graphene and Graphene Oxide: Synthesis, Properties, and Applications, Advanced Materials 22 (2010) 3906–3924. https://doi.org/10.1002/adma.201001068.

CHAPTER 6

Ni-Mn PHOSPHATE/ELECTROCHEMICALLY EXFOLIATED GRAPHENE COMPOSITE FOR HYBRID SUPERCAPACITORS

6.1 Introduction

To enhance the efficiency of supercapacitor devices, carbon-based EDLC electrodes are often coupled with pseudocapacitive materials such as transition metal phosphates (TMPs), which provide abundant redox-active sites. These materials can be integrated with carbon nanostructures or used as complementary electrodes in hybrid supercapacitor configurations. TMPs have gained increasing attention due to their multiple oxidation states, structural robustness, and low cost, offering advantages over metal oxides, sulphides, and nitrides [1–5]. Examples such as $Co_3(PO_4)_2$ [6], $Ni_2P_2O_7$ [7], and $Mn_3(PO_4)_2$ [8] have demonstrated promising electrochemical behaviour. Among them, nickel-based phosphates generally deliver high capacitance, whereas manganese-based phosphates are valued for their cycling stability and long operational lifespan [7–9].

Nickel-manganese phosphates, in particular, benefit from the complementary electrochemical activity of both metal centres within a stable phosphate framework [10,11], making them strong candidates for hybrid supercapacitor electrodes. However, their intrinsically low electrical conductivity restricts electron transport and limits rate capability [11]. To address this challenge, these phosphates are commonly combined with conductive carbon nanostructures.

This chapter is published as T. Kgwadibane et al., J. Energy Storage.152 (2026).120697.

Electrochemically exfoliated graphene (EEG) is especially beneficial due to its excellent conductivity, chemical stability, and two-dimensional morphology, which collectively enhance electron mobility, improve electrode-electrolyte interactions, and accelerate redox reactions [12,13].

In this study, nickel-manganese phosphate/electrochemically exfoliated graphene ($NiMn(PO_4)_2$/EEG) nanocomposites were synthesized via a hydrothermal method and paired with activated carbon derived from wastewater sludge for hybrid supercapacitor applications. The $NiMn(PO_4)_2$/50 mg EEG//AC device using $NiMn(PO_4)_2$/EEG as the positive electrode and sludge-derived activated carbon as the negative electrode exhibited high electrochemical performance and excellent cycling stability. These results demonstrate the strong synergistic effect between $NiMn(PO_4)_2$/EEG and sustainable activated carbon, highlighting their potential for high-performance, environmentally responsible energy storage. Additionally, the use of wastewater sludge as a carbon precursor offers a valuable pathway for waste-to-energy material conversion.

6.2 Results and discussion

6.2.1 Physicochemical and structural characterisation

The surface morphology of the as-synthesised $NiMn(PO_4)_2$, EEG, and $NiMn(PO_4)_2$/EEG composites was examined using scanning electron microscopy (SEM), as shown in **Figure 6.1(a-d)**. The pristine $NiMn(PO_4)_2$ micrograph **(Figure 6.1(a))** exhibits well-defined hexagonal micro-rods, characteristic of a highly ordered crystalline structure. In contrast, the EEG micrograph **(Figure 6.1(b))** reveals a sheet-like morphology typical of multi-layer graphene, confirming the successful exfoliation and restacking of graphene layers.

A distinct morphological transformation is observed upon the incorporation of EEG into the $NiMn(PO_4)_2$ matrix. In the composite containing 50 mg of EEG **(Figure 6.1(c))**, the $NiMn(PO_4)_2$ micro-rods are anchored onto the EEG sheets, appearing smaller and more agglomerated compared to the pristine sample. This reduction in particle size can be attributed to the strong interfacial interactions between Ni^{2+}/Mn^{2+} precursors and oxygen-containing functional groups present on the EEG surface. These functional groups serve as heterogeneous nucleation sites, promoting extensive nucleation while simultaneously restricting crystal growth. Consequently, smaller micro-rods are formed, which are expected to provide a larger electrochemically active surface area, thereby enhancing charge storage performance.

However, with further increase in EEG content to 100 mg **(Figure 6.1(d))**, the $NiMn(PO_4)_2$ micro-rods become larger and more closely resemble the pristine morphology. This change is likely due to the higher carbon content, which reduces the availability of metal cations per nucleation site, limiting new nucleus formation and favouring the coalescence and growth of existing micro-rods. Excessive EEG may also induce partial agglomeration or restacking of graphene layers, which can obscure active sites and hinder uniform dispersion of $NiMn(PO_4)_2$ micro-rods. Therefore, the observed variation in micro-rod size with increasing EEG content reflects a delicate balance between nucleation density and crystal growth rate, governed by the degree of interaction between the phosphate precursors and the conductive carbon matrix

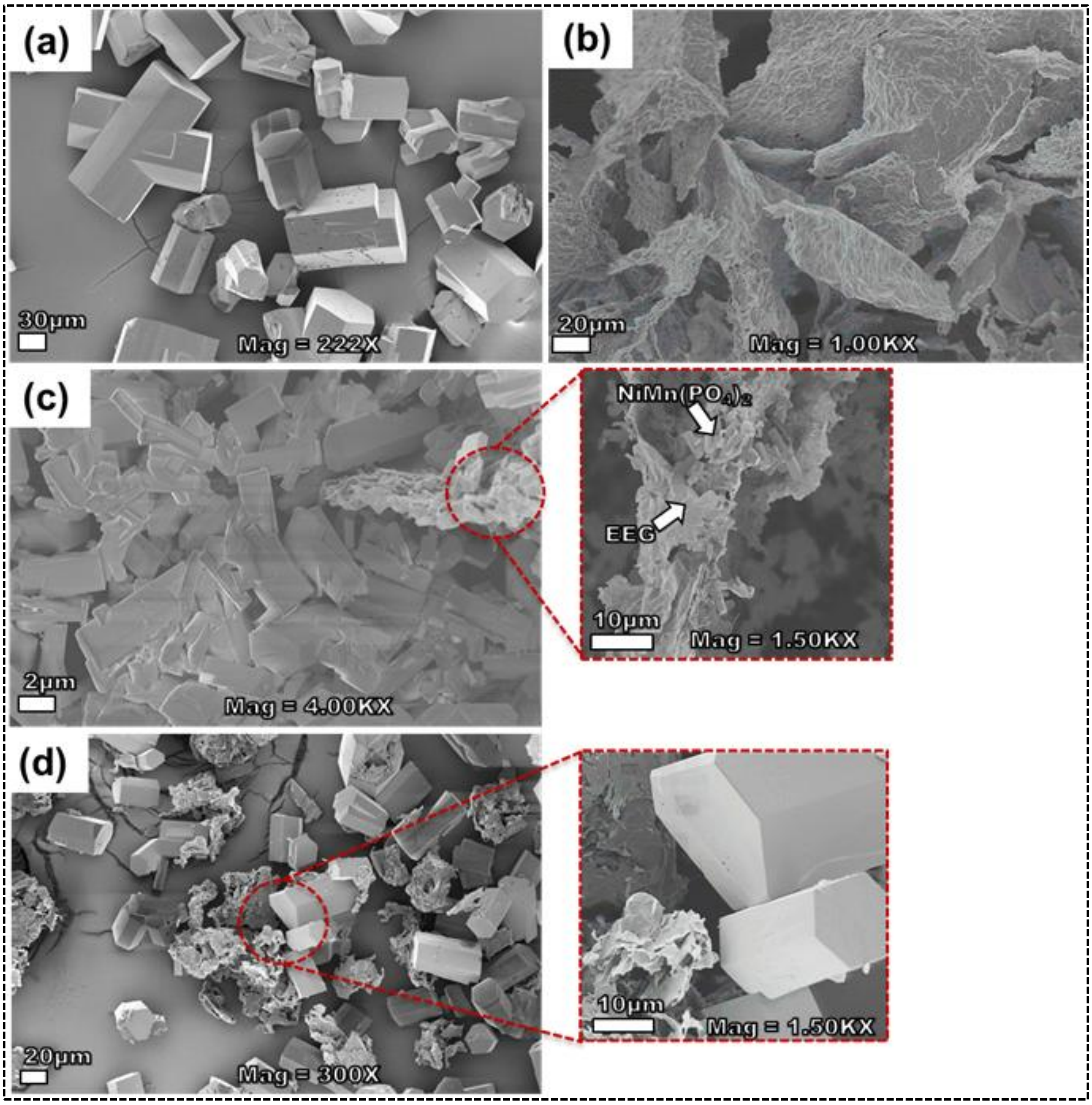

Figure 6.1 SEM micrographs of the as-synthesized materials: (a) $NiMn(PO_4)_2$, (b) EEG, (c) $NiMn(PO_4)_2$/50 mg EEG composite, and (d) $NiMn(PO_4)_2$/100 mg EEG composite.

Elemental composition analysis further confirms the successful synthesis of the individual components and composites. The EDS spectrum of pristine $NiMn(PO_4)_2$ **(Figure 6.2(a))** reveals the presence of nickel (11.6 wt%), manganese (37.7 wt%), oxygen (36.4 wt%), and phosphorus (14.3 wt%), consistent with the expected stoichiometry of $NiMn(PO_4)_2$. The EDS spectrum of EEG **(Figure 6.2(b))** shows carbon (77.8 wt%), oxygen (18.7 wt%), sulphur (2.9 wt%), and phosphorus (0.7 wt%), confirming the successful incorporation of these heteroatoms into the graphene framework. The EEG was synthesised using a H_2SO_4:H_3PO_4 intercalant ratio of 70:30 and an intercalation time of 800 seconds. Incorporation of heteroatoms such as sulphur and phosphorus into graphene has been reported to improve electrical conductivity, surface reactivity, and thermal stability [14]. The EDS spectra of the $NiMn(PO_4)_2$/EEG composites **(Figure 6.2(c, d))** exhibit signals corresponding to both the $NiMn(PO_4)_2$ and EEG components, confirming successful composite formation.

Structural analysis using XRD further supports these findings. The XRD pattern of the as-synthesised $NiMn(PO_4)_2$, presented in **Figure 6.3(a)**, exhibits sharp and well-defined diffraction peaks, indicative of high crystallinity. The diffraction reflections correspond to the Inorganic Crystal Structure Database (ICSD) reference 30802 ($Mn_{0.9}Ni_{2.1}(PO_4)_2$), confirming the formation of an olivine-related sarcopside-type phase that crystallises in a monoclinic system (space group $P121/a1$) with distinct lattice parameters. Additional peaks can be indexed to $Ni_3(PO_4)_2$ (ICSD 153160) and $Mn_3(PO_4)_2$ (ICSD 411377), both of which crystallise in the monoclinic ($P121/c1$) space group. The coexistence of these reflections verifies the formation of a mixed-metal phosphate solid solution comprising both Ni and Mn species.

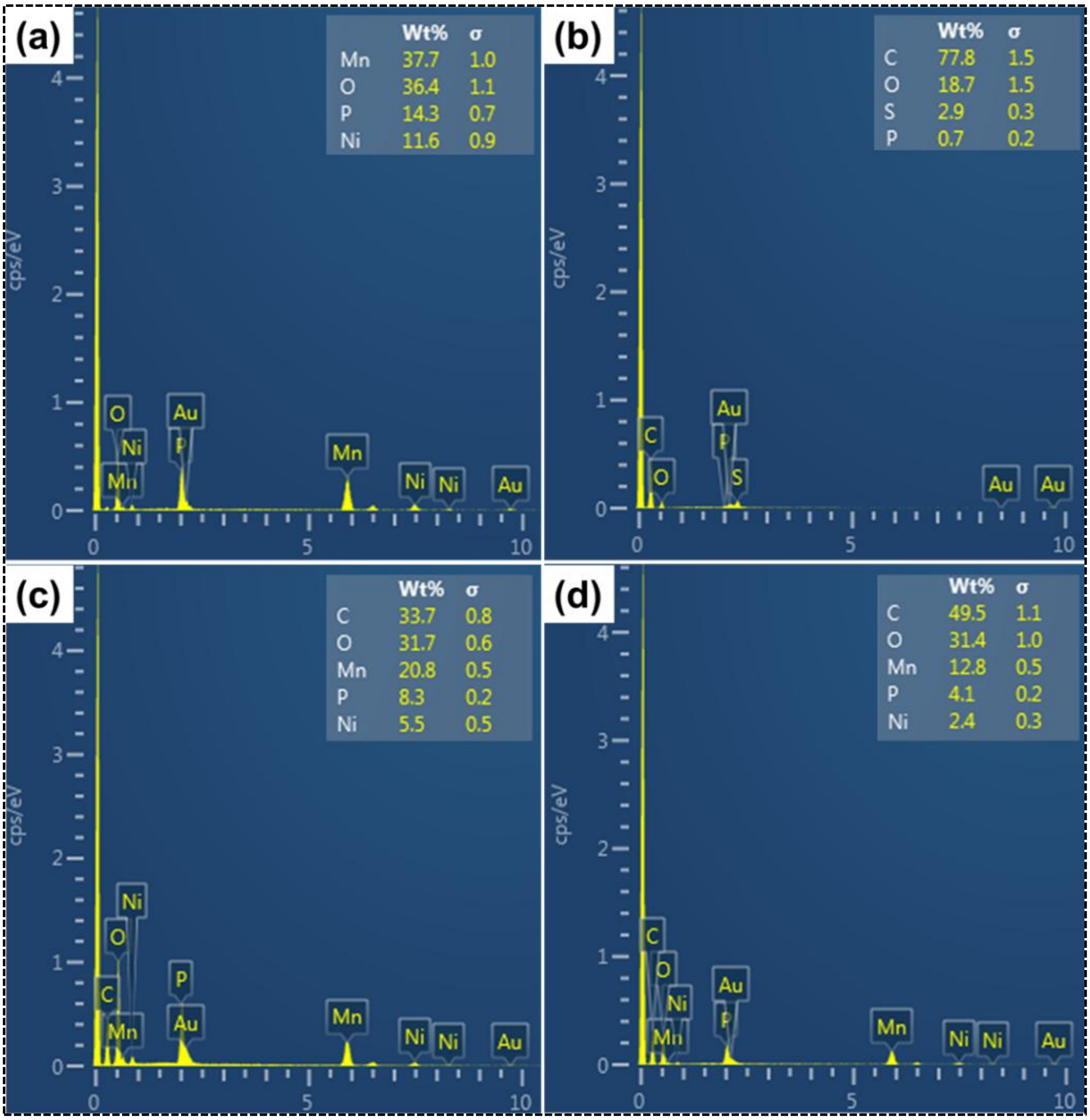

(a)

	Wt%	σ
Mn	37.7	1.0
O	36.4	1.1
P	14.3	0.7
Ni	11.6	0.9

(b)

	Wt%	σ
C	77.8	1.5
O	18.7	1.5
S	2.9	0.3
P	0.7	0.2

(c)

	Wt%	σ
C	33.7	0.8
O	31.7	0.6
Mn	20.8	0.5
P	8.3	0.2
Ni	5.5	0.5

(d)

	Wt%	σ
C	49.5	1.1
O	31.4	1.0
Mn	12.8	0.5
P	4.1	0.2
Ni	2.4	0.3

Figure 6.2 EDS spectra of the as-synthesized (a) $NiMn(PO_4)_2$, (b) EEG, (c) $NiMn(PO_4)_2$/50 mg EEG composite, (d) $NiMn(PO_4)_2$/100 mg EEG composite, confirming elemental composition.

For phase identification and indexing, ICSD reference patterns were employed, and colour-coded histograms were used to visually distinguish Ni-, Mn-, and mixed-metal phosphate phases. Structurally, sarcopside-type $NiMn(PO_4)_2$ adopts an olivine-related monoclinic framework constructed from edge-sharing MO_6 (M = $\mathrm{Ni}^{2+,}$ Mn^{2+}) octahedra interconnected by PO_4 tetrahedra [15]. The octahedral chains extend along the *b*-axis and are cross-linked by phosphate groups, forming a robust three-dimensional network. Partial substitution between Ni^{2+} and Mn^{2+} induces slight lattice distortions while maintaining the overall structural integrity, resulting in a stable solid-solution-type lattice. This mixed-metal configuration enhances both the structural robustness and the electronic/ionic transport properties of the phosphate framework.

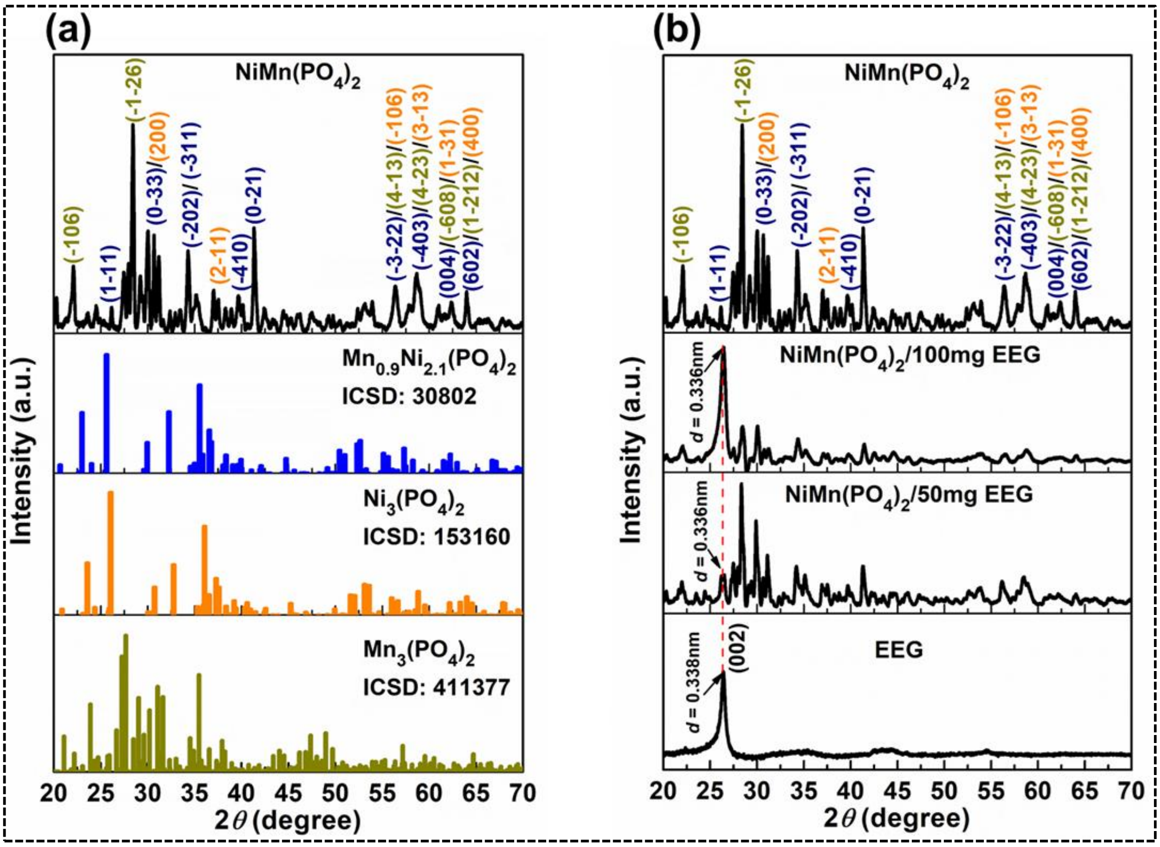

Figure 6.3 XRD patterns of the as-synthesized $NiMn(PO_4)_2$, EEG, $NiMn(PO_4)_2$/50 mg EEG, and $NiMn(PO_4)_2$/100 mg EEG composites. Reference diffraction patterns in (a) are obtained from the Inorganic Crystal Structure Database (ICSD).

The XRD patterns of the $NiMn(PO_4)_2$/EEG composites, shown in **Figure 6.3(b)**, reveal diffraction features attributable to both pristine $NiMn(PO_4)_2$ and EEG. The EEG exhibits a characteristic (002) reflection at $2\theta = 26.4°$, corresponding to an average interlayer spacing (*d*-spacing) of 0.338 nm, typical of few-layer graphene [16]. The retention of a similar (002) *d*-spacing in the composite suggests that $NiMn(PO_4)_2$ nanocrystals are predominantly anchored on the EEG surface rather than intercalated between graphene layers. This configuration promotes intimate interfacial contact between the phosphate phase and the conductive carbon matrix, which is expected to facilitate efficient charge transport and improve electrochemical performance.

Figure 6.4(a) presents the FTIR spectra of the as-synthesised pristine $NiMn(PO_4)_2$, EEG, and $NiMn(PO_4)_2$/EEG composite samples. The FTIR spectrum of pristine $NiMn(PO_4)_2$ exhibits distinct vibrational peaks at 1030 cm^{-1}, attributed to P–O stretching, and at 525 and 583 cm^{-1}, which correspond to P–O bending and metal–oxygen (Ni–O and Mn–O) vibrations, respectively [17–20]. Additional absorption bands observed near 1540 cm^{-1} and 3400 cm^{-1} are assigned to O–H stretching vibrations, indicating the presence of surface hydroxyl groups and adsorbed moisture. The FTIR spectrum of pristine electrochemically exfoliated graphene (EEG) displays characteristic vibrational bands at 1019 cm^{-1} (C–O stretching), 1400 cm^{-1} (C–OH bending), and 2950 cm^{-1} (C–H stretching), together with a broad band near 3400 cm^{-1} corresponding to O–H stretching vibrations. A distinct band at 1650 cm^{-1} is attributed to C=C stretching within the graphitic domains of the EEG structure. The FTIR spectrum of the $NiMn(PO_4)_2$/EEG composite exhibits vibrational features characteristic of both $NiMn(PO_4)_2$ and EEG, confirming the successful integration of the two phases into a single composite matrix.

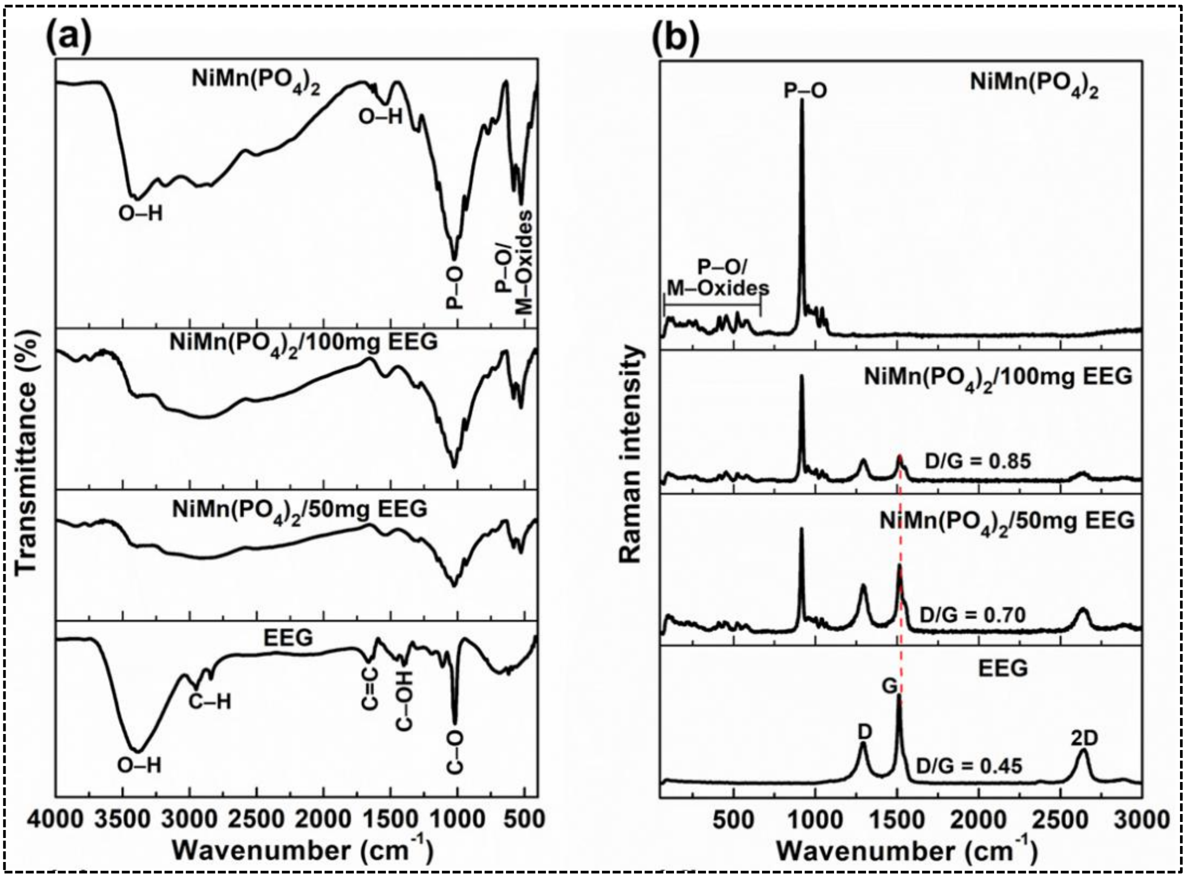

Figure 6.4 (a) FTIR spectra and (b) Raman spectra of the as-synthesized $NiMn(PO_4)_2$, EEG, $NiMn(PO_4)_2$/50 mg EEG, and $NiMn(PO_4)_2$/100 mg EEG composites.

Raman spectroscopy was employed to further elucidate the structural and chemical characteristics of the as-synthesised materials, as shown in **Figure 6.4(b)**. The Raman spectrum of EEG displays well-defined peaks corresponding to the D-band (1309 cm^{-1}), G-band (1582 cm^{-1}), and 2D-band (2623 cm^{-1}). The G-band arises from the stretching vibrations of sp^2-hybridised carbon atoms in aromatic rings and is associated with longitudinal and transverse optical phonon modes of E_{2g} symmetry at the Γ point [21–23]. According to Raman selection rules, the G-band results from a first-order Raman scattering process, whereas the D- and 2D-bands originate from double- or triple-resonance scattering involving one or two phonons [10,12,16]. The D-band is typically activated by structural defects or edge irregularities, while the 2D-band is a second-order overtone of the D-band and does not require defects for activation.

For the $NiMn(PO_4)_2$/EEG composite **(Figure 6.4(b))**, Raman peaks appear at 1292 cm^{-1} (D-band), 1516 cm^{-1} (G-band), and 2634 cm^{-1} (2D-band). The G-band exhibits an upshift from 1512 cm^{-1} in pristine EEG to approximately 1516 cm^{-1} in the composite, signifying an increase in charge carrier density. This shift indicates improved electrical conductivity in the $NiMn(PO_4)_2$/EEG composite and agrees with previous reports showing that the G-band position in chemically doped graphene varies linearly with the Fermi energy [26]. Moreover, the D-to-G intensity ratio (I_D/I_G) increases from 0.45 in pristine EEG to ≥ 0.7 in the composite, reflecting an increased defect density attributed to doping-induced interactions between $NiMn(PO_4)_2$ and the graphene framework.

The Raman spectrum of pristine $NiMn(PO_4)_2$ **(Figure 6.4(b))** displays characteristic vibrational modes of phosphate oxyanions, including a symmetric stretching mode at 919 cm^{-1} and antisymmetric stretching modes at 956, 1004, and 1041 cm^{-1} [27,28]. Additional peaks at 415/453, 523, and 579 cm^{-1} correspond to symmetric bending vibrations of Ni-O-P and Mn-O-P linkages within the PO_4^{3-} group, as well as P-O-Ni and P-O-Mn bonds [17–20].

Overall, the combined FTIR and Raman analyses confirm the coexistence of characteristic features from both $NiMn(PO_4)_2$ and EEG within the composite. The observed peak shifts and intensity variations indicate strong interfacial interactions between the phosphate framework and the conductive graphene matrix. These interactions are expected to facilitate electron transport and ion diffusion, thereby enhancing the electrochemical performance of the composite material**.**

6.2.2 Electrochemical characterization

The electrochemical performance of the as-synthesised $NiMn(PO_4)_2$ and $NiMn(PO_4)_2$/EEG composite electrodes was investigated using a conventional three-electrode configuration in aqueous 1 M KOH electrolyte within a potential window of 0.0-0.45 V versus Ag/AgCl. **Figure 6.5(a,b)** presents the cyclic voltammetry (CV) and galvanostatic charge–discharge (GCD) curves for both electrodes recorded at a scan rate of 5 mV s^{-1} and a current density of 1 A g^{-1}, respectively. The incorporation of 50 mg EEG into the $NiMn(PO_4)_2$ matrix markedly enhances the current response and discharge duration compared to the pristine electrode, indicating improved charge-transfer kinetics and enhanced electrochemical activity. In contrast, the $NiMn(PO_4)_2$/100 mg EEG electrode exhibits a reduced current response, likely due to excessive graphene loading, which induces sheet aggregation, limits electrolyte penetration, and obstructs access to electroactive sites. The $NiMn(PO_4)_2$/50 mg EEG composite, therefore, achieves an optimal balance between conductivity and active surface exposure, displaying the highest current response and longest discharge time. This enhancement is attributed to the conductive EEG framework, which promotes rapid electron transport and efficient electrode-electrolyte interactions. By comparison, pristine $NiMn(PO_4)_2$ exhibits slower charge-transfer kinetics and lower conductivity, leading to a reduced specific capacitance, while excessive EEG content (100 mg) causes partial restacking of graphene layers, further impeding ion diffusion and charge storage [29].

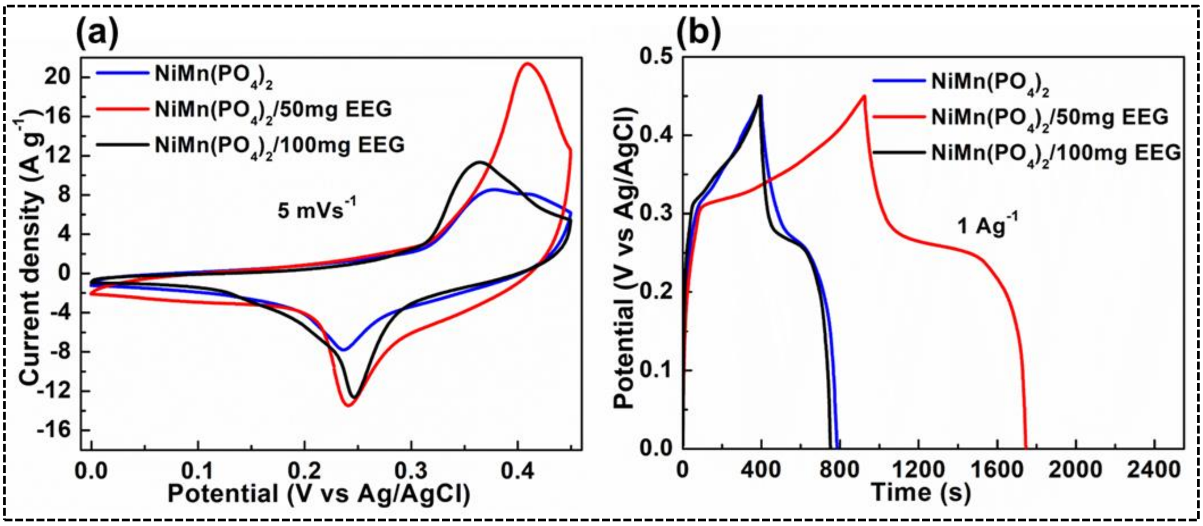

Figure 6.5 (a) Cyclic voltammetry (CV) and (b) galvanostatic charge-discharge (GCD) curves of $NiMn(PO_4)_2$ and $NiMn(PO_4)_2$/EEG electrodes at a scan rate of 5 mV s^{-1} and a current density of 1 A g^{-1}.

To further evaluate rate capability, **Figure 6.6(a-c)** illustrates the CV profiles of pristine $NiMn(PO_4)_2$ and $NiMn(PO_4)_2$/EEG electrodes recorded at scan rates ranging from 5 to 100 mV s^{-1} within the potential window of 0.0-0.45 V versus Ag/AgCl. Both electrodes display distinct redox peaks, confirming that the charge storage mechanism is dominated by faradaic processes. The anodic and cathodic peaks appear at approximately 0.25 V and 0.35 V, respectively, corresponding to the reversible redox transitions of the Ni^{2+}/Ni^{3+} and $Mn^{2+}/Mn^{3+}/Mn^{4+}$ couples. The gradual increase in current density with increasing scan rate indicates excellent rate capability and efficient charge propagation at the electrode/electrolyte interface. This behaviour arises from the diffusion-controlled movement of electrolyte ions; at lower scan rates, ion diffusion is slower, resulting in lower current response, whereas at higher scan rates, the ion flux toward the electrode surface increases, enhancing the overall current response.

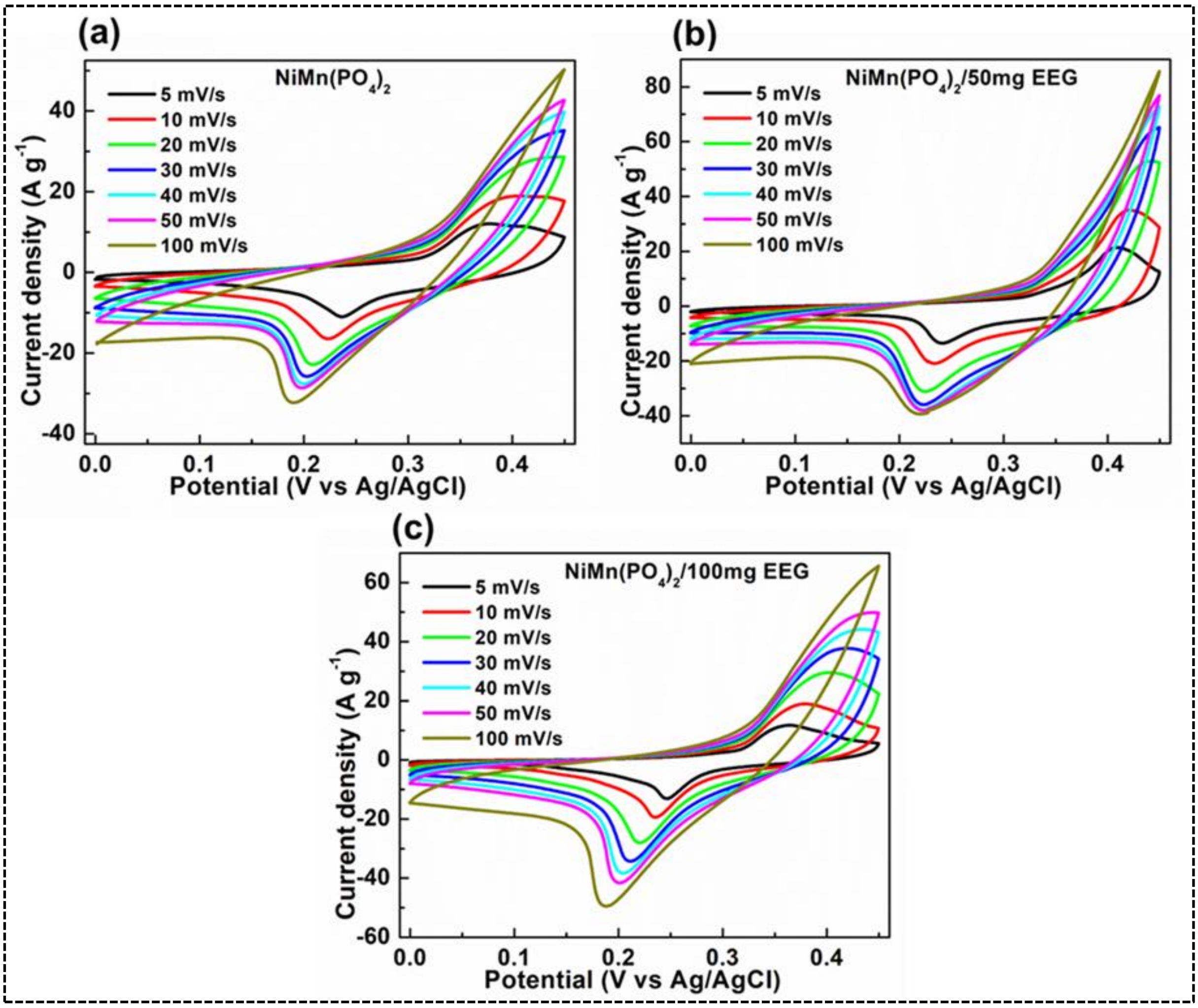

Figure 6.6 (a-c) **CV curves** of $NiMn(PO_4)_2$ and $NiMn(PO_4)_2$/EEG composite electrodes recorded at different scan rates.

The charge-discharge characteristics of the pristine and composite electrodes were further examined at various current densities (1, 2, 3, 4, 5, and 10 A g^{-1}) within the safe potential window of 0.0-0.45 V, as shown in **Figure 6.7(a-c)**. The non-linear GCD curves exhibit multiple potential regions: an initial sharp voltage drops from 0.45 to 0.28 V, a moderate slope between 0.28 and 0.20 V, and a final sharp decline from 0.20 to 0.0 V versus Ag/AgCl. These potential plateaus are indicative of multiple faradaic reactions associated with the redox activity of both Ni and Mn species. The coexistence of Ni^{2+}/Ni^{3+} and $Mn^{2+}/Mn^{3+}/Mn^{4+}$ couples contribute synergistically to the overall pseudocapacitive behaviour, facilitating reversible electron transfer and enhancing specific capacitance and energy density [10,30,31].

Collectively, the electrochemical data confirm that moderate EEG incorporation (50 mg) significantly improves the capacitive behaviour of $NiMn(PO_4)_2$ by providing a conductive network that enhances charge mobility, optimises ion diffusion, and sustains stable redox activity.

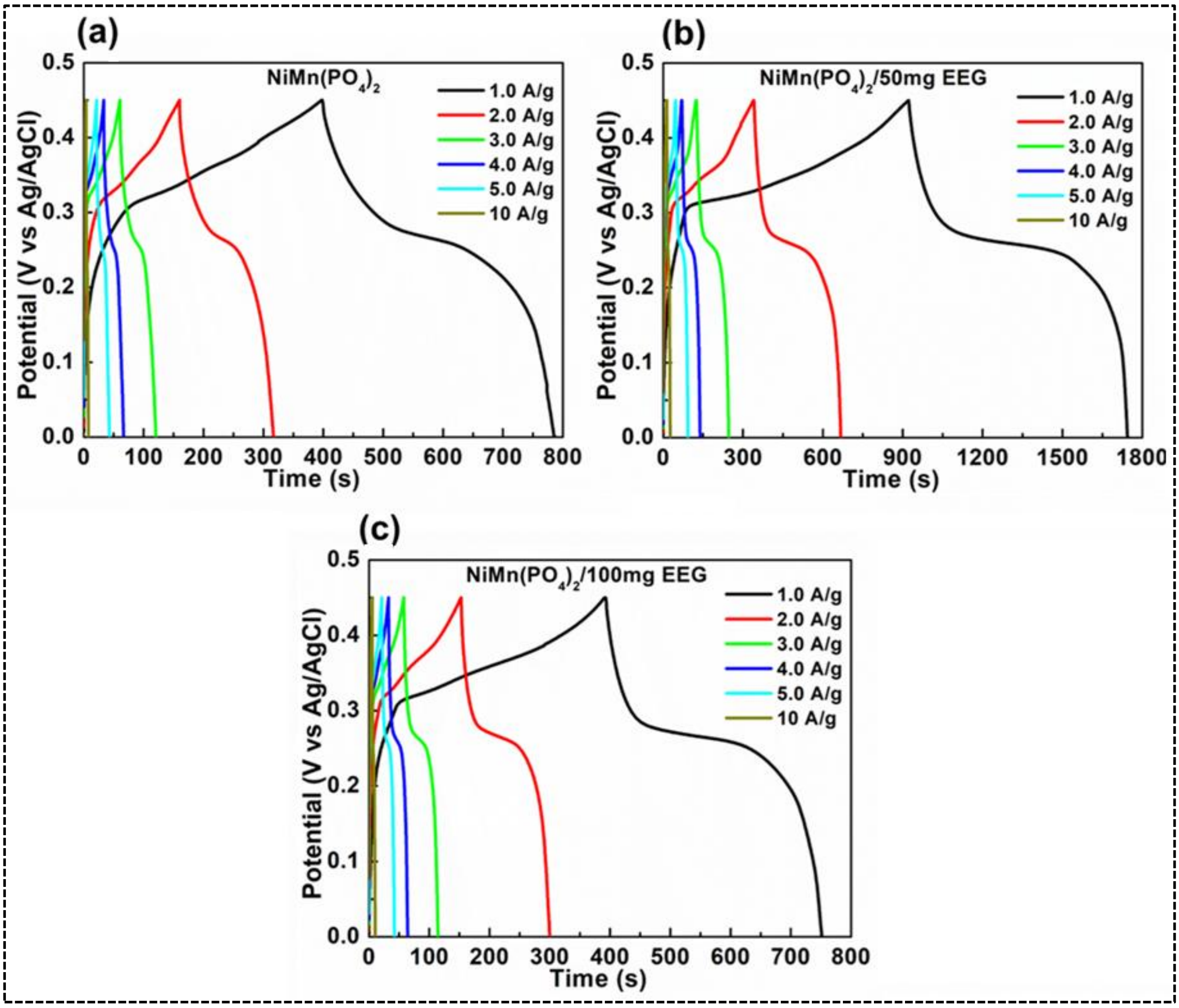

Figure 6.7 (a-c) GCD curves of $NiMn(PO_4)_2$ and $NiMn(PO_4)_2$/EEG composite electrodes measured at varying current densities.

Furthermore, after analysing the GCD results, the specific capacity was calculated using equation (2.3). **Figure 6.8(a)** presents the specific capacity of the pristine $NiMn(PO_4)_2$ and $NiMn(PO_4)_2$/50 mg EEG composite electrodes at various current densities. The $NiMn(PO_4)_2$/50 mg EEG electrode exhibits a markedly higher specific capacity compared to the pristine $NiMn(PO_4)_2$, delivering 822.1 C g^{-1} at 1 A g^{-1}, while the pristine electrode achieves 388.6 C g^{-1}. A gradual decrease in specific capacity is observed for both electrodes with increasing current density **(Figure 6.8(a))**, which can be attributed to the limited ion diffusion and shortened intercalation/extraction time at higher current densities. At lower current densities, OH^- ions have sufficient time to intercalate into and extract from the electrode matrix, facilitating complete redox reactions and yielding higher capacity. Conversely, at higher current densities, ion diffusion becomes kinetically restricted, resulting in diminished capacity [32]. Notably, the $NiMn(PO_4)_2$/EEG composite demonstrates superior electrochemical performance compared to many previously reported electrode materials **(Table 2.1)**, underscoring the effectiveness of EEG incorporation in enhancing charge storage capability.

The cycling performance of the electrodes was further evaluated over 5000 continuous GCD cycles at a current density of 5 A g^{-1}, as shown in **Figure 6.8(b)**. Both pristine and composite electrodes exhibited excellent coulombic efficiency (~100%), confirming good reversibility of the redox reactions **(inset, Figure 6.8(b)).** However, the $NiMn(PO_4)_2$/50 mg EEG electrode retained 71% of its initial specific capacity after 5000 cycles, significantly outperforming the pristine $NiMn(PO_4)_2$, which maintained only 52%. This enhanced cycling stability is attributed to the synergistic interaction between the electrochemically exfoliated graphene and the redox-active Ni-Mn phosphate framework. The EEG sheets provide a highly conductive network that facilitates rapid electron transport and minimizes internal resistance, while the $NiMn(PO_4)_2$ matrix offers abundant redox-active sites, ensuring reversible and stable faradaic processes throughout cycling [29].

To further elucidate the charge-storage mechanism, the anodic peak currents of the pristine $NiMn(PO_4)_2$ and $NiMn(PO_4)_2$/EEG composite electrodes were analysed to gain insight into their charge-storage mechanisms. The peak current values obtained from the CV curves **(Figures 6.8(a-c))** were plotted against the scan rate to determine the corresponding *b*-values, as illustrated in **Figure 6.8(c)**. A *b*-value approaching 1.0 signifies a surface-controlled capacitive process dominated by fast redox reactions, whereas a value near 0.5 indicates a diffusion-controlled faradaic process typical of battery-type behavior [33,34]. The calculated *b*-values for the $NiMn(PO_4)_2$ and $NiMn(PO_4)_2$/50 mg EEG electrodes are 0.49 and 0.48, respectively, suggesting that charge storage in both materials is predominantly governed by diffusion-controlled faradaic reactions occurring within the electrode bulk.

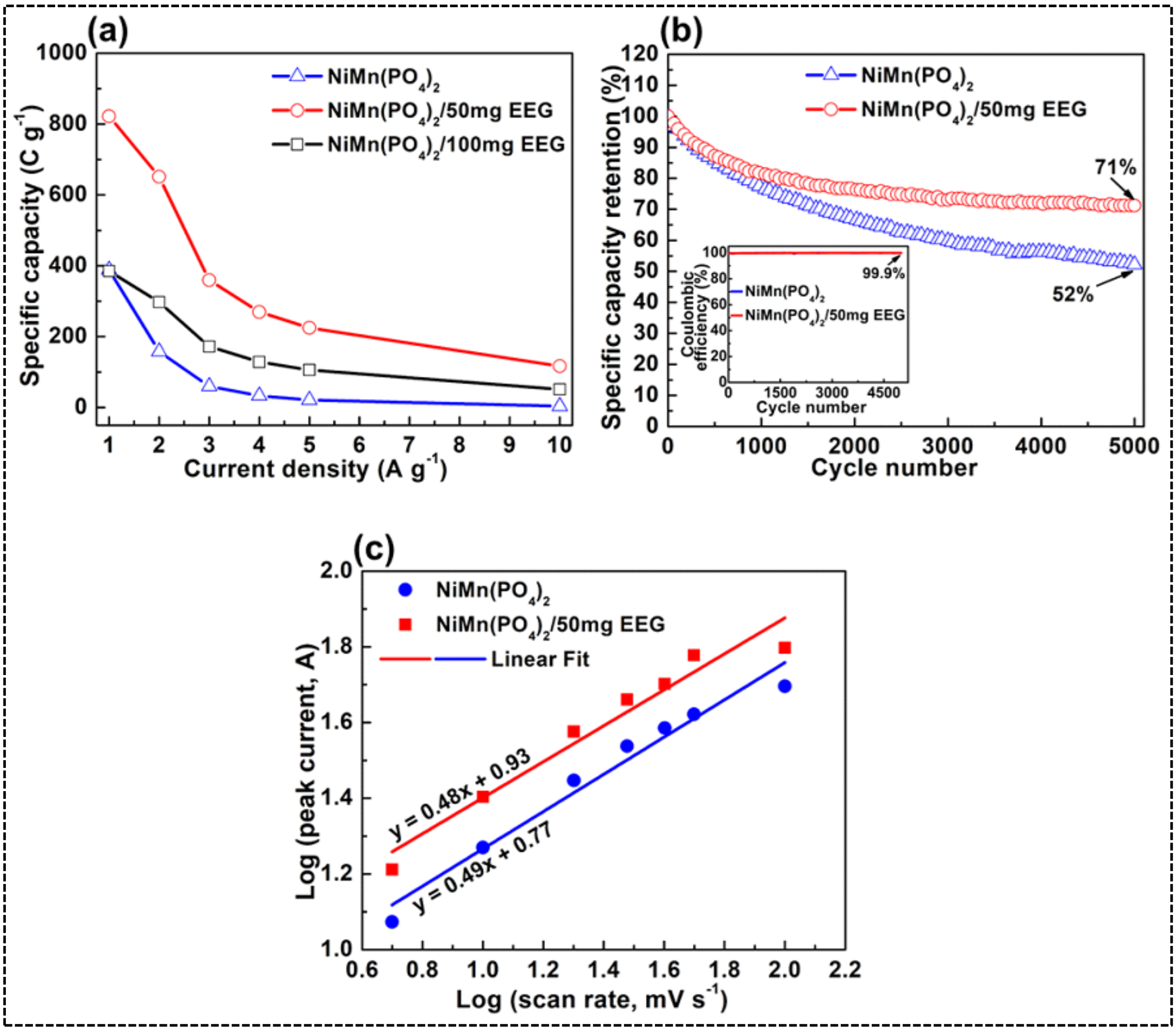

Figure 6.8 (a) Specific capacity of $NiMn(PO_4)_2$ and $NiMn(PO_4)_2$/EEG electrodes as a function of current density. (b) Cycling stability and coulombic efficiency over 5000 GCD cycles at 5 A g^{-1}. (c) Log(current) vs. log(scan rate) relationship for $NiMn(PO_4)_2$ and $NiMn(PO_4)_2$/50 mg EEG electrodes.

Electrochemical impedance spectroscopy (EIS) was employed to further elucidate the charge-transfer behavior and interfacial resistance of the electrodes, as depicted in **Figures 6.9(a,b)**. The Nyquist plots **(Figure 6.9(a))** reveal a semicircular region at high frequency corresponding to charge-transfer resistance (R_{CT}) and a slanted line at low frequency indicative of diffusive ion transport. The low-frequency region of both electrodes shows a line inclined at an angle greater than 45° toward the imaginary axis, characteristic of faradaic processes. The pristine $NiMn(PO_4)_2$ electrode exhibits a longer diffusion path nearly three times that of the $NiMn(PO_4)_2$/50 mg EEG electrode suggesting slower ion migration toward the electrode/electrolyte interface.

In the high-frequency region, the equivalent series resistance (R_S) for the $NiMn(PO_4)_2$/50 mg EEG electrode (1.42 Ω) is significantly lower than that of the pristine $NiMn(PO_4)_2$ electrode (2.13 Ω), indicating improved electrical conductivity and reduced interfacial resistance in the composite. This reduction is attributed to the optimized integration of EEG, which forms an interconnected conductive network that enhances electron transport and ensures intimate contact between $NiMn(PO_4)_2$ microstructures and the current collector. The synergistic interaction between the EEG and the phosphate framework effectively minimizes potential barriers for charge transfer, thereby improving the overall capacitive performance [35].

After 5000 charge-discharge cycles, both electrodes maintained R_S values comparable to their initial measurements, confirming the structural robustness and interfacial stability of the electrode materials. However, a slight increase in diffusion length was observed after cycling, likely due to minor morphological adjustments or structural relaxation within the active material during prolonged operation. These results collectively demonstrate that the $NiMn(PO_4)_2$/50 mg EEG composite electrode exhibits enhanced conductivity, efficient ion diffusion, and superior electrochemical stability, validating its potential as a high-performance electrode material for hybrid supercapacitor applications.

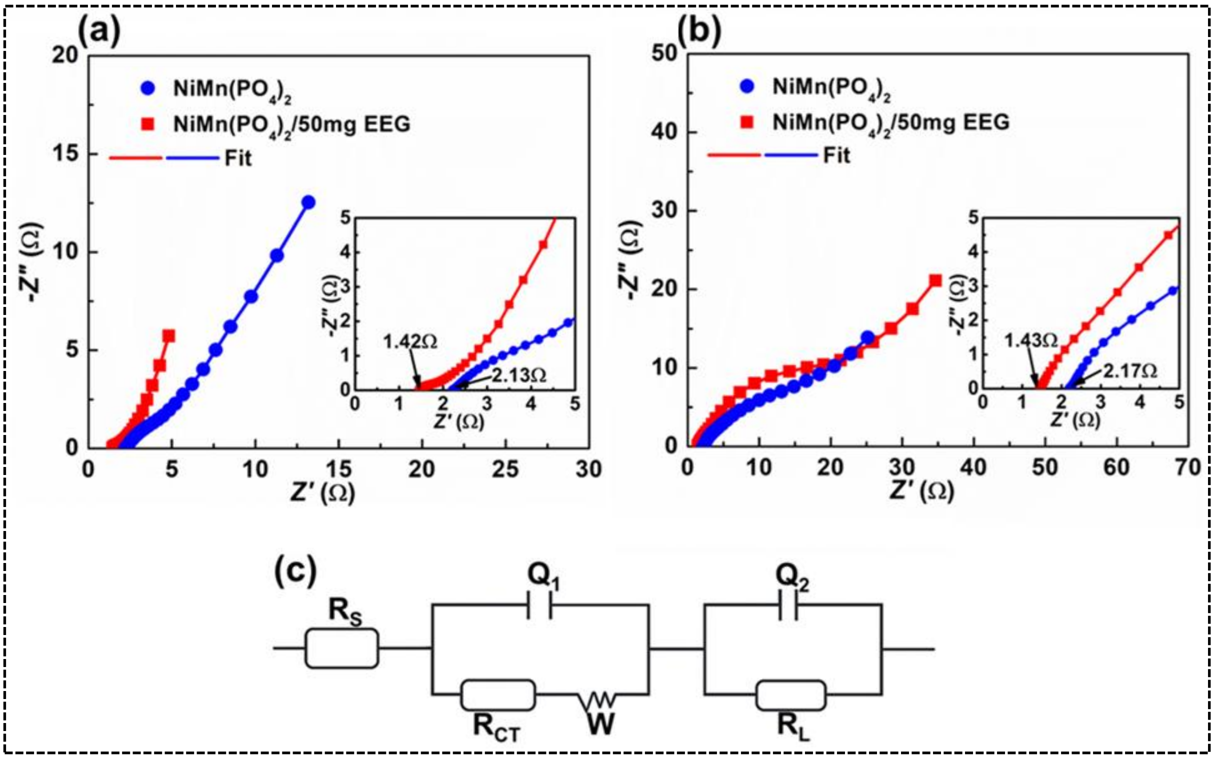

Figure 6.9 (a, b) EIS (Nyquist) plots before and after long-term cycling (5000 GCD cycles at 5 A g^{-1}). (c) Equivalent circuit model used to fit the Nyquist plots shown in (a) and (b).

Furthermore, a two-electrode configuration was employed to evaluate the practical performance of the synthesized materials by assembling a hybrid supercapacitor device. The device was constructed using the high-performing $NiMn(PO_4)_2$/50 mg EEG composite as the positive electrode and wastewater-sludge-derived activated carbon (AC) as the negative electrode, with 1 M KOH aqueous solution serving as the electrolyte **(Figure 6.10(a))**. Although the synthesis and characterisation of the sludge-derived AC were successfully carried out, these results are not included in the main discussion, as they fall outside the primary scope of this study; the full details are provided in **Appendix A**. To ensure charge balance between the two electrodes, the mass ratio was optimised according to the relationship $Q^{+} =$

Q^{-}(Equation 2.5), compensating for differences in specific capacitance between the positive and negative electrodes.

The assembled $NiMn(PO_4)_2$/50 mg EEG//AC hybrid device achieved a maximum operating potential window of 1.4 V **(Figure 6.10(b))**. The cyclic voltammetry (CV) curves exhibit well-defined pseudocapacitive characteristics, maintaining nearly identical shapes even at high scan rates up to 200 mV s^{-1}, confirming excellent electrochemical stability and reversibility. The corresponding galvanostatic charge-discharge (GCD) profiles **(Figure 6.10(c))**, recorded over a current density range of 0.5-10 A g^{-1}, further demonstrate the pseudocapacitive nature of the hybrid device. The calculated specific capacity values, presented in **Figure 6.10(d)**, reveal a high capacity of 220.3 C g^{-1} at A g^{-1}. Even at 10 A g^{-1}, the device retains 54% of its capacity, corresponding to 120.0 C g^{-1}, signifying excellent rate capability and efficient ion transport kinetics within the electrode-electrolyte interface.

Energy and power densities were derived from the GCD discharge curves using equations (2.6 - 2.7) to assess the device's energy storage capability. The $NiMn(PO_4)_2$/50 mg EEG//AC hybrid supercapacitor delivered a maximum energy density of 40.0 Wh kg^{-1} at a power density of 327.1 W kg^{-1} (1.0 A g^{-1}), a value sufficient to power low-energy electronic devices such as wireless sensors, demonstrating its suitability for portable and remote applications. Even at a high current density of 10 A g^{-1}, the device maintained an energy density of 23.4 Wh kg^{-1} and achieved a maximum power density of 6538.0 W kg^{-1} **(Figure 6.10(e))**.

When compared with previously reported nickel-manganese phosphate-based hybrid supercapacitors **(Table 2.4)**, the $NiMn(PO_4)_2$/50 mg EEG//AC device exhibits highly competitive energy–power characteristics and superior cycling stability. Operating within a 1.4 V window, it outperforms several systems including Ni-Co-Mn phosphate@MXene and $NiMn(PO_4)_2$/GF while maintaining 87% capacity retention after 5000 cycles at 5 A g^{-1}. These results demonstrate the significant contribution of EEG in enhancing electrical conductivity, improving interfacial charge-transfer kinetics, and reinforcing overall electrochemical stability, establishing this hybrid system as a promising candidate for next-generation high-performance energy storage devices.

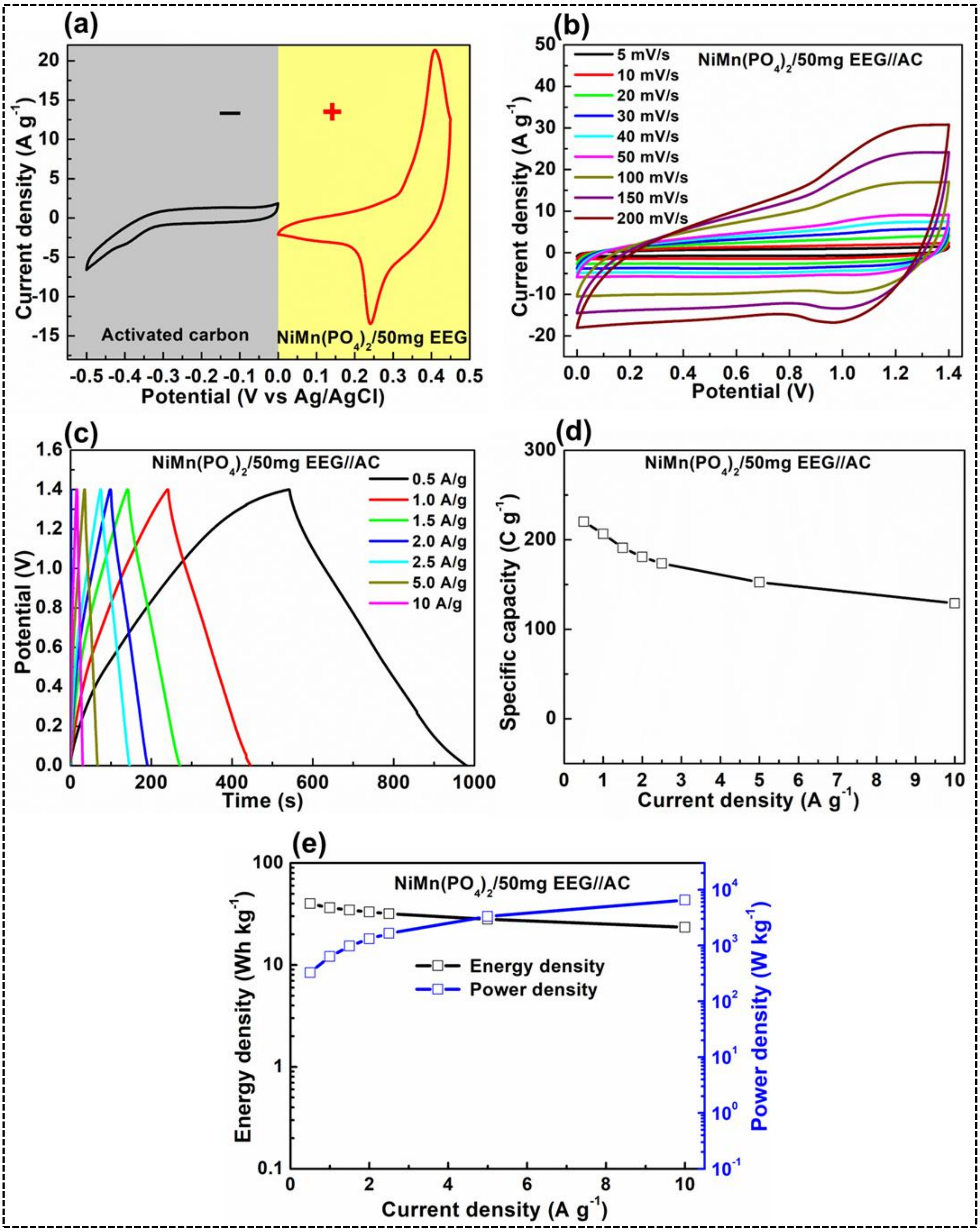

Figure 6.10 $NiMn(PO_4)_2$/50 mg EEG//AC hybrid device: (a) CV curves of wastewater sludge-derived activated carbon and $NiMn(PO_4)_2$/50 mg EEG electrodes at a scan rate of 5 mV s^{-1}. (b) CV and (c) GCD curves of the assembled device at different scan rates and current densities.

(d) Specific capacity versus current density. (e) Energy density and power density as a function of current density.

The cycling stability test conducted at a current density of 5 A g^{-1} **(Figure 6.11(a))** demonstrated outstanding durability, with the device retaining 87% of its initial capacitance and maintaining 97.5% coulombic efficiency after 5000 charge-discharge cycles. This high stability is attributed to the synergistic integration of the redox-active $NiMn(PO_4)_2$/EEG composite and the highly conductive activated carbon electrode, which together enable efficient charge transfer and structural robustness during prolonged cycling. Nonetheless, minor performance degradation over extended operation could arise from electrolyte decomposition or electrode material fatigue, which future optimization efforts should address.

Electrochemical impedance spectroscopy (EIS) results obtained before and after cycling **(Figure 6.11(b))** further confirm the device's structural and interfacial stability. The Nyquist plots exhibit a nearly linear slope in the low-frequency region, slightly tilted above 45°, characteristic of pseudocapacitive behaviour. The comparable series resistance values ($R_S \approx 1$ Ω, inset **Figure 6.11(b)**) before and after cycling indicate minimal changes in electrode-electrolyte resistance, supporting the observed 87% capacitance retention after 5000 cycles. The short diffusion length evident in the low-frequency domain further demonstrates efficient ion diffusion and rapid charge transfer across the electrode-electrolyte interface. The experimental data were fitted using the equivalent circuit model illustrated in **Figure 6.8(c)**, confirming that the hybrid device maintains low internal resistance and high interfacial stability, key features underpinning its long-term durability and superior electrochemical performance.

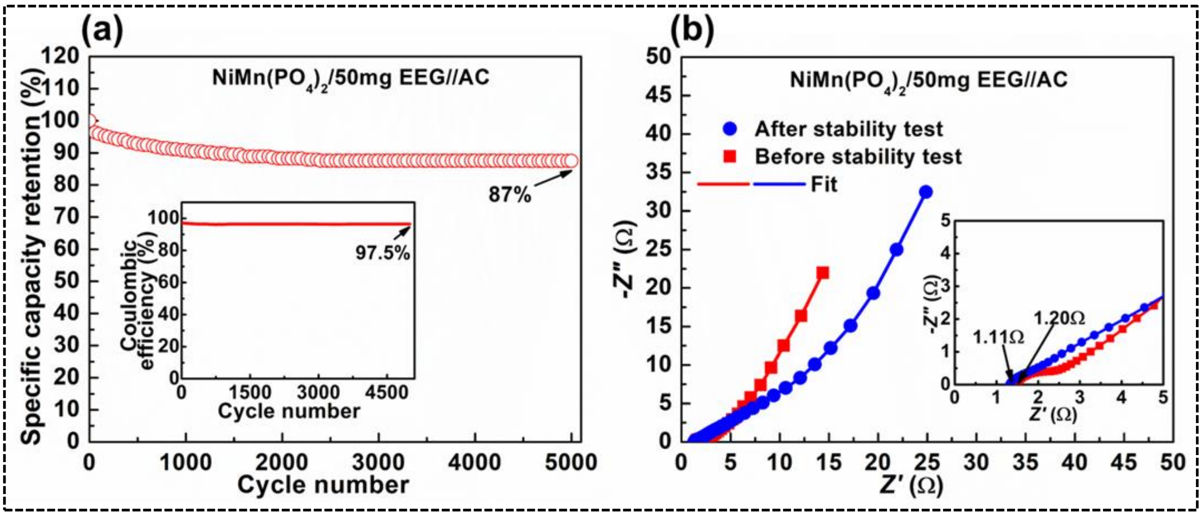

Figure 6.11 $NiMn(PO_4)_2$/50 mg EEG//AC hybrid device performance: (a) Cycling stability and coulombic efficiency over 5000 GCD cycles at 5 A g^{-1}. (b) Nyquist plots before and after the long-term cycling stability test in (a).

As illustrated in **Figure 6.12**, the Ragone comparison between Ni-Mn phosphate-based devices and commercial energy storage systems shows that the $NiMn(PO_4)_2$/50 mg EEG//AC hybrid device achieves energy densities approaching the upper range of typical battery systems, whereas conventional electrochemical capacitors operate at substantially lower energy levels. The energy and power density values obtained in this study are consistent with those reported for other Ni-Mn phosphate-based devices.

It is also important to recognize that laboratory-scale studies typically report gravimetric energy and power densities based solely on the mass of the active materials, while commercial benchmarking normalizes these values to the total cell stack, including current collectors, separators, housing, and electrolyte. [33,36] For meaningful comparison with commercial systems, normalization to the dry cell mass is recommended, and correction factors of four to five are commonly applied when translating laboratory data to practical device performance.

[36,37] Applying such adjustments typically lowers the apparent performance metrics, indicating that the present results as well as prior reports represent promising laboratory-scale outcomes with significant potential for future commercial implementation.

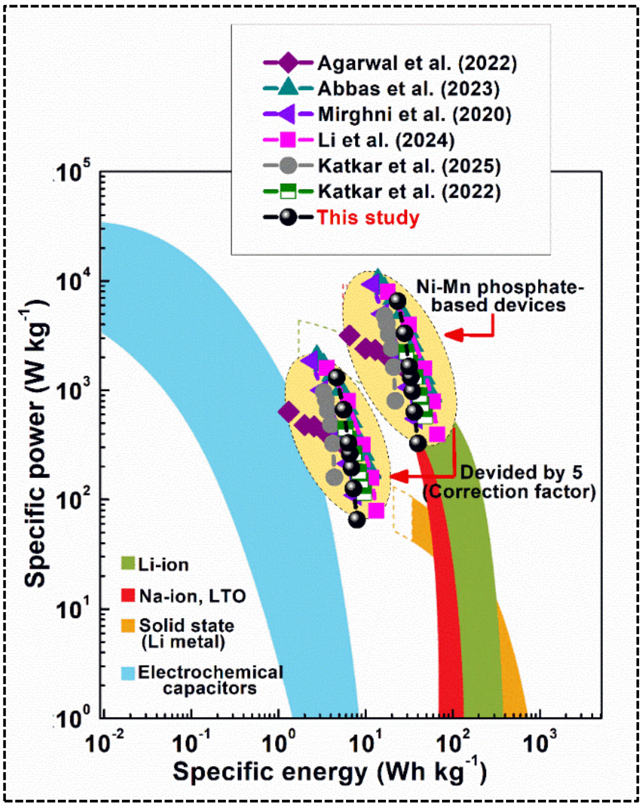

Figure 6.12. Ragone plot showing the energy-power relationship of Ni-Mn phosphate-based devices from this study compared with previously reported systems [38–43], alongside commercial energy-storage technologies such as Li-ion, Na-ion, LTO, solid-state batteries, and electrochemical capacitors. Reprinted with permission from [33], Copyright 2020, Springer Nature.

6.3 Conclusion

The $NiMn(PO_4)_2$/EEG composite and wastewater sludge-derived activated carbon electrodes demonstrated strong electrochemical performance, underscoring their suitability for hybrid supercapacitor applications. The optimized $NiMn(PO_4)_2$/50 mg EEG electrode exhibited excellent charge-transfer characteristics, enhanced redox activity, and durable cycling behaviour, achieving a high specific capacity of 822.1 C g^{-1} with 71% retention after 5000 cycles. When assembled into a hybrid device ($NiMn(PO_4)_2$/50 mg EEG//AC), the system delivered a maximum energy density of 40.0 Wh kg^{-1} and a power density of 6538 W kg^{-1} values comparable to other Ni-Mn phosphate-based devices and indicative of promising laboratory-scale performance with potential for future commercial translation. For practical context, the device is capable of powering a small low-energy sensor for several minutes on a single charge.

References

1. A. Samal, C. Mohanty, N. Das, R. Das, M.F. Kühnel, *Mater Today Chem*, 38 (2024) 102096.
2. X. Li, A.M. Elshahawy, C. Guan, J. Wang, *Small*, 13 (2017).
3. A.A. Mirghni, K.O. Oyedotun, O. Fasakin, B.A. Mahmoud, D.J. Tarimo, N. Manyala, *J Energy Storage*, 31 (2020) 101584.
4. N. Chen, J. Zhou, Q. Kang, H. Ji, G. Zhu, Y. Zhang, S. Chen, J. Chen, X. Feng, W. Hou, *J Power Sources*, 344 (2017) 185–194.
5. A.A. Mirghni, K.O. Oyedotun, O. Fasakin, B.A. Mahmoud, D.J. Tarimo, N. Manyala, *J Energy Storage*, 31 (2020) 101584.
6. P.K. Katkar, S.J. Marje, S.S. Pujari, S.A. Khalate, A.C. Lokhande, U.M. Patil, *ACS Sustain Chem Eng*, 7 (2019) 11205–11218.
7. S.J. Marje, P.K. Katkar, S.S. Pujari, S.A. Khalate, A.C. Lokhande, U.M. Patil, *Synth Met*, 259 (2020) 116224.
8. P.K. Katkar, S.J. Marje, S.S. Pujari, S.A. Khalate, P.R. Deshmukh, U.M. Patil, *Synth Met*, 267 (2020) 116446.
9. P.K. Katkar, Z.A. Sheikh, V.D. Chavan, S.W. Lee, *J Mater Sci Technol*, 206 (2025) 282–296.
10. A. Samal, C. Mohanty, N. Das, R. Das, M.F. Kühnel, *Mater Today Chem*, 38 (2024) 102096.
11. T. Kgwadibane, N.W. Hlongwa, X.G. Fuku, M.J. Madito, *J Energy Storage*, 139 (2025).

12. N.S. Mankge, M.J. Madito, N.W. Hlongwa, A.T. Kuvarega, *J Energy Storage*, 46 (2022).

13. N.S. Mankge, D.Y. Momodu, N.W. Hlongwa, K. Makgopa, A.T. Kuvarega, M.J. Madito, *Synth Met*, 307 (2024) 117652.

14. D. Momodu, M.J. Madito, A. Singh, F. Sharif, K. Karan, M. Trifkovic, S. Bryant, E.P.L. Roberts, *Carbon N Y*, 171 (2021) 130–141.

15. A.G. Nord, *Zeitschrift Fur Kristallographie*, 166 (1984) 159–176.

16. Y. Wu, B. Wang, Y. Ma, Y. Huang, N. Li, F. Zhang, Y. Chen, *Nano Res*, 3 (2010) 661–669.

17. B. Boonchom, S. Youngme, S. Maensiri, C. Danvirutai, *J Alloys Compd*, 454 (2008) 78–82.

18. W. Massa, O. V. Yakubovich, O. V. Dimitrova, *Solid State Sci*, 7 (2005) 950–956.

19. J.A.Z. Martínez, R.L. Porto, I.E.M. Cortez, T. Brousse, J.A.A. Martínez, L.A.L. Pavón, *J Electrochem Soc*, 165 (2018) A2349–A2356.

20. R.L. Frost, *Spectrochim Acta A Mol Biomol Spectrosc*, 60 (2004) 1439–1445.

21. A.C. Ferrari, J. Robertson, *Phys Rev B*, 61 (2000) 14095–14107.

22. TUINSTRA F, KOENIG JL, *Journal of Chemical Physics*, 53 (1970) 1126–1130.

23. A.C. Ferrari, D.M. Basko, *Nat Nanotechnol*, 8 (2013) 235–246.

24. J. Bin Wu, M.L. Lin, X. Cong, H.N. Liu, P.H. Tan, *Chem Soc Rev*, 47 (2018) 1822–1873.

25. L.M. Malard, M.A. Pimenta, G. Dresselhaus, M.S. Dresselhaus, *Phys Rep*, 473 (2009) 51–87.

26. C.F. Chen, C.H. Park, B.W. Boudouris, J. Horng, B. Geng, C. Girit, A. Zettl, M.F. Crommie, R.A. Segalman, S.G. Louie, F. Wang, *Nature*, 471 (2011) 617–620.

27. R.L. Frost, *Spectrochim Acta A Mol Biomol Spectrosc*, 60 (2004) 1439–1445.

28. R.L. Frost, P.A. Williams, W. Martens, J.T. Kloprogge, P. Leverett, *Journal of Raman Spectroscopy*, 33 (2002) 260–263.

29. A.A. Mirghni, M.J. Madito, T.M. Masikhwa, K.O. Oyedotun, A. Bello, N. Manyala, *J Colloid Interface Sci*, 494 (2017) 325–337.

30. L. Soserov, D. Marinova, V. Koleva, A. Stoyanova, R. Stoyanova, *Batteries*, 8 (2022) 51.

31. M.J. Madito, *ACS Appl Mater Interfaces*, 13 (2021) 37014–37026.

32. C. Yuan, X. Zhang, L. Su, B. Gao, L. Shen, *J Mater Chem*, 19 (2009) 5772–5777.

33. P. Simon, Y. Gogotsi, *Nat Mater*, 19 (2020) 1151–1163.

34. M.R. Lukatskaya, B. Dunn, Y. Gogotsi, *Nat Commun*, 7 (2016) 12647.

35. M.J. Madito, *ACS Appl. Mater. Interfaces*, 13 (2021) 37014–37026.

36. Y. Gogotsi, P. Simon, *Science (1979)*, 334 (2011) 917–918.

37. A. Balducci, D. Belanger, T. Brousse, J.W. Long, W. Sugimoto, *J Electrochem Soc*, 164 (2017) A1487–A1488.

38. A. Agarwal, S. Majumder, B.R. Sankapal, *Energy and Fuels*, 36 (2022) 5953–5964.

39. Z. Abbas, M.R.A. Karim, W. Shehzad, N.A. Shama, J. Kumar, Sirajuddin, S. Karakuş, R.A. Soomro, A. Nafady, *Electrochim Acta*, 471 (2023).

40. A.A. Mirghni, K.O. Oyedotun, O. Fasakin, B.A. Mahmoud, D.J. Tarimo, N. Manyala, *J Energy Storage*, 31 (2020) 101584.

41. M. Li, M. Zhao, B. Wu, S. Mourdikoudis, S. Wei, F.M. Oliveira, J. He, L. Děkanovský, J. Luxa, S. Yang, Z. Sofer, *Chemical Engineering Journal*, 482 (2024).

42. P.K. Katkar, Z.A. Sheikh, V.D. Chavan, S.W. Lee, *J Mater Sci Technol*, 206 (2025) 282–296.

43. P.K. Katkar, S.A. Patil, J.H. Jeon, H.R. Na, N.S. Padalkar, S.K. Jerng, S. Lee, S.H. Chun, *Energy and Fuels*, 36 (2022) 13356–13369.

CHAPTER 7

GENERAL CONCLUSIONS AND RECOMMENDATIONS

7.1 Concluding Remarks

This research successfully developed and characterised heteroatom-doped electrochemically exfoliated graphene (EEG) films and Ni-Mn$(PO_4)_2$/EEG composite electrodes for application in hybrid supercapacitors. The study demonstrates that the strategic integration of mixed-metal phosphate chemistry with highly conductive, defect-engineered graphene matrix provides an effective pathway for enhancing electrochemical energy storage performance.

A significant outcome of the work is the successful synthesis and structural confirmation of heteroatom-doped EEG, achieved through a controlled two-step intercalation/exfoliation process. XPS analysis verified the incorporation of nitrogen, phosphorus, and sulphur into the graphene matrix, each contributing uniquely to electronic and structural modifications. These dopants generated measurable Fermi-level shifts and introduced beneficial defect sites, collectively enhancing charge carrier density, electrical conductivity, and surface reactivity. Raman spectroscopy further confirmed the presence of doping-induced disorder and heterogeneous defect domains, validating the relationship between doping configuration and electronic behaviour. The strong agreement between experimental findings and theoretical predictions underscores the reliability of the doping approach and its effectiveness in tailoring graphene for electrochemical applications.

Parallel to this, the Ni-Mn$(PO_4)_2$ phosphate was successfully synthesised and characterised as a mixed-metal olivine-related structure composed of interconnected MO_6 (M = Ni^{2+}, Mn^{2+})

octahedra and PO_4 tetrahedra. The coexistence of Ni and Mn within the phosphate lattice provided both structural robustness and enhanced redox activity. XRD analysis revealed a well-defined crystalline structure comprising Ni-Mn$(PO_4)_2$ as a dominant phase alongside minor $Ni_3(PO_4)_2$ and $Mn_3(PO_4)_2$ phases. This mixed-metal configuration contributed to improved electronic and ionic transport, supporting stable faradaic reactions during cycling.

When integrated with EEG, the resulting Ni-Mn$(PO_4)_2$/EEG composite showed marked improvements in electrochemical behaviour. The conductive graphene network facilitated rapid electron transfer, increased accessible active sites, and enhanced structural stability of the phosphate phase. The optimized Ni-Mn$(PO_4)_2$/50 mg EEG electrode delivered an impressive specific capacity of 822.1 C g^{-1}, outperforming many previously reported Ni-Mn phosphate-based materials. The electrode retained 71% of its initial capacity after 5000 cycles, reflecting strong cycling durability and resistance to structural degradation.

The hybrid device assembled using the Ni-Mn$(PO_4)_2$/EEG as a positive electrode and AC as a negative electrode exhibited a high energy density of 40.0 Wh kg^{-1} at a power density of 327.1 W kg^{-1}, and sustained a maximum power density of 6538 W kg^{-1}. Importantly, the device maintained 87% cycling retention after 5000 charge-discharge cycles, demonstrating excellent long-term reliability. These performance indicators compare favourably with previously reported Ni-Mn phosphate systems, with the present system showing competitive or superior energy power characteristics.

This study provides compelling evidence that:

i. Heteroatom-doped EEG significantly enhances electron transport and interfacial charge transfer, validating its role as an advanced conductive scaffold.

ii. Ni-Mn$(PO_4)_2$ offers a stable, redox-active mixed-metal phosphate framework capable of delivering strong pseudocapacitive behaviour.

iii. The synergistic integration of Ni-Mn$(PO_4)_2$ and heteroatom-doped EEG produces a composite with high capacity, good rate capability, and excellent cycling stability.

iv. The assembled hybrid supercapacitor demonstrates practical energy storage potential, achieving energy and power outputs suitable for powering low-energy electronic devices.

Overall, this research establishes a solid foundation for the development of next-generation hybrid supercapacitors based on mixed-metal phosphates and engineered graphene. The strong performance metrics, combined with the scalability of the synthesis methods employed, highlight the technological relevance and future potential of the Ni-Mn$(PO_4)_2$/EEG system in advanced energy storage applications.

7.2 Recommendations

Based on the outcomes of this study, several research directions and practical considerations are proposed:

i. Optimization of Phosphate-Carbon Interfaces: Future work should focus on tailoring the interfacial chemistry between Ni-Mn$(PO_4)_2$ and EEG to further enhance charge-transfer efficiency. Strategies may include surface functionalisation, controlled nucleation of phosphate particles, or use of linker molecules to strengthen interfacial coupling.

ii. Expanded Heteroatom-Doping Strategies: The role of co-doping could be further explored by varying dopant ratios or introducing additional heteroatoms (e.g., B or F) to tune electronic structure and catalytic activity. Advanced in-situ spectroscopies would help reveal how dopants influence redox behaviour during cycling.

iii. Mechanistic Studies Under Operating Conditions: In-situ/operando characterisation, such as Raman, XRD, or XPS during electrochemical cycling, would provide deeper insight into phase evolution, electronic restructuring, and degradation pathways within both EEG and the Ni-Mn$(PO_4)_2$ framework.

iv. Device-Level Optimization and Modelling: Future studies should investigate electrode balancing, electrolyte formulation, and cell-level engineering to achieve higher voltage windows and improved energy densities. Device modelling could also guide material selection and electrode design for optimal performance.

v. Scale-Up and Manufacturing Pathways: To move toward practical implementation, emphasis should be placed on scalable synthesis routes (low-temperature synthesis, continuous exfoliation processes, slurry-based coating, or roll-to-roll film formation). Long-term reliability testing in pouch-cell formats is also recommended.

APPENDIX A

WASTEWATER SLUDGE-DERIVED ACTIVATED CARBON FOR HYBRID SUPERCAPACITORS

A.1 Introduction

Wastewater sludge (WWS) generation has increased significantly in recent years, driven by rapid urbanisation, industrial expansion, and growing potable water demand. Although comprehensive global data remain limited, national estimates suggest that approximately 53 million tonnes of dried sludge are produced annually. The expansion of urban water systems to meet drinking water needs has further intensified sludge production at wastewater treatment plants (WWTPs). Effective management of this waste stream remains a major challenge due to its heterogeneous composition, potential environmental risks, and the declining suitability of conventional disposal methods such as landfilling and agricultural application [1–3]. Converting WWS into carbon-based materials for advanced electrochemical energy storage offers a promising route that simultaneously addresses waste management and contributes to the development of clean energy technologies.

In the synthesis of activated carbon from WWS, air-dried WWS was immersed in 30% phosphoric acid (H_3PO_4) at a sludge-to-acid ratio of 1:10 (w/v) for 18 hours. The treated material was washed, oven-dried at 100 °C, and carbonized at 600 °C for 4 hours under an inert atmosphere. The resulting activated carbon was washed repeatedly with deionized water to remove residual acid and soluble impurities, oven-dried at 100 °C, pulverized, and sieved to achieve a uniform particle size.

This is part of manuscript is published as T. Kgwadibane et al., J. Energy Storage.152 (2026).120697.

A.2 Results and discussion

A.2.1 Physicochemical and structural characterisation

The surface morphology of the wastewater-sludge-derived activated carbon, shown in **Figure A.1(a)**, reveals a heterogeneous structure composed of irregular and agglomerated particles, which is characteristic of carbon materials undergoing activation and carbonisation. These processes promote pore development and structural rearrangement, resulting in the observed rough and non-uniform texture. The accompanying EDS spectrum **(Figure A.1(b))** further confirms the elemental composition of the material, showing carbon (44.4 wt%) and oxygen (40.1 wt%) as the dominant constituents, along with phosphorus (10.7 wt%), silicon (3.8 wt%), and aluminium (1.0 wt%). The presence of phosphorus, silicon, and aluminium reflects residual inorganic species from the raw wastewater sludge, while the phosphorus content also indicates the influence of H_3PO_4 used as the activating agent.

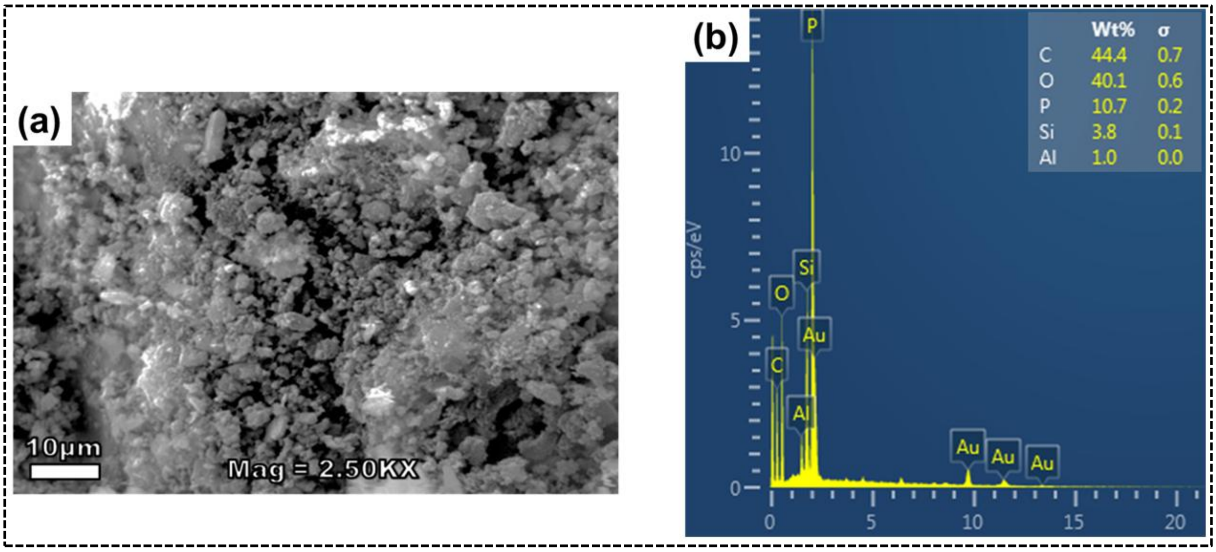

Figure A.1 (a) SEM micrograph, (b) EDS spectra of the as-synthesised wastewater sludge-derived activated carbon.

Building on the morphological and compositional insights, the structural characteristics of the wastewater-sludge-derived activated carbon were further examined using XRD, as presented in **Figure A.2(a)**. The diffraction pattern is shown alongside ICSD reference entries hexagonal carbon (card no. 31170; P63mc), monoclinic SiP_2O_7 (card no. 8096; P121/n1), and tetragonal SiO_2 (card no. 34889; P43212) with colour-coded peak histograms used to assist phase identification. The activated carbon displays several prominent reflections at $2\theta = 20.3°$, 22.9°, 23.8°, 26.4°, 27.5°, 30.4°, 33.1°, 37.3°, 38.0°, and 42.8°, all attributed to crystalline SiP_2O_7, while peaks at 25.8° and 28.9° correspond to SiO_2. The broad hump normally associated with amorphous carbon near 26° is largely masked by overlapping crystalline peaks. The strong presence of SiP_2O_7 confirms that silica from the sludge reacted with phosphoric acid during activation to produce stable silicophosphate phases. These robust Si–P–O networks contribute to enhanced structural stability and help maintain the porous carbon framework during long-term electrochemical operation.

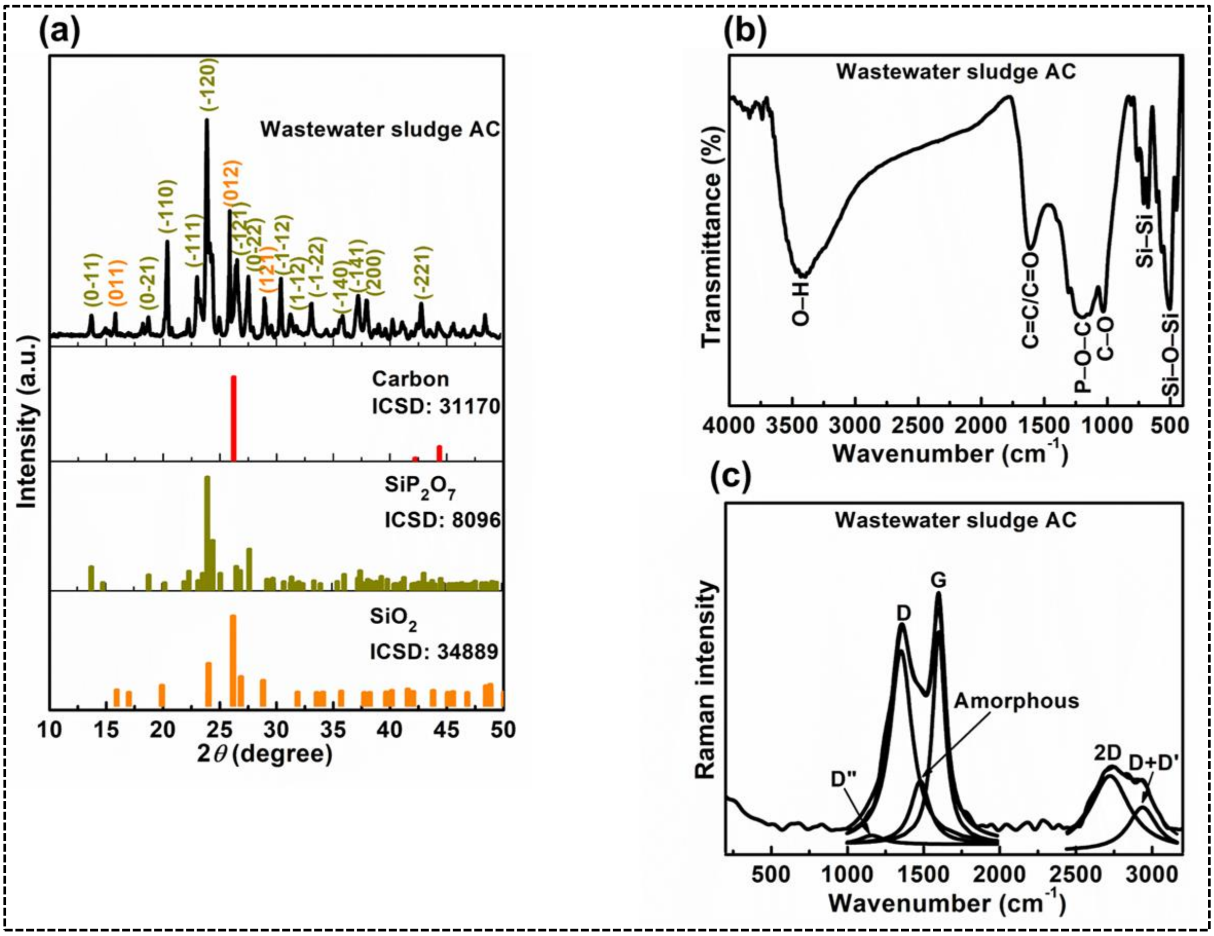

Figure A.2 (a) XRD patterns with histograms as reference patterns from various Inorganic Crystal Structure Database (ICSD) cards. (b) FTIR and (c) Raman spectra of wastewater sludge-derived activated carbon

Complementing the structural information obtained from XRD, the surface chemistry and disorder characteristics of the wastewater-sludge-derived activated carbon were further analysed using FTIR and Raman spectroscopy **(Figure A.2(b,c))**. The FTIR spectrum **(Figure A.2(b)** shows a broad O–H stretching band at 3413 cm^{-1}, attributed to hydroxyl groups from phenols, alcohols, or adsorbed moisture [4,5], while the band at ~1615 cm^{-1} corresponds to C=C and C=O stretching in aromatic structures. A peak near 1037 cm-1 arises from C–O stretching in carboxylic acids, alcohols, phenols, or esters [6]. Structural modification induced by H_3PO_4 activation is evident from the band at ~1190 cm^{-1}, assigned to P–O–C linkages, confirming successful incorporation of phosphorus into the carbon matrix [7]. Additional bands at ~510 and ~710 cm^{-1} reflect Si–O–Si and Si–Si vibrations, consistent with residual inorganic components identified by XRD.

Raman spectroscopy provides further insight into the carbon framework, revealing prominent D (1356 cm^{-1}) and G (1603 cm^{-1}) bands characteristic of disordered and graphitic carbon, respectively **(Figure A.3(c))**. A broad feature around ~2900 cm^{-1}, associated with the 2D and D+D' bands, indicates turbostratic stacking and limited graphitization, while a broad shoulder near ~1500 cm^{-1} is typical of amorphous carbon.[8]. The G band originates from in-plane C–C bond stretching (E_{2g} mode), whereas the defect-activated D band appears due to lattice disorder. The measured $I_{(D)}/I_{(G)}$ ratio of 0.90 confirms a predominantly disordered carbon structure [9], with an estimated in-plane crystallite size (L_a) of ~5.5 nm based on the Tuinstra-Koenig relation [10]. Together, these FTIR and Raman results support the presence of a heteroatom-containing, structurally disordered carbon matrix consistent with the complex composition and crystalline phases revealed by XRD.

A.2.2 Electrochemical characterization

Furthermore, the electrochemical performance of the wastewater sludge-derived activated carbon (AC) as a negative electrode for the hybrid supercapacitor device was evaluated using a conventional three-electrode configuration in 1 M KOH aqueous electrolyte within a potential window of –0.5 to 0.0 V versus Ag/AgCl **(Figure A.3)**. The cyclic voltammetry (CV) and galvanostatic charge-discharge (GCD) profiles shown in **Figures A.3(a-b)** exhibit nearly rectangular and symmetrical shapes across scan rates of 5-100 mV s^{-1} and current densities of 2-10 A g^{-1}, respectively, characteristic of ideal capacitive behavior. Long-term cycling stability, assessed over 5000 continuous GCD cycles at a current density of 5 A g^{-1} **(Figure A.3(e))**, demonstrated excellent durability, with 91% capacitance retention and nearly 100% coulombic efficiency, reflecting the inherent structural robustness of carbon-based electrodes.

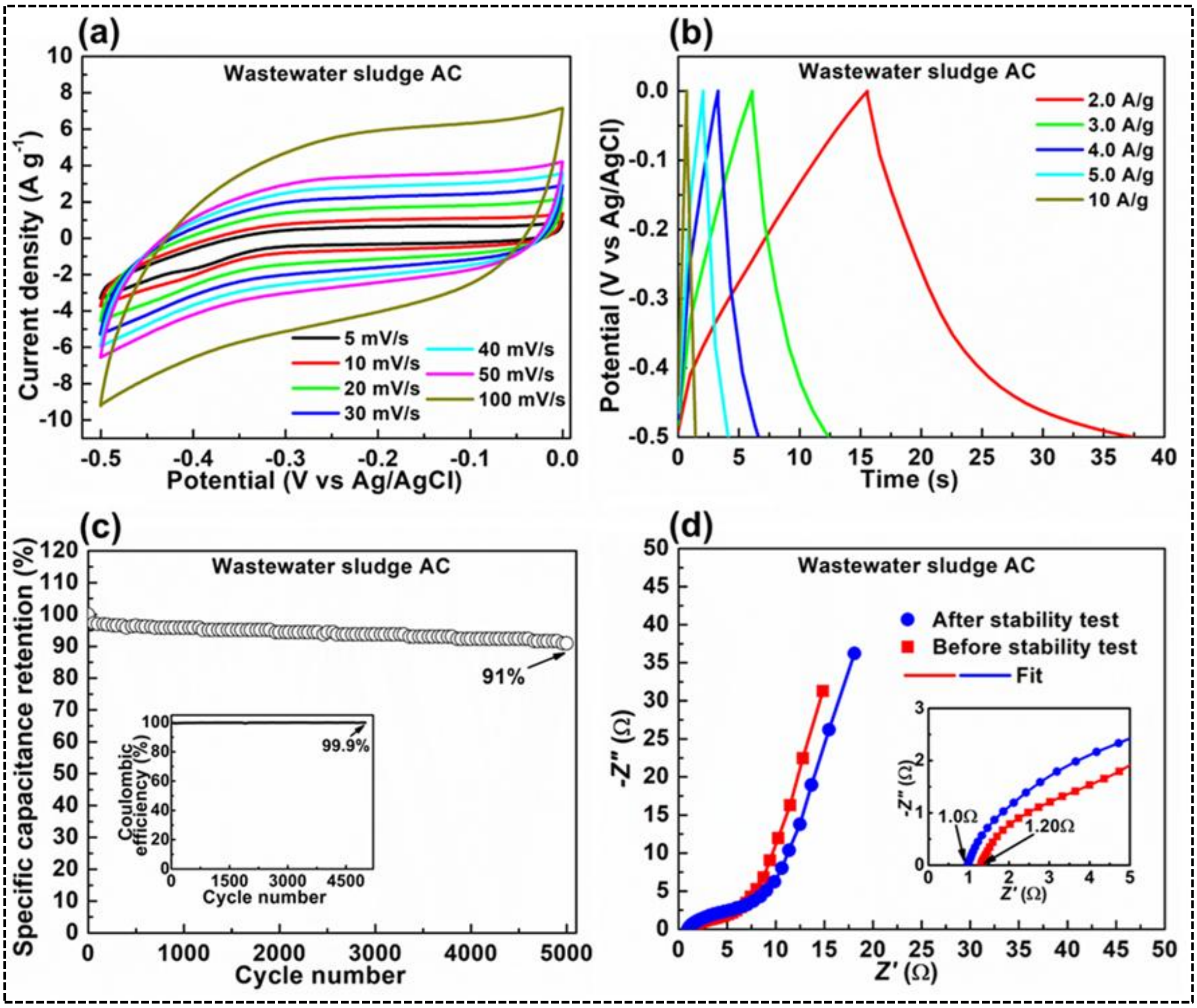

Figure A.3 Wastewater sludge-derived AC electrode: (a) CV and (b) GCD curves at different scan rates and current densities; (c) cycling stability and coulombic efficiency over 5000 GCD cycles at 5 A g^{-1}; (d) Nyquist plots before and after long-term cycling in (c).

Electrochemical impedance spectroscopy (EIS) measurements obtained before and after cycling **(Figure A.3(f))** further confirmed the electrode's stability. The Nyquist plots display negligible variation in series resistance ($R_S \approx 1\ \Omega$), indicating that the charge-transfer characteristics and electrode architecture remained largely unchanged after prolonged cycling. Moreover, the short diffusion length observed in the low-frequency region signifies efficient ion transport and rapid interfacial charge transfer. These findings collectively highlight the superior electrochemical reversibility, conductivity, and long-term reliability of the wastewater sludge-derived activated carbon electrode, underscoring its suitability as a negative electrode material for hybrid supercapacitor applications.

A.3 Conclusion

Beyond its electrochemical performance, this work also demonstrates a sustainable waste-to-energy pathway by upcycling municipal sludge into functional activated carbon. Although the sludge-derived AC contained lower carbon content and residual inorganic species, improvements in purification, activation, and carbonisation protocols could enhance graphitic ordering and porosity. Future studies should explore low-temperature carbonisation (<600 °C), in-situ redox monitoring to better understand electrode behaviour, and pilot-scale pouch cell testing to bridge laboratory results with industrial implementation.

This is part of manuscript is published as T. Kgwadibane et al., J. Energy Storage.152 (2026).120697.

References

1. A. Rorat, P. Courtois, F. Vandenbulcke, S. Lemiere, Industrial and Municipal Sludge: Emerging Concerns and Scope for Resource Recovery, (2019), pp. 155–180.
2. S. Shaddel, H. Bakhtiary-Davijany, C. Kabbe, F. Dadgar, S.W. Østerhus, *Sustainability (Switzerland)*, 11 (2019).
3. M.K.H. Winkler, C. Meunier, O. Henriet, J. Mahillon, M.E. Suárez-Ojeda, G. Del Moro, M. De Sanctis, C. Di Iaconi, D.G. Weissbrodt, *Chemical Engineering Journal*, 336 (2018) 489–502.
4. P. Wiercik, M. Kuśnierz, M. Kabsch-Korbutowicz, A. Plucińska, P. Chrobot, *Desalination Water Treat*, 273 (2022) 114–125.
5. D. Shrestha, S. Maensiri, U. Wongpratat, S.W. Lee, A.R. Nyachhyon, *J Environ Chem Eng*, 7 (2019).
6. N. Bouchelkia, K. Benazouz, A. Mameri, L. Belkhiri, N. Hamri, H. Belkacemi, A. Zoukel, A. Amrane, F. Aoulmi, L. Mouni, *Processes*, 11 (2023).
7. A. Damayanti, R. Wulansarie, Z.A.S. Bahlawan, Suharta, M. Royana, M.W.N.M. Basuki, B. Nugroho, A.L. Andri, *ChemEngineering*, 7 (2023).
8. A. Sadezky, H. Muckenhuber, H. Grothe, R. Niessner, U. Pöschl, *Carbon N Y*, 43 (2005) 1731–1742.
9. A.C. Ferrari, D.M. Basko, *Nat Nanotechnol*, 8 (2013) 235–246.
10. F. Tuinstra, J.L. Koenig, *J Chem Phys*, 53 (1970) 1126–1130.

APPENDIX B

PUBLICATIONS ARISING FROM THIS DISSERTATION

1. **T. Kgwadibane**, N.W. Hlongwa, X.G. Fuku, M.J. Madito,

   Recent advances in nickel-manganese phosphates-based electrodes for hybrid supercapacitors,

   Journal of Energy Storage 139 (2025) 118782.

2. **T. Kgwadibane**, R. Morad, D.Y. Momodu, N.W. Hlongwa, X. Fuku, M.J. Madito,

   Heteroatom-doped electrochemically exfoliated graphene thin films: A Raman spectroscopy and density functional theory study

   Diamond & Related Materials 160 (2025) 113058

3. **T. Kgwadibane**, M.O. Bello, R. Morad, N.W. Hlongwa, X. Fuku, M.J. Madito,

   Hydrothermal synthesis of $NiMn(PO_4)_2$/electrochemically exfoliated graphene composites and wastewater sludge-derived activated carbon for hybrid supercapacitors

   Journal of Energy Storage 152 (2026) 120697

APPENDIX C

CONFERENCE PRESENTATIONS ARISING FROM THIS DISSERTATION

1. **Oral Presentation: T. Kgwadibane**

   Title: *Raman Imaging of high conductivity Electrochemically Exfoliated Graphene: Fermi Level Shift and the Electrochemical Performance*

   Event:*7th International Symposium on Electrochemistry, 2025.*

   Venue: *Southern Sun Maharani Hotel in Durban, KwaZulu-Natal.*

2. **Poster Presentation: T. Kgwadibane**

   Title: *Wastewater Sludge-Based Activated Carbon for Supercapacitors*

   Event: *Renewable Energy and Storage Workshop/Symposium 2025, Department of Chemistry, University of Pretoria, 2025*

   Venue: *Conference 100, UP Conference Centre, Hatfield Campus, University of Pretoria*